Title
Water Vapor Variability Across Spatial Scales: Insights for Theory, Parameterization, and Model Assessment

Author
Pressel, Kyle Gregory

Publication Date
2012

Peer reviewed|Thesis/dissertation

Water Vapor Variability Across Spatial Scales: Insights for Theory, Parameterization, and Model Assessment

by

Kyle Gregory Pressel

A dissertation submitted in partial satisfaction of the
requirements for the degree of
Doctor of Philosophy

in

Engineering - Civil and Environmental Engineering

in the

Graduate Division

of the

University of California, Berkeley

Committee in charge:

Professor William D. Collins, Co-chair
Professor Fotini Katopodes Chow, Co-chair
Professor John C. H. Chiang
Professor Robert A. Harley

Spring 2012

Water Vapor Variability Across Spatial Scales: Insights for Theory, Parameterization, and Model Assessment

Abstract

Water Vapor Variability Across Spatial Scales: Insights for Theory, Parameterization, and Model Assessment

by

Kyle Gregory Pressel

Doctor of Philosophy in Engineering - Civil and Environmental Engineering

University of California, Berkeley

Professor William D. Collins, Co-chair

Professor Fotini Katopodes Chow, Co-chair

The subject of this dissertation is the scale dependence of water vapor variability as observed by remote sensing and in situ measurements, and predicted by aqua-planet simulation. Global observations of the water vapor field from the Atmospheric Infrared Sounder (AIRS) are used to show that the first order structure function of the water vapor field exhibits power law behavior for scales between 50 km and 500 km throughout much of the troposphere. The power law scaling exponents are shown to vary between the boundary layer and free troposphere, with first order structure function scaling exponents of approximately 1/3 in the boundary layer and less than 1/2 in the free troposphere. Observations from the 396 m level of the WLEF television broadcast tower are used to show that the convective mixed layer layer and nocturnal residual layer exhibit power law behavior of first order structure functions and first order detrended fluctuation functions for scales between 1 km and 100 km. The power law scaling exponents computed from the tower observations of the convective mixed layer are shown to be consistent with the AIRS boundary layer regime exponents, while the exponents computed from the tower observations of the residual layer are shown to be consistent with AIRS free tropospheric regime scaling exponents. Finally, structure functions of the instantaneous water vapor field are computed from aqua-planet simulations performed at T85 and T340 spectral resolutions. Free tropospheric structure function scaling exponents for scales less than 500 km computed from the T340 spectral resolution simulation are shown to agree very well with free tropospheric scaling exponents computed from AIRS. Boundary layer structure function scaling exponents from the T340 spectral resolution are shown to be generally larger than boundary layer scaling exponents from AIRS.

In memory of my Grandfather, C. Carlton Brown (1919 - 2006)

Who being neither a professional scientist nor a professional academic, neverthless instilled in me the fundamental curiosity about the natural world and desire to know that has driven me to science.

Contents

List of Figures

List of Tables

Acknowledgments

The author would like to acknowledge and thank his advisor and Thesis Committee Chair William D. Collins whose passion and drive to work on many of the open questions and challenges in the climate sciences, while leading one of the world's preeminent climate research centers will serve as an inspiration to me throughout my career.

The author would like to acknowledge and thank his Thesis Committee including, Professors Fotini Katopodes Chow and Robert A. Harley of the Department of Civil and Environmental Engineering, Professor William D. Collins of the Department of Earth and Planetary Sciences, and Professor John C. H. Chiang of the Department of Geography. The diversity and depth of their knowledge of atmospheric sciences is without comparison.

During the course of this research KGP was supported by The United States Department of Homeland Security Scholar and Fellows Program administered by Oak Ridge Associated Universities, The NASA Interdisciplinary Science Program and the DOE BER project on robust regional climate modeling.

The author would like to thank Brian Kahn of the Jet Propulsion Laboratory and Farid Ait-Chaalal of the The California Institute of Technology for productive discussions and suggestions and two reviewers for their comments, criticisms, and suggestions that yielded significant improvements to Chapter 2. AIRS data were obtained through the Goddard Earth Sciences Data and Information Services Center (online at http://daac.gsfc.nasa.gov/).

The author would like to thank and acknowledge Professor Ankur R. Desai of The University of Wisconsin, Madison who provided access to WLEF dataset, and never failed to provide the high quality custom data sets used in Chapter 3 in a remarkably timely fashion. WLEF flux tower measurements were made possible via tireless efforts of K.J. Davis of Pennsylvania State University, J. Thom of University of Wisconsin-Madison, B.D. Cook of NASA Goddard Space Flight Center, R. Teclaw and D. Baumann of the U.S. Forest Service Northern Research Station, and R. Strand, of the Wisconsin Education Communications Board (ECB).

The author would also like to acknowledge the help of Fuyu Li of Lawrence Berkeley National Laboratory who provided access to the aqua-planet simulations used in Chapter 4.

The author would like to thank his wife, Colleen Kaul of Stanford University without whose tireless proofreading many needless typographical errors would have likely gone uncorrected.

Chapter 1

Introduction

There is little doubt that water vapor plays an important role in determining the state of Earth's climate. In the vapor state, water influences the climate system radiatively as a powerful greenhouse gas (e.g. Pierrehumbet (1995)) as well as dynamically as the principal driver of hydrological cycle dynamics (Schneider et al., 2009). The equilibrium vapor pressure for water vapor (over a plane surface) is determined uniquely by the Clausius-Clapeyron equation, which has an exponential dependence on temperature (Wallace and Hobbs, 2006). Therefore, an exogenous radiative forcing that changes the mean earth surface temperature, such as anthropogenic climate change, is likely to affect the amount of water vapor in the atmosphere. Furthermore, because water vapor is a greenhouse gas, changes in the amount of atmospheric water vapor can amplify the mean earth surface temperature changes in response to the exogenous radiative forcing (Held and Soden, 2000). This feedback loop is referred to as the water vapor feedback and functions as a positive feedback (Hall and Manabe, 1999).

If the atmosphere were in an equilibrium state with regards to water vapor, as would pertain if the atmosphere were quiescent with uniform surface temperature and with only molecular diffusion for transport of mass and energy, then the vapor pressure of water on isothermal surfaces would be constant and equal to the equilibrium vapor pressure dictated by the Clasius-Clayperon equation. In this fictional state, the entirety of the hydrologic cycle would consist only of the equilibrium exchange (by evaporation and condensation) of water molecules between liquid and vapor states at plane surfaces of water located at the planet's surface. The atmosphere would therefore be everywhere precisely saturated. In reality, no such equilibrium condition exists, as is evidenced by the complexity of the observed hydrologic cycle.

In Earth's atmosphere there is a co-existence of sub-saturated, saturated, and super-saturated conditions with respect to water vapor. This coexistence is a result of three dimensional fluid transport and radiative cooling (e.g. Schneider et al. (2006) and Pierrehumbert et al. (2007)). Where conditions are sufficiently saturated, clouds form. Water vapor and clouds are intimately related.

While the title of this dissertation says nothing of clouds nor do clouds in particular

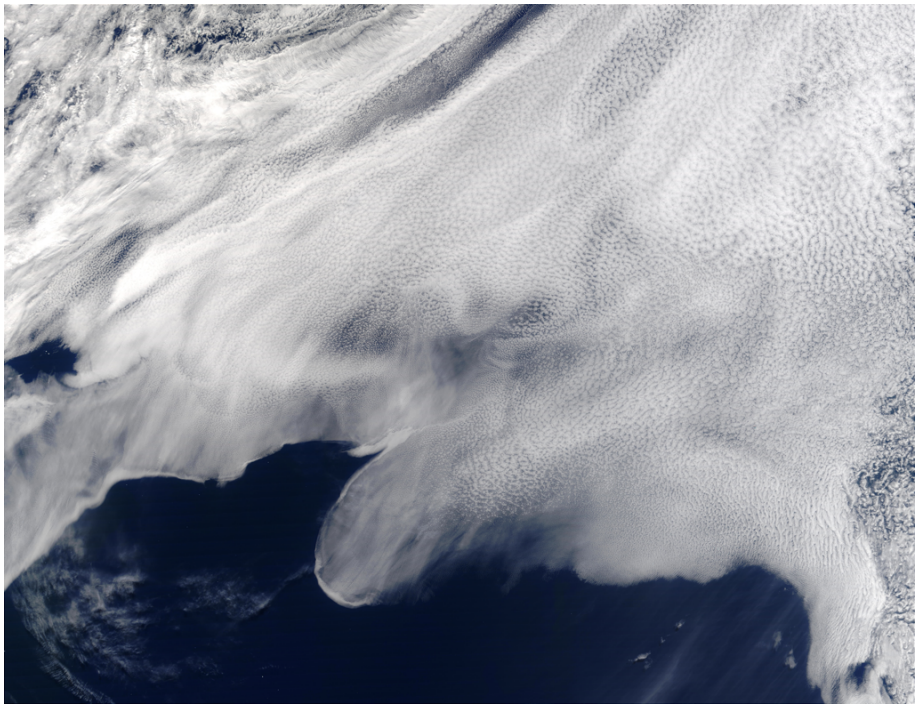

Figure 1.1: MODIS visible image showing the tremendous variability in clouds over a wide range of scales.

serve as a theme throughout this work, it is the representation of cloudiness in atmospheric models that serves as the primary motivation of the research described herein. Therefore, the introductory section of this work focuses on the effects of clouds in the climate system, uncertainties related to the representation of clouds in climate models, and strategies for reducing these uncertainties through observations. Finally, the subject of scale dependence and statistical scale invariance concludes the introduction and remains the primary theme throughout the rest of this work.

1.1 Cloud Radiative Effects

The only significant means of energy transfer between the earth system and the sun, and space is through radiative transfer. In an unperturbed climate equilibrated over sufficiently long times scales there exists a top of the atmosphere (TOA) balance between globally integrated incoming and outgoing radiative fluxes. The TOA incoming radiative flux is almost entirely of solar origin. The TOA outgoing radiative flux is composed of solar radiation which is scattered out of the atmosphere and emitted terrestrial radiation. The large difference in solar and terrestrial effective radiative temperatures allows solar and terrestrial radiation to be considered spectrally distinct. This distinction has lead to the use of terms shortwave

and longwave radiation to indicate solar and terrestrial radiation respectively.

Globally, clouds play an important role in determining the state of the equilibrium condition between incoming and outgoing radiative fluxes through their scattering of shortwave radiation and both absorption and emission of longwave radiation. The combined shortwave and longwave radiative effect of clouds leads to a cooling of $14 - 21$ Wm^{-2} in the contemporary climate (Ramanathan et al., 1989; Harrison et al., 1990).

1.1.1 Cloud Radiative Effects and Feedback

Figures 1.2 and 1.3 show the annual mean outgoing shortwave radiation at the TOA from a simulation of the pre-industrial climate as simulated by the Community Climate Systems Model (CCSM) (Collins et al., 2006). For the clear sky, Figure 1.2, the map of TOA outgoing shortwave radiation is essentially a map of surface albedo, as the bulk of shortwave radiation passes unimpeded through the clear atmosphere. In particular, maximum values of TOA outgoing shortwave radiation are associated with areas of high surface albedo, such as regions with permanent snow cover and deserts, while minimum values are associated with areas of low surface albedo such as oceans and forests. Figure 1.3, shows the map of TOA outgoing shortwave radiation with the effects of clouds included. The effect of clouds is to increase albedo through increased scattering of shortwave radiation out of the atmosphere. This effect is maximized over bodies of water, where in the absence of clouds incoming shortwave radiation is almost entirely absorbed. The globally integrated shortwave cloud effects approximately double the planetary albedo (Ramanathan et al., 1989), and lead to net cooling.

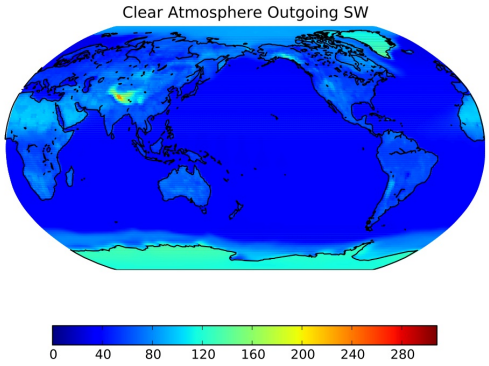

Figure 1.2: Annual average clear sky outgoing shortwave radiation as simulated by CCSM. The units are Wm^{-2}.

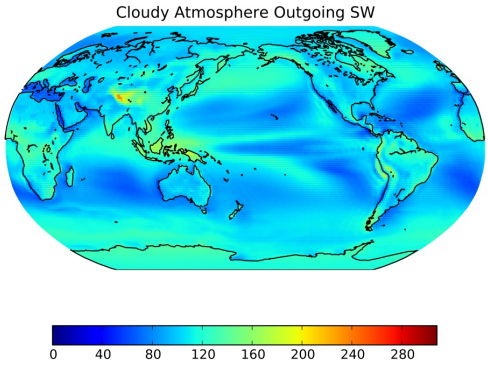

Figure 1.3: Annual average cloudy sky outgoing shortwave radiation as simulated by CCSM. The units are Wm^{-2}.

Figures 1.4 and 1.5 show the annual mean outgoing radiation from a CCSM simulation of

pre-industrial climate. For the clear sky, Figure 1.4, the map of outgoing longwave radiation is a map of the effective radiative temperature of the atmosphere, and is thus dependent on the vertical profile of temperature and concentration of greenhouse gases. In the cloudy atmosphere, depicted Figure 1.5, the effects of clouds are to reduce the outgoing longwave radiation through a mechanism analogous to the greenhouse effect. The cloud greenhouse effect is maximized in regions of high cold cloud tops which reduce the effective radiative temperature. The globally averaged longwave cloud radiative effect leads to an enhancement of the planetary greenhouse effect by 30 Wm^{-2} (Ramanathan et al., 1989; Harrison et al., 1990).

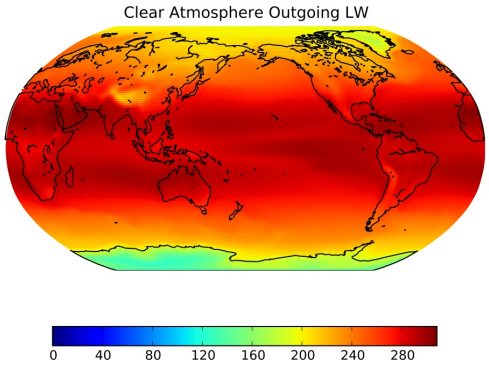

Figure 1.4: Annual average clear sky outgoing longwave radiation as simulated by CCSM. The units are Wm^{-2}.

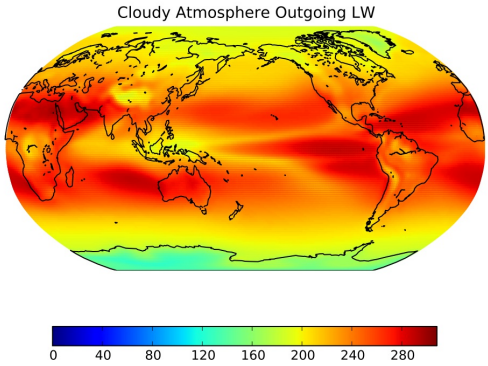

Figure 1.5: Annual average cloudy sky outgoing longwave radiation as simulated by CCSM. The units are Wm^{-2}.

The total cloud radiative effect, defined to be the sum of the shortwave and longwave radiative effects, is given by

$$CRE = \left(\uparrow F_{lw}^{clear} - \uparrow F_{lw}^{cloudy}\right) + \left(\uparrow F_{sw}^{clear} - \uparrow F_{sw}^{cloudy}\right) \tag{1.1}$$

where $\uparrow F_{lw}^{clear}$ is the clear sky outgoing longwave radiative flux, $\uparrow F_{lw}^{cloudy}$ is the cloudy sky outgoing longwave radiative flux, $\uparrow F_{sw}^{clear}$ is the clear sky outgoing shortwave radiative flux, and $\uparrow F_{sw}^{cloudy}$ is the cloudy sky outgoing shortwave radiative flux (Stephens, 2005). A plot of the mean cloud radiative effect from a simulation of pre-industrial climate by CCSM is given in Figure 1.6. Negative values of CRE correspond to mean cloud effects which lead to retention of energy by the climate system. The values of cloud radiative forcing are largely positive and are consistent with globally averaged cooling caused by cloud cover. Considerable negative correlation between shortwave and longwave radiative effects leads to cancellation, particularly in the tropics.

Any process which changes as a function of global mean surface temperature and directly or indirectly affects the TOA radiation budget may serve as a climate change feedback (Bony

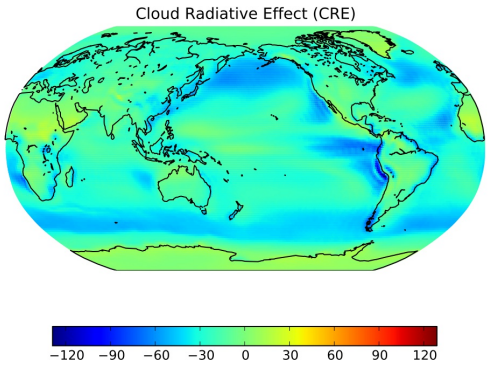

Figure 1.6: Mean cloud radiative effect (CRE) as simulated by CCSM. The units are Wm^{-2}.

et al., 2006). A process which functions as a climate feedback can act to either increase or decrease the sensitivity of the climate system to internal or external perturbations. Schneider (1972), building upon the ideas of Moller (1963), suggested that clouds could serve as a dynamical feedback to perturbations in surface temperature. Early modeling studies by Wetherald and Manabe (1988) found that cloud feedback processes lead to an increase in climate sensitivity. There has been much recent interest in cloud feedback as it has been identified as the most substantial source of uncertainty in Global Climate Model (GCM) predictions of climate sensitivity (Cess et al., 1996; Soden and Held, 2006; Solomon et al., 2007; Dufresne and Bony, 2008). Numerous cloud feedback pathways have been suggested in the literature which involve both boundary layer clouds in regions of large scale subsidence (Bony and Dufresne, 2005) and high clouds in convective regions (Lin et al., 2002).

The representation of cloud feedbacks in global climate models is a daunting problem. Evidence of cloud feedbacks resulting from changes in low and high clouds indicates that feedback phenomena are active in both the shortwave and longwave portions of the TOA radiation budget. The anti-correlation between longwave and shortwave cloud radiative effects means that depending on the sign of the shortwave and longwave feedbacks their interaction can be either constructive or destructive, which can obscure the source of model uncertainties (Stephens, 2005).

1.1.2 A Strategy for Reducing Uncertainties

Illingworth and Bony (2009) have proposed a two step strategy associated with reducing uncertainty in GCM representation of cloud radiative feedback. The two steps they propose are:

- "Determine what are the most critical uncertainties."

- "Determine how observations might be used to reduce some of these uncertainties."

Critical Uncertainties

Numerous efforts have been put forward to identify the critical uncertainties in cloud feedbacks. Bony et al. (2004) proposed a method to decompose changes in radiative properties into dynamic (macroscale) and thermodynamic (microscale) components through conditional averaging. Using this decomposition they showed that marine boundary layer clouds play a prominent role in producing cloud feedback related uncertainties in climate models (Bony and Dufresne, 2005). This result has also been confirmed by idealized model studies by Medeiros et al. (2008). Webb et al. (2006), using global and local feedback analysis and a local feedback classification system, showed that feedbacks involving low clouds were responsible for 59% of total inter-model feedback variance. By clustering cloud statistics from ensembles of climate models into cloud optical depth and cloud top pressure classes Williams and Webb (2009) showed that 47% of global variance in cloud radiative responses was from stratocumulus regimes while an additional 18% was from the transitional stratocumulus-cumulus regimes.

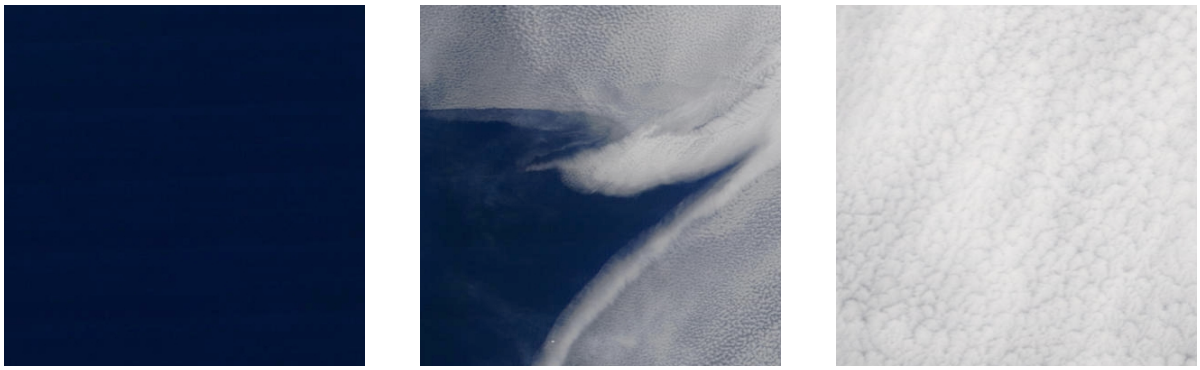

Figure 1.7: MODIS visible images that are of a spatial extent roughly the size of a single GCM gridcell. The images were extracted from the image shown in Figure 1.1. The left, center, and right subfigures represent clear, partially cloudy, and totally cloudy conditions respectively.

At current GCM grid resolutions, cloud variability is inherently a subgrid-scale property. Traditionally, many GCMs have taken an all or nothing approach to cloudiness, in which a GCM grid cell is considered to be either entirely clear or cloudy (Ose, 1993; Fowler et al., 1996). Figure 1.7 shows MODIS visible images of stratocumulus clouds over the Eastern Pacific Ocean, with each image's aerial extent roughly equal to the size of a single GCM grid cell. Both the partially cloudy scene (shown in the center panel of Figure 1.7) and totally cloudy scenes (shown in the right most panel of Figure 1.7) exhibit significant subgrid-scale variability. To account for this variability, many modern GCMs utilize statistical cloud schemes to represent the statistical properties of subgrid-scale cloud variability.

These schemes are based on the assumption that subgrid-scale cloud variability can be diagnosed from a knowledge of the probability distributions of subgrid-scale thermodynamic or moisture variables (Sommeria and Deardorff, 1977; Mellor, 1977; Bougeault, 1981). All statistical cloud schemes require that a distributional assumption be made about subgrid-scale variables, and that these distributions can be parameterized by gridscale GCM variables. Many statistical cloud schemes use the subgrid-scale probability density function of total water mixing ratio (q_t) as a basis for modeling cloud fraction (Tompkins, 2002). In general, distributional specification has been relatively ad hoc with triangular (Smith, 1990), uniform (Le Trent and Li, 1991), binormal (Lewellen and Yoh, 1993), Gaussian type (Lohmann et al., 1999; Bechtold et al., 1992), exponential (Bechtold et al., 1995), and beta (Tompkins, 2002) forms all being suggested and implemented.

The zeroth-order problem of a statistical cloud model is to predict grid-scale fractional cloudiness from PDFs modeling subgrid-scale variability. For illustrative purposes consider Figure 1.8 to be a schematic of a statistical cloud scheme based upon the subgrid-scale q_t variability. In a GCM the PDF of q_t denoted by $P(q_t)$ is parameterized by grid-scale variables. Assuming that the saturation mixing-ratio (q') can be determined from the grid-scale temperature, then the fractional cloudiness C can be determined by integrating $P(q_t)$ above the saturation mixing ratio

$$C = \int_{q'}^{\infty} P(q_t)\, dq_t. \tag{1.2}$$

This integral corresponds to the blue region in Figure 1.8. The information from the fractional cloudiness calculation can then be passed to microphysical and radiative transfer routines.

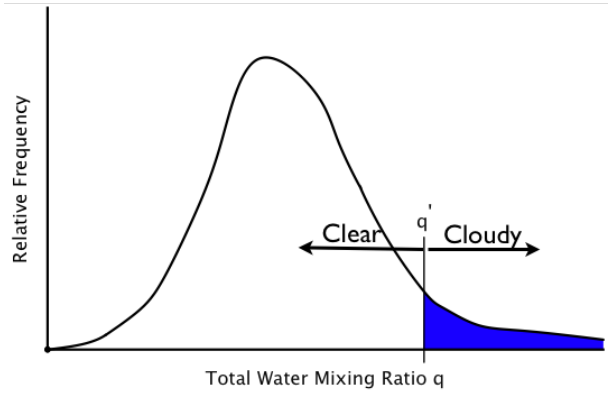

Figure 1.8: Schematic of a statistical cloud model. q is the total water mixing-ratio and q' is the saturation mixing-ratio.

In an effort to build statistical cloud schemes which are more physically consistent with other GCM components, Bony and Emanuel (2001) and Tompkins (2002) have proposed

and implemented prognostic statistical schemes which allow interaction of the cloud parameterization with turbulence and convection closures. Because prognostic statistical schemes solve a time dependent equation for the moments or parameters of the subgrid-scale PDFs, these schemes allow information regarding sub-grid scale cloud variability to be passed across GCM timesteps in a physically realistic manner.

Prognostic statistical cloud schemes are particularly amenable to observational constraint. Like most statistical cloud schemes, prognostic statistical clouds schemes are based on PDFs or joint PDFs of observable variables (Tompkins, 2003). This means that, given observations with sufficient spatial resolution, the PDFs upon which the schemes are based can be measured. For example, the Tompkins prognostic statistical cloud scheme assumes a beta PDF for the total water mixing ratio q_t, where

$$q_t = q_l + q_v + q_i \tag{1.3}$$

and q_l, q_v, and q_i are the liquid, vapor, and ice water mixing ratios respectively (Tompkins, 2002). The beta PDF $P(q_t)$ for $0 \leq q_t \leq 1$ is a two parameter distribution given by

$$P(q_t; \alpha, \beta) = \frac{1}{B(\alpha, \beta)} q_t^{\alpha-1} (1 - q_t)^{\beta-1} \tag{1.4}$$

where $B(\alpha, \beta)$ is the beta function and α and β are the distribution parameters. The parameters α and β can be written in terms of the first (μ_{q_t}) and second (σ_{q_t}) moments of the distribution as

$$\alpha = \mu_{q_t} \left(\frac{\mu_{q_t} (1 - \mu_{q_t})}{\sigma_{q_t}} - 1 \right), \tag{1.5}$$

$$\beta = (1 - \mu_{q_t}) \left(\frac{\mu_{q_t} (1 - \mu_{q_t})}{\sigma_{q_t}} - 1 \right) \tag{1.6}$$

Replacing the distributional first and second moments in Equations 1.5 and 1.6 with the sample mean and sample variance computed from an empirical data set gives the method of moments estimate for the parameters of the beta PDF that best emulates the properties of that data set. Thus, given an appropriate empirical data set, the model PDFs can be approximated and used to assess the distributional basis upon which the statistical scheme is built.

1.1.3 Countering uncertainty with observations

Despite the computational ease of constructing empirical PDFs it is not readily apparent which data sets can or should be used to compute the sample moments. Tompkins (2002) tested the assumed beta distributions using high resolution cloud resolving models (CRMs), and found the beta distribution provided a rather good fit to model computed histograms of total water mixing ratio. However, CRMs are not independent of their own modeling

assumptions, and are thus not optimal for this task. Observational data sets offer a clear alternative to CRM data for the purpose of constraining model PDFs, as they are independent of modeling assumptions. However, given that the hope is to constrain PDFs that model subgrid-scale variability in GCMs, the observed data set must be global in extent and of sufficiently high resolution to provide estimates of the PDF moments at near cloud scales. At present, there is no data set that provides both global coverage and cloud scale resolution.

One approach to solving this problem is to characterize the scale dependence of moments of spatial fluctuations of the water vapor field, using a combination of in situ observations, which provide high spatio-temporal resolution but lack global coverage, and remote sensing observations, which provide lower spatial resolution but nearly global coverage. If the scale dependent relationship for statistical moments of spatial fluctuations are relatively simple and universal across a wide range of conditions and scales, then the scale dependent relationship can be used to infer moments of spatial fluctuations at near cloud scale from coarse resolution data. A schematic of this proposed methodology is shown in Figure 1.9. In the schematic, the black vertical line in the middle of the figure represents the smallest observed scale of the coarse resolution data set, the solid blue line represents the scale dependence of moments of the coarse resolution data set, and the red dashed line represents the scale dependence of the moments of the high resolution observations. Characterization of the scale dependence of moments of spatial fluctuations of the water vapor field from global retrievals of water vapor mixing ratio at scales from 50 km and 500 km is the subject of Chapter 2 of this dissertation. Characterization of the scale dependence of moments of spatial fluctuations of the water vapor field at scales between 1 km and 100 km is the subject of Chapter 3 of this dissertation.

There are several methods for determining the scale dependence of moments of spatial fluctuations from data. In all cases, these methods attempt to measure the mean variability at a particular scale. Therefore, through the rest of this dissertation we will refer to the characterization of moments of spatial fluctuations as the characterization of the scale dependence of variability in order to avoid any potential confusion.

The scale dependence of the spatial variability of many atmospheric properties has been studied, including temperature (e.g. Nastrom and Gage (1985)), wind velocity (e.g. Nastrom and Gage (1985) and Frehlich and Sharman (2010)), trace gasses (e.g. Tjemkes and Visser (1994); Cho et al. (1999a,b) and Cho et al. (2000)) cloud properties (e.g. Davis et al. (1994, 1996)) and precipitation (e.g. Lovejoy (1982)). In all of these cases the observed scale dependence can be closely approximated by power laws. One example of scale dependent moments with power law behavior are the atmospheric energy spectra shown in Figure 1.10, which was taken from Skamarock (2004). In Figure 2.7, the energy spectra are related to the scale dependence of variance (e.g. Kahn and Teixeira (2009)). The existence of power law scale dependence of variability is an indicator of statistical scale invariance, which will be discussed in greater detail in Chapter 2. A few studies suggest power law scale dependence of moments of the atmospheric water vapor field from aircraft based observations (e.g. Nastrom et al. (1986), Cho et al. (2000), Kahn et al. (2011), and Fischer et al. (2012)) and satellite remote sensing observations (e.g. Tjemkes and Visser (1994) and Kahn and Teixeira (2009)).

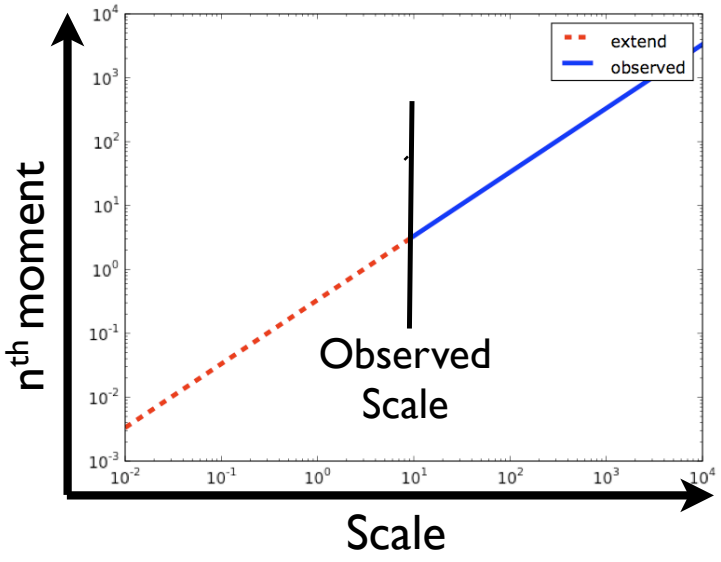

Figure 1.9: A schematic suggesting the proposed extension (extrapolation) of coarse resolution observations (blue solid line) to smaller scales based on a known scale dependence (red dashed line).

While several studies have characterized the scale dependence of variability of water vapor, they all suffer from two important limitations. In particular, the aircraft based studies tend to be limited to a fairly small number of flights and typically to a small set of meteorological conditions. In the case of studies based on satellite observations, the quality of their derived power law fits is not adequately addressed, so that the universality of the derived scale dependent relationships is difficult to ascertain. The research described in this dissertation sets out to establish the scale dependence of variability of the atmospheric water vapor field, to show the statistical scale invariance of the water vapor field across a wide range of scales, and to address its universality. Additionally, once the scale dependence is characterized based on observations, it can be compared to the scale dependence of variability in numerical simulations as a means of benchmarking simulations to observations (e.g. Kahn et al. (2011)).

1.2 Structure of Dissertation

The research results presented in this dissertation are contained in three chapters. In the first chapter, the scale dependence of water vapor variability is characterized by structure functions of the water vapor field as observed by the Atmospheric Infrared Sounder. The analysis of AIRS provides nearly global information about the scale dependence of water

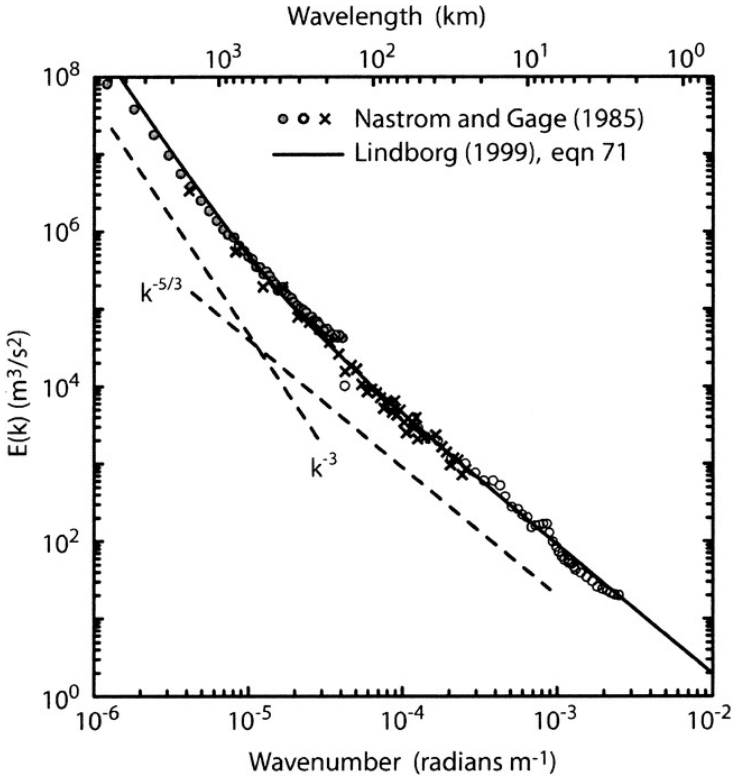

Figure 1.10: Kinetic energy wavenumber spectra based on aircraft observations from MOZAIC. The spectra show -5/3 power law scaling behavior at scales smaller than a few hundread km, and -3 power law scaling behavior at scales above approximately 800km. The plot is based on the results of Nastrom and Gage (1985) and a relationship derived by Lindborg (1999). (This figure is reproduced unaltered from Skamarock (2004).)

vapor at scales between 50km and 500km. In the second chapter observations made from the 396m level of the WLEF tower located in Park Fall, Wisconsin are used to characterize the scale dependence of water vapor variability across a range of scales extending form 1 km to 100 km. In the third chapter, high resolution aqua-planet simulations are used to characterize the scale dependence of water vapor in numerical simulations across scales ranging from 50 km to 500 km.

1.3 Scientific Contributions

- Structure Function Analysis of the AIRS Observed Water Vapor Field.
  - A methodology is developed to investigate statistical scale invariance based on the structure functions of remote sensing fields that are observed non-uniformly

in space. The methodology can be applied to compute any order of structure function given an appropriate data set.

- The structure function methodology is applied to physical retrievals of water vapor mass mixing ratio from the Atmospheric Infrared Sounder (AIRS), and is used to show that the first order structure function of the water vapor field exhibits scaling (power law behavior) between 50km and 500km, suggesting the statistical scale invariance of the water vapor field at mesoscales.
- For the first time the nearly global spatial and seasonal variation of first order structure function scaling exponents H are reported along with robust error estimates.
- The scaling exponents suggest the existence of free tropospheric and boundary layer scaling regimes with $H < 0.5$ and $H > 0.5$ characterizing the boundary layer and free tropospheric regimes respectively.
- It is hypothesized that the $H > 0.5$ behavior is related to the rapid generation of filamentary structures by two dimensional chaotic mixing.
- Maritime boundary layer exponents are shown to cluster around $H = 1/3$, which is consistent with other observations of boundary layer statistical scale dependence.

- Spatial Structure Functions and Detrended Fluctuation Analysis of Water Vapor Time Series Observed from the WLEF tower.
  - A methodology is developed to compute spatial structure functions and detrended fluctuation functions from observed time series using Taylor's Frozen Turbulence Hypothesis
  - The methodology is applied to observations from the 396m WLEF very tall tower located near Park Falls, Wisconsin.
  - Tower time series that are observed within the daytime convective mixed layer are shown to have scaling structure function and detrended fluctuation functions at scales up to at least 100km.
  - Convective mixed layer scaling exponents are shown to be consistent with approximate $H = 1/3$ behavior of structure functions and detrended fluctuation functions.
  - Tower time series that are observed in the nocturnal residual layer are shown to have scaling structure function and detrended fluctuation functions at scales at least as large as 100km.
  - Residual layer scaling exponents are shown to be consnstent with $H > 0.5$ behavior.
  - Convective mixed layer scaling exponents are shown to exhibit remarkable consistency with the free tropospheric and boundary layer exponents observed by AIRS.

- Structure function analysis of water vapor fields from aqua-planet simulations
  - Free tropospheric structure functions scaling exponents from a T340 resolution aqua planet simulation are shown to provide good qualitative and quantitative agreement with the zonal mean scaling exponents from AIRS as reported in Chapter 2, but simulations at T85 resolution do not agree as well with the AIRS results. This suggests that high resolution global climate models are successful in representing the physical processes responsible for transport and mixing of water vapor in the free troposphere.
  - Boundary layer structure function scaling exponents generally do not agree with the AIRS results at the T85 or T340 resolutions. This suggests that high resolution global climate models do not provide an adequate representation of transport and mixing of water vapor in the boundary layer, and that parameterizations based on gridscale estimates of water vapor variability must take these deficiencies into account.

Chapter 2

Scaling of Water Vapor Structure Functions as Observed by AIRS

2.1 Introduction

Generally speaking, a function $f(r)$ exhibits scaling if it has power law dependence on r such that

$$f(r) \propto r^{\alpha} \tag{2.1}$$

where α is called the scaling exponent. If the function $f(r)$ is a scale dependent statistic of a spatially or temporally distributed field, then scaling is an indicator of the statistical scale invariance of the field. Hereafter, statistical scale invariance will be referred to as scale invariance as is commonly done in the atmospheric science literature. The scaling of atmospheric energy and temperature spectra across a wide range of scales has been well established in the literature (Nastrom and Gage, 1985). In particular, Nastrom and Gage (1985) show that observed upper tropospheric wavenumber spectra of wind and temperature have a nearly universal form characterized by two scaling regimes. The first regime occurs within the mesoscale at length scales less than 400 km with a power law scaling exponent of -5/3, while the second regime occurs at scales greater than 400 km with a power law scaling exponent of -3.

Several studies have investigated the scale dependence of water vapor variability and have shown the presence of scaling behavior in water vapor spectra. Nastrom et al. (1986) find that observed water vapor wavenumber power spectra measured by commercial aircraft in the upper troposphere and lower stratosphere follow an approximately -5/3 scaling for scales less than 500 km to 800 km, and that the spectra suggest the existence of a scale break to a steeper scaling at scales greater than 800 km. Tjemkes and Visser (1994) find that water vapor power spectra spectra computed from High-Resolution Infrared Sounder (HIRS) measurements in the southern hemisphere storm track exhibit an approximately -5/3 wavenumber scaling in both the free troposphere and near surface across a wide range of scales. The scaling of trace gases as observed during the Pacific Exploratory Mission (PEM)

has been characterized by Cho et al. (1999a). They find that the wavenumber spectra of specific humidity have scaling exponents near -5/3 throughout the depth of the troposphere over scales ranging from 6 km to 60 km. Wood and Taylor (2001) show that water vapor power spectra from aircraft observations made below marine stratocumulus cloud layers exhibit scaling consistent with -5/3 at scales up to 80 km.

There is a growing body of literature that suggests the presence of significant deviations from the -5/3 power spectra scaling suggested by the aforementioned results. Kahn and Teixeira (2009), hereafter KT09, use physical retrievals of water vapor profiles from the Atmospheric Infrared Sounder (AIRS) to compute a global climatology of variance spectra scaling exponents. In particular, they find that maximum values of the spectral scaling exponents occur in the tropical mid-troposphere, and that scaling exponents show significant deviations from $-5/3$ behavior at scales ranging from roughly 100 km to 400 km. Additionally, KT09 find evidence of a very weak scale break that occurs at scales larger that 400 km in water vapor variance spectra, in contrast to the strong scale break they observe in coincident temperature variance spectra. Significant departures from -5/3 scaling behavior are shown by Lovejoy et al. (2010), who find aircraft observations of tropospheric humidity to be consistent with -2 wavenumber scaling from 4 km to 1000 km. Kahn et al. (2011) show that variance spectra for length scales between 10 km and 100 km computed from aircraft transects from the American Monsoon Systems Ocean-Cloud-Atmosphere-Land Study Regional Experiment (VOCALS-REx) exhibit vertical variability, with scaling exponents most consistent with -5/3 scaling in the near surface and becoming steeper with height.

If water vapor behaves as a passive scalar, and depending on the nature of atmospheric turbulence and the sources and sinks of water vapor, there are two theoretical spectra that may explain the observed spectra. The Obukhov-Corrsin spectrum predicts that passive scalars in locally isotropic turbulent flow will exhibit power spectra scaling with a -5/3 scaling exponent (Corrsin, 1951). However, if water vapor acts as a passive scalar forced at large scales, dissipated at small scales, and transported by a two-dimensional velocity field, then in steady state the Batchelor spectrum predicts that wavenumber spectra of such a scalar field should follow a -1 scaling between the forced and dissipative scales (Batchelor, 1959; Pierrehumbert, 1994). Based on the discussion of prior results, it seems that several of the studies suggest Obukhov-Corrsin type behavior, although, there are several reasons to question such an inference. First, the differences in horizontal and vertical tropospheric length scales suggest that the atmospheric flow field is not isotropic. Second, in several cases Nastrom et al. (1986); Tjemkes and Visser (1994); Cho et al. (1999a) the consistency with -5/3 scaling is confirmed based on comparison to reference spectra rather than explicitly computed scaling exponents, which limits the power of such conclusions. Finally, water vapor is a non-passive scalar interacting with atmospheric motions in a multiplicity of ways, including its role in large scale latent heat transport, its radiative effects as a greenhouse gas, and its enhancement of vertical motions through latent heat release in moist convection (Sherwood et al., 2010).

It is the non-passive nature of water vapor which makes the scaling of water vapor spectra relevant to the subgrid scale representation of moist processes in GCMs and drives the need

to further characterize the scale-dependent statistics of the water vapor field. Indeed, the nonlinear coupling between water in its various phases and the atmospheric flow occurs at all scales of atmospheric motion. The problem of GCM parameterization is one of scale dependence, in that it seeks to couple the simulated climate system to processes operating at scales that cannot be directly resolved by the GCM dynamical core (e.g. Williams (2005)). The scaling of water vapor spectra offers a direct means of connecting small scale variability to large scale variability. Scaling has been proposed as a way of estimating the subgrid scale water vapor variability in GCMs as a basis for statistical cloud parameterization (e.g. KT09, Cusack et al. (1999)) and as a means of comparing GCM representation of the spatial variability of water vapor to observed variability (Kahn et al., 2011). Despite the potential utility of observations of scale invariance in climate model development and verification, few studies have characterized the climatology of the scale invariance of the water vapor field.

Scaling of atmospheric spectra has been used to assess climate simulations. Kahn et al. (2011) use variance spectra computed from AIRS physical retrievals and aircraft observations from VOCALS-REx to investigate the consistency between water vapor variance spectra obtained from observations, free-running climate GCMs, and meteorological reanalyses. Their investigations suggest that reanalysis spectra provide better agreement with AIRS observed spectra than GCM spectra. However, in each case the spectral scaling exponents of modeled variance spectra are appreciably larger than observed exponents.

In this chapter we compute first order structure function scaling exponents for physical retrievals of water vapor mixing ratio obtained from AIRS. The goals of this chapter are to develop a methodology for estimating and interpreting the scaling exponents of water vapor structure functions that also considers the validity of underlying assumptions and the quality of the empirically derived scaling and to apply this methodology to investigate seasonal variations in the retrieved water vapor field from AIRS. Compared to existing approaches, this methodology introduces greater confidence in the computed exponents and places inferences of universality drawn from these results on a stronger empirical foundation. This chapter will proceed by discussing the definition of the structure function in the second section, the AIRS data set in the third section, the computation of directionally-independent and directional structure function scaling exponents in the fourth section, and the climatology of scaling exponents in the fifth section. In the sixth section the results are discussed in the context of the qualitative features of the water vapor field, and a summary and final remarks are given in the seventh section.

2.2 Structure Functions and Scaling

Most often the scale invariance of observed atmospheric data sets is determined through linear fits to log-log power spectra (log spectra versus log wavenumber) (Nastrom and Gage, 1985; Nastrom et al., 1986; Tjemkes and Visser, 1994; Cho et al., 1999a) or through linear fits to log-log structure functions (log structure function versus log scale) (Pierrehumbert, 1996; Marshak et al., 1997; Stolle et al., 2009). In this chapter we employ a structure function

methodology. The q-th order generalized structure function of a one-dimensional spatially varying field $\phi(x)$ is given by

$$S_q(r) = \langle |\phi(x_i + r) - \phi(x_i)|^q \rangle \tag{2.2}$$

where $\langle\rangle$ indicates an ensemble mean taken over all pairs of points $(x_i, x_i + r)$ separated by a distance r. The difference inside of the absolute value is typically referred to as an increment of the field ϕ and is denoted as $\Delta\phi$. The q-th order structure function therefore describes the scale dependence of the expected values of the q-th moment of increments of the field ϕ. In practice, because of the finite size of observational data sets, the ensemble mean in Equation 2.2 is approximated by the arithmetic mean over a finite the set of observed increments $\Delta\phi$. The Weiner-Khinchin theorem permits the second order structure function scaling exponent to be related to the Fourier power spectra exponent through the relation

$$\beta = -(\alpha_2 + 1) \tag{2.3}$$

where β and α_2 are the exponents of the Fourier power spectra and second order structure function, respectively.

In this chapter, we compute only the first order structure function scaling exponent, which we refer to as α. The primary reason for analyzing the first order structure function, rather than the second order, is that higher order structure functions are more susceptible to the effects of finite empirical data sets when approximating the ensemble mean in Equation 2.2 by an arithmetic mean. For some fields whose structure functions of various orders exhibit power law scaling, the scaling exponents of various orders of structure function can be related by the expression

$$\alpha_q = q\alpha \tag{2.4}$$

where α_q is the q-th order structure function scaling exponent and q is the order of the structure function. In this case, the field is monofractal, and a single scaling exponent is sufficient to completely characterize the scaling of all orders of its structure functions. Fields that exhibit structure function scaling but do not have this property are called multifractal or, synonymously, are said to exhibit anomalous scaling. Many atmospheric fields are known to exhibit a more complex relationship among the scaling exponents than that given by Equation 2.4 (e.g. Pierrehumbert (1996); Marshak et al. (1997); Stolle et al. (2009); Cho et al. (2000)). Cho et al. (2000) considered the mesoscale scaling of water vapor structure functions of order 0.5 through 10 as observed by a relatively small number of aircraft flights in the boundary layer and free troposphere. Their findings suggest that, despite clear evidence of anomalous scaling, using Equation 2.4 to approximate α_2 from α in Equation 2.3 will provide only a small overestimate (< 0.1) of β. This suggests that $\alpha_2 \approx 2\alpha$. Therefore, β can be related to α through Equation 2.3 by

$$\beta \approx -(2\alpha + 1) \tag{2.5}$$

as in KT09. To afford comparison to the rather limited prior results, conversion will be made between β and α using Equation 2.5 when necessary. Independent of the approximation made

in Equation 2.5, α provides considerable descriptive information about spatial correlations in the field ϕ.

The first order structure function scaling exponent (α) provides an efficient means of characterizing the spatial correlative structure of the observed field as an empirical approximation to the Hurst exponent (H), which is widely used to characterize stochastic processes (Hurst, 1956). Stochastic processes with $H > 1/2$ exhibit long range correlations and thus the increments of the processes exhibit persistence, in the sense that positive (negative) increments are expected to be followed by further positive (negative) increments. Random processes with $H < 1/2$ do not exhibit long range correlation and the increments of the process are antipersistent in the sense that a positive (negative) increment is expected to be followed by a negative (positive) increment. The Hurst exponent (and, therefore, the first order structure function exponent) of a one-dimensional random process is related to the fractal dimension D by $D = 2 - H$. Therefore, H characterizes the degree to which the random process fills space. Qualitatively, processes that are more space filling, as indicated by a larger fractal dimension D but smaller Hurst exponent H, are characterized by having a generally rougher appearance (Feder, 1988). In the discussion that is to follow we will assume that $H = \alpha$. In order to emphasize their equivalence, throughout the remainder of this chapter we will denote first order structure function scaling exponents by H.

For illustrative purposes, examples of two synthetic Gaussian random processes having Hurst exponents of 0.3 and 0.7 are shown in Figure 2.1, and computed structure functions and fitted power laws for each random process are shown in the inset plots. The random processes were generated using the circulent matrix method described by Wood and Chan (1994). It is clear from the inset structure function plots that both process are characterized by structure functions with power-law behavior and that the process with $H = 0.3$ has a rougher, more space filling appearance, which is characteristic of processes with antipersistent increments, while the process with $H = 0.7$ has a distinctly less space filling and smoother appearance that is characteristic of processes with persistent increments and long range correlations.

In this chapter, structure function scaling exponents H are computed from water vapor retrievals from AIRS. Computation and subsequent interpretation of first order structure function exponents estimated from two-dimensional data require the directional dependence of the structure function exponents to be addressed. Unlike time series, which vary only in the temporal dimension, two-dimensional spatially distributed fields may exhibit directional anisotropy resulting in directionally dependent structure functions and scaling exponents. The methodology described herein seeks to investigate the climatology of directionally independent and directionally dependent structure function scaling exponents.

2.3 The AIRS/AMSU Dataset

The AIRS/AMSU instrument suite combines AIRS, a high spectral resolution infrared spectrometer, with the Advanced Microwave Sounding Unit (AMSU) to retrieve the vertical profiles of tropospheric water vapor and temperature. The AIRS/AMSU instrument suite

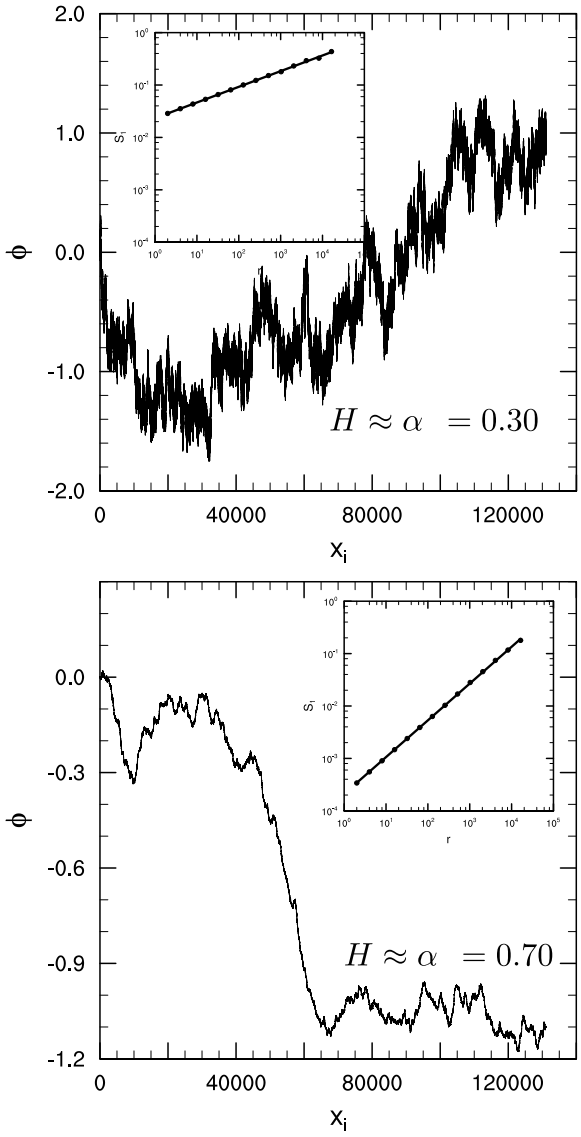

Figure 2.1: Two synthetic Gaussian random processes (ϕ) having Hurst exponents of $H \approx 0.3$ and $H \approx 0.7$ in the top and bottom panels respectively. The inset plot in each figure shows the first order structure function computed from the random process. The Hurst exponent estimated by least squares regression is also denoted.

is onboard NASA's sun-synchronous Earth Observing Satellite Aqua (0130 and 1330 local equator crossing times) and collects twice daily observations over most of the planet. AIRS provides physical retrievals of vertical profiles of water vapor mass mixing ratio (q_v) in scenes with up to 70% fractional cloudiness (Aumann et al., 2003). The vertical resolution of AIRS water vapor profiles are dependent on the local meteorological conditions. Maddy and Barnet (2008) estimate that the average vertical resolution is less than or equal to 3 km for all levels below 300 hPa based on analysis of AIRS empirical averaging kernels. Retrievals in partially cloudy scenes are achieved through a cloud clearing methodology as described by Susskind et al. (2003). This methodology combines single AMSU fields of view (FOV) with 3×3 grids of spatially coincident AIRS FOVs to produce cloud cleared radiances used for the subsequent retrieval process.

The spatial resolution of the AIRS data determines the smallest separation r for which we can compute structure functions, and hence it also sets the lower bound on the range of length scales for studies of scaling using these observations. The actual spatial resolution of AIRS observations depends upon the scan geometry and upon atmospheric conditions. Both AIRS and AMSU are cross-track scanning instruments, and therefore the horizontal spatial resolution degrades from a nominal 45 km-wide footprint (the areal projection of the instrument aperture on the Earth's surface) at nadir to a 150 km-wide footprint at the extremes of the scan lines Aumann et al. (2003). Furthermore, the cloud clearing methodology eliminates some fraction of the 9 AIRS coincident FOVs per AMSU FOVs that are impacted by cloudiness, thereby making the effective resolution for each retrieval dependent on cloud fraction (Susskind et al., 2003).

AIRS physical retrievals have been the subject of several validation studies, including comparisons against Atmospheric Radiation Measurement (ARM) site observations (Tobin et al., 2006), dropsondes (Pu and Zhang, 2010), radiosondes (Hagan et al., 2004; Divakarla et al., 2006), and aircraft measurements (Hagan et al., 2004; Gettelman et al., 2004). Validation studies have shown that AIRS performs to within the design error tolerance of less than 20% RMS error for water vapor mass mixing ratio observations. See KT09 for a more detailed discussion of AIRS validation.

For this study we use physical retrievals of water vapor mass mixing ratio from the AIRS Version 5 Level 2 Standard Product for December, January and February (DJF) in 2007 and 2008, and June, July and August (JJA) in 2008. Structure functions for ascending (daytime) and descending (nighttime) overpasses are computed separately in order to quantify the sensitivity of scaling to diurnal variations. Gettelman et al. (2004) have shown that AIRS loses sensitivity above 200 hPa where water vapor concentrations fall to less than 10 ppmv. Therefore, we limit the range of this study to pressure levels between 1000 hPa and 300 hPa to ensure the accuracy of the results. The AIRS data are quality controlled using the *PGood* quality indicator, which identifies retrievals that are of sufficient quality for statistical climate studies but may not be suitable for assimilation Olsen et al. (2007). Negative water vapor mixing ratio retrievals are excluded from the analysis. Additionally, as suggested by Olsen et al. (2007), we require that the estimated standard error of the retrieval be less than 50% of the retrieved value. In order to minimize any bias towards dry conditions in the data

set, no additional cloud masking is used in this study beyond the cloud screening already employed in the AIRS retrieval process.

Figures 2.2 and 2.3 show the AIRS three month mean water vapor retrievals for ascending (daytime) and descending (nighttime) overpasses at 925 hPa and 500 hPa, respectively. In order to conform with the AIRS pressure level convention, quantities reported on pressure levels in this chapter represent the mean values of those quantities between the stated level and the adjacent level above (in physical space). For example, water vapor retrievals reported at 925 hPa represent the mean water vapor mixing ratio between 925 hPa and 850 hPa. At both pressure levels the maximum values of water vapor mixing ratio occur in the ascending branch of the tropical circulation. At 500 hPa there is evidence of a subtropical minimum of water vapor mass mixing ratio associated with the subsidence branch of the mean Hadley circulation. There is a decrease in water vapor mixing ratio away from the tropics, which can be directly associated with the dependence of saturation mixing ratio on temperature as predicted by the Clausius-Clapeyron equation.

2.4 Computation of Structure Functions and Scaling Exponents from AIRS Data

For an arbitrary scalar field $\phi(\mathbf{x})$ of a two-dimensional argument $\mathbf{x} \in \mathbf{R}^2$ the first order generalized structure function is given by

$$S_1(\mathbf{x}, \mathbf{r}; \phi) = \langle |\phi(\mathbf{x} + \mathbf{r}) - \phi(\mathbf{x})| \rangle \tag{2.6}$$

where $\langle\rangle$ indicates an ensemble mean taken across all pairs of points $(\mathbf{x} + \mathbf{r}, \mathbf{x})$ for a large number of realizations of the field $\phi(\mathbf{x})$. The structure function exhibits scaling in a direction $\theta = \arccos \frac{(\mathbf{r} \cdot \mathbf{x})}{||r||||x||}$ if

$$S_1(\mathbf{x}, \mathbf{r}; \phi) \propto ||r||^{\alpha(\mathbf{x}, \theta)} \tag{2.7}$$

where $\alpha(\mathbf{x}, \theta)$ is the power law scaling exponent at $\mathbf{x}$ in the direction θ.

If the field exhibits statistical spatial homogeneity and isotropy, then Equation 2.6 loses dependence on the orientation of position $\mathbf{x}$ and separation $\mathbf{r}$ and can be simplified to

$$S_1(r; \phi) = \langle |\phi(\mathbf{x} + \mathbf{r}) - \phi(\mathbf{x})| \rangle \tag{2.8}$$

where the ensemble mean $\langle\rangle$ is now taken over all points separated by a lag distance $r = ||\mathbf{r}||$. In this case, the field exhibits scaling of the first order structure function if

$$S_1(r; \phi) \propto r^{\alpha}. \tag{2.9}$$

Recall that α (whether directionally dependent or independent) is considered to be equivalent to the Hurst exponent H in our analysis.

Previous analysis of variance scaling of the AIRS observed water vapor fields has implicitly assumed that the variance field is homogeneous and isotropic at scales of up to $12^\circ \times 12^\circ$

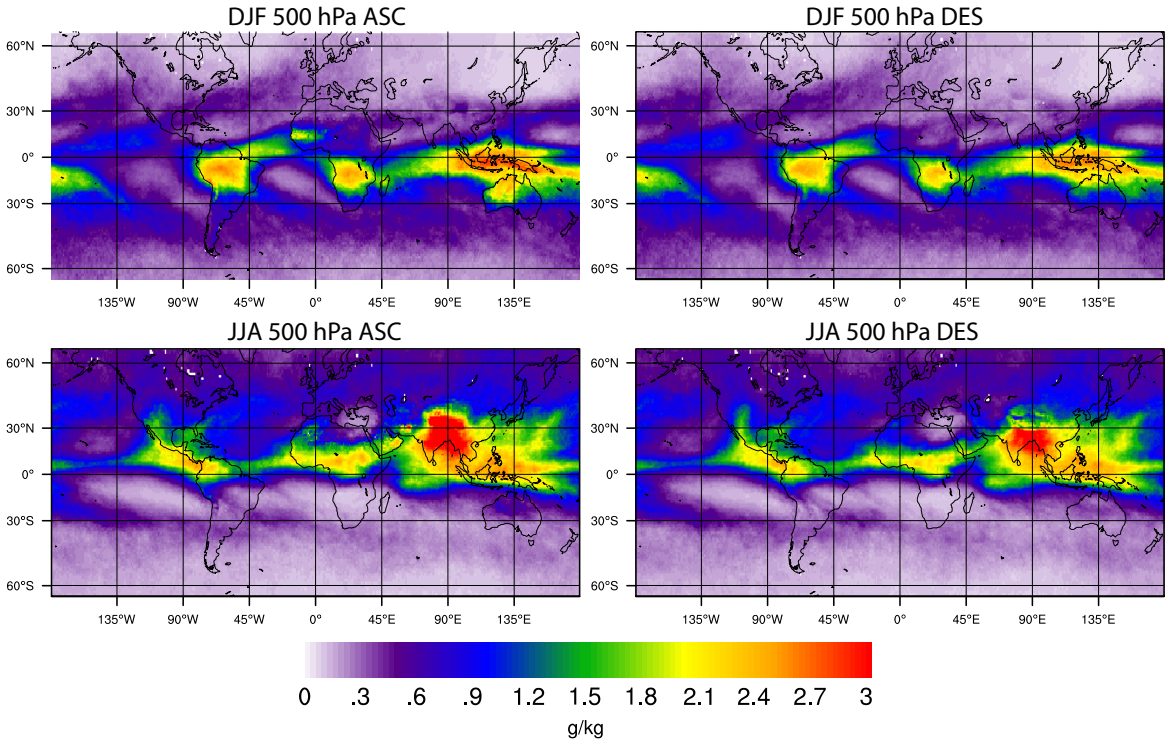

Figure 2.2: AIRS 500 hPa three month mean water vapor mass mixing ratio [g kg^{-1}] for Ascending (ASC) and Descending (DES) passes. Means are computed by binning individual retrievals to a 1.0° × 1.0° latitude-longitude grid. Masked values, appearing in white, represent grid boxes for which there are no successful AIRS retrievals during the analysis period.

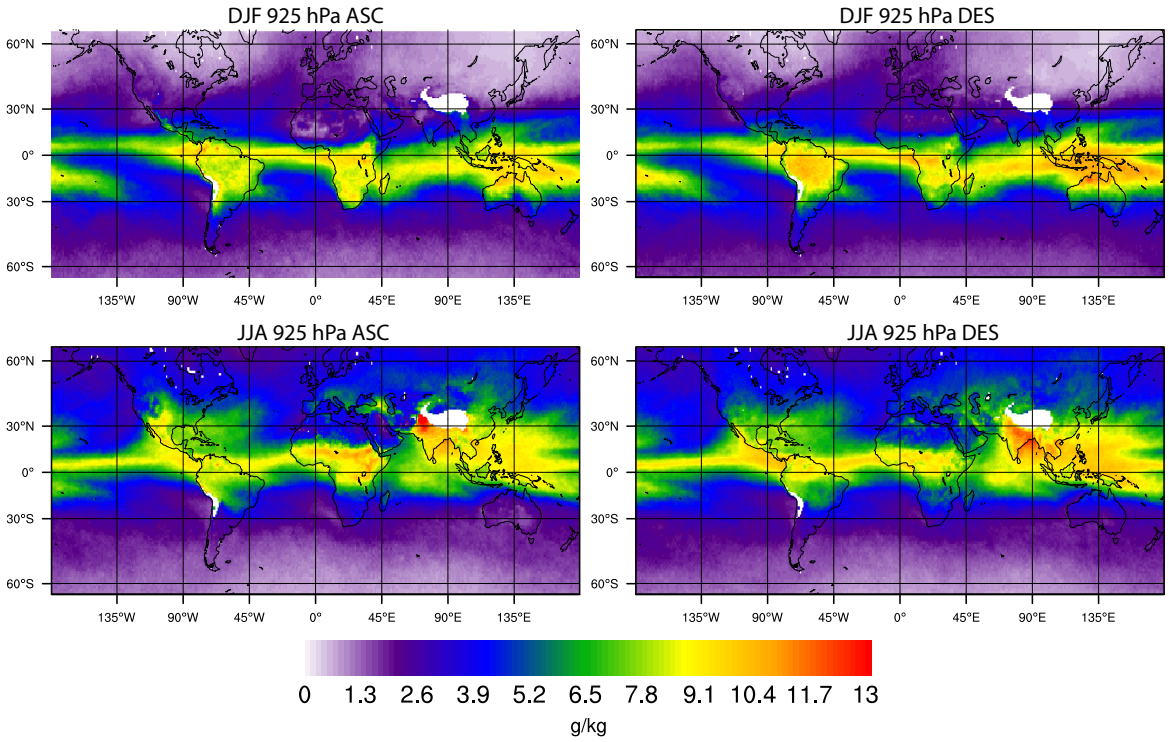

Figure 2.3: AIRS 925 hPa three month mean water vapor mass mixing ratio [g kg^{-1}]. Note the difference in colorbar between Figures 2.2 and 2.3. Means are computed by binning individual retrievals to a 1.0° × 1.0° latitude-longitude grid. Masked values, appearing in white, represent grids for which there are no successful AIRS retrievals during the analysis period.

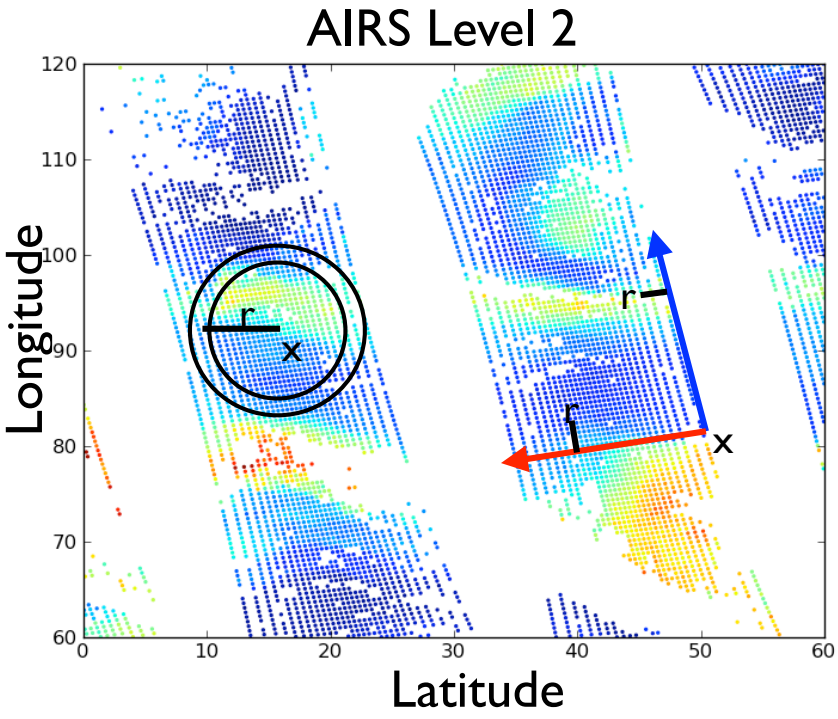

Figure 2.4: A schematic depicting the AIRS Level 2 water vapor mass mixing ratio field and blue and red arrow representing the across track and along track directions respectively. The black concentric circles represents the non directional structure functions for which increments are computed independent of direction for a given lag distance r.

in latitude and longitude (KT09). In order to quantify the anisotropy of structure function scaling we compute three separate structure functions. One structure function is computed from increments regardless of direction (directionally independent), a second from increments that are oriented in the direction of the satellite track (along-track), and a third for increments that are oriented normal to the satellite track (across-track). The along-track direction is oriented in a North-South direction as the ascending (descending) equator crossing occurs with an angle of 8° west of North (8° east of South). Because the along-track structure functions are computed from increments oriented in approximately the North-South direction, they are likely to be more affected by meridional gradients in the water vapor field than would the across-track or directionally independent structure functions.

Structure functions and scaling exponents are computed for overlapping domains centered every two degrees globally from 58°S to 58°N. The domains extend $12° \times 12°$ in latitude and longitude at the equator and increase in longitudinal width away from the equator in order to keep the area of the domain approximately constant. The choice of domain size ensures that there are a sufficient number of increments of each lag distance to provide an

approximation of the ensemble mean. Structure functions are computed by binning water vapor increments by lag distance r, where the lag distance for an increment is defined as the great circle distance between the locations of the retrievals composing the increment. Increments are accumulated for the entire period of analysis and are used to compute a single structure function for each domain. Structure functions are computed over a range of lag-distance bins that are non-overlapping and centered every 50 km between 50 km and 500 km inclusive. Figure 2.5 shows example along-track, across-track, and directionally independent structure functions. For the directionally-independent structure functions all increments, independent of direction, are binned by lag-distance, while in the case of cross-track (along-track) structure functions only increments which are normal (parallel) to the satellite ground track are binned. Finally, the arithmetic mean is computed for each bin in order to approximate the structure function. Structure function scaling exponents are determined by least squares fits to the log-log structure function between 50 km and 500 km. The range of scales has been selected to avoid relatively weak scale-breaks which have been observed in previous studies (KT09).

The exponent for each domain is then gridded according to the latitude and longitude of the domain center and plotted as a map. It is important to note that the exponents computed for each domain are estimated using data which are also used to compute scaling exponents for adjacent partially overlapping domains, and hence the exponents plotted on each map are not truly independent for separations smaller than half of the domain size.

In order to analyze the climatology of structure function scaling exponents it is necessary to identify structure functions exhibiting power law scale dependence. Two methods for identifying structure functions with power law scaling have been tested. The first method identifies structure functions as scaling when the ratio of the width of the linear regression slope parameter confidence interval to the regression slope itself is within an empirically-determined percentage threshold (Tuck, 2010). Due to the small number of degrees of freedom in the regression (the number N of lag distances $-$ 2), and since the width of the confidence interval is proportional to $1/\sqrt{N-2}$, this test tends to reject a large number of log-log structure functions for reasonable choices of the confidence interval width despite satisfactory linearity over the scaling range. We have considered an alternate method based upon setting an ad hoc lower bound on the coefficient of determination (R^2). This is mathematically equivalent to setting a minimum amount of the variance of the log-log structure function that is required to be explained by the linear regression in order for the structure function to be deemed as scaling. Tests have shown that the second method is successful in identifying scaling structure functions, and we adopt this alternate method with a lower bound on R^2 of 0.95 for the remainder of our analysis.

As previously mentioned, this study involves two periods of analysis, the first in boreal winter during December, January, and February of 2007 and 2008 and the second in boreal summer during June, July, and August of 2008. Over each period, increments are computed from each day's data. Then, the increments obtained on each day are combined to compute a single structure function for the entire three month period for each $12^\circ \times 12^\circ$ domain. Combining increments over the entire period to compute a single structure function and

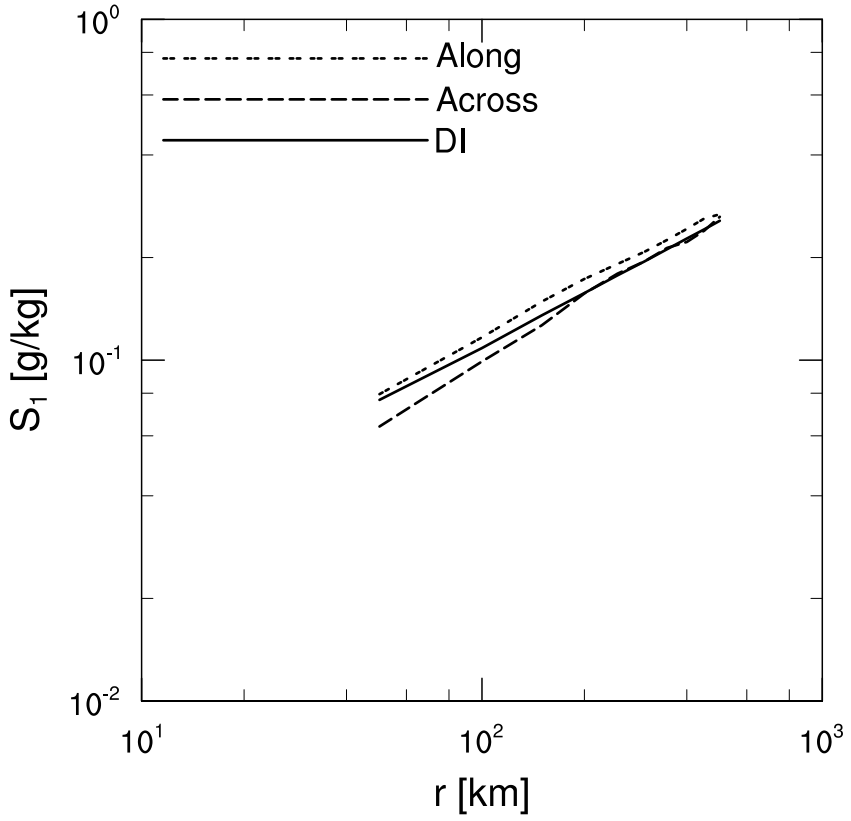

Figure 2.5: Example 500 hPa DJF ascending pass Along-Track (Along), Across-Track (Across), and Directionally-Independent (DI) structure functions for a structure function domain centered centered at 165°W and 51°N. The selection of this particular structure function domain is arbitrary.

scaling exponent requires the assumption that the increments are being sampled from a temporally statistically stationary field. It was found that a three month analysis period provided sufficient sampling to allow robust estimation of the ensemble means required by the structure functions.

2.5 Results

2.5.1 Maps of Scaling Exponents

Maps of structure function scaling exponents (H) over scales ranging from 50 km to 500 km computed from AIRS water vapor mass mixing ratio retrievals for the 500 hPa and 925 hPa levels for DJF 2007/2008 and JJA 2008 are shown in Figures 2.6 and 2.7, respectively. The scaling exponents for each $12^\circ \times 12^\circ$ domain have been plotted regardless of the $R^2 > 0.95$ quality of fit criterion. However, regions for which the $R^2 > 0.95$ quality of fit criterion is not met are indicated with black hatching. The near absence of hatching in the directionally-independent and across-track maps (the left two columns of Figures 2.6 and 2.7) suggests the presences of nearly ubiquitous structure function scaling. The exceptions to the nearly ubiquitous scaling of directionally-independent and across-track structure functions occur primarily in a few regions of the deep tropics for both 500 hPa and 925 hPa and at the northern and southern extremes of the domain of analysis for the 925 hPa level. The along-track scaling exponent maps indicate similar behavior for the along-track structure function in the subtropics and midlatitudes with nearly ubiquitous scaling behavior, but suggest the occurrence of widespread departures from structure function scaling in the tropics where the $R^2 > 0.95$ criterion is not met. The maps also suggest that there is a slight diurnal variation in the aerial coverage of the hatched regions, with the largest areal coverage occurring for the ascending (daytime) overpasses.

The coloration of the maps shown in Figures 2.6 and 2.7 has been intentionally selected to draw clear distinction between $H < 0.5$ and $H > 0.5$ scaling behavior. Cool colors are used to indicate $H < 0.5$ behavior and warm colors are used to indicate $H > 0.5$ behavior. It is then apparent that the most dominant feature of the maps is the distinction that can be made between the $H > 0.5$ behavior at 500 hPa and the $H < 0.5$ behavior at 925 hPa that is clearly apparent in the subtropics and midlatitudes. Additionally, in the directionally-independent and across-track cases, it is evident that a second obvious distinction can be made between equatorial scaling exponents with $H > 0.5$, on one hand, for subtropical and midlatitude exponents and $H < 0.5$ for tropical scaling exponents, on the other.

The similarities between directionally-independent, along-track and across-track scaling exponent maps for each case (across each row in Figures 2.6 and 2.7) suggest that the scaling is approximately isotropic, particularly outside of the tropics. Comparing the ascending (daytime) and descending (nightime) maps suggests the presence of some diurnal variation in scaling exponents, with larger diurnal variation of directional scaling exponents than of directionally-independent scaling exponents. Comparing the maps in Figure 2.6 with those in

Figure 2.7 indicates that there is strikingly little seasonal variability in the scaling exponent maps, with the general qualitative features remaining very similar between DJF and JJA. The most notable and obvious exception to the limited seasonal variation is the region of $H < 0.5$ at 500 hPa that appears in conjunction with the South Asian Monsoon during JJA. Additionally, the maps provide some evidence of a slight shift southward of the tropical $H < 0.5$ region at 500 hPa from DJF to JJA.

Very few studies have considered the spatial variability of scaling exponents. Therefore, there are a limited number of prior analyses to which these results can be compared. KT09 show maps of AIRS variance spectra scaling exponents on the 850 hPa and 300 hPa levels for two seasons, MAM and SON, making direct comparison to these results difficult. Nonetheless, the most obvious distinction between the maps shown here and those in KT09 is the lack of a distinct equatorial minimum in scaling exponents as has been observed here. However, the results do confirm the findings of KT09 and Lovejoy et al. (2010) that there are significant departures from the $H \approx 1/3$ ($\beta = -5/3$) behavior described by Nastrom et al. (1986) and Tjemkes and Visser (1994) across a similar range of scales as those reported here.

2.5.2 Zonal Mean Cross Sections

The zonal symmetry evident in the maps of scaling exponents shown in Figures 2.6 and 2.7 suggests the appropriateness of computing zonal means. Figure 2.8 shows zonal mean cross sections of maritime directionally-independent (left column), along-track (center column), and across-track (right column) scaling exponents computed for all AIRS layers between 1000 hPa and 300 hPa. The computation of zonal means has been limited to include only those exponents from maritime structure function domains (those having a land fraction less than 0.1) in order to avoid the effects of varying surface topography on the lower tropospheric zonal means, and hence are referred to as maritime zonal means. Additionally, in order to only include domains for which there is evidence of structure function scaling, only domains for which the $R^2 > 0.95$ quality of fit criterion is met are included in the computation of the zonal mean. Therefore, latitudes for which the $R^2 > 0.95$ criterion is not frequently met should be interpreted with substantial caution. We note that that the systematic breakdown of scaling of the along-track structure function in proximity to the equator is a robust feature at all pressure levels, and thus caution against attempts at interpretation of zonal means of along-track structure function scaling exponents within 15° of the equator at all pressure levels.

As with the maps shown previously, the coloration of the zonal mean cross sections shown in Figure 2.8 has been selected in order to draw a clear distinction between $H < 0.5$ and $H > 0.5$ scaling behavior. It is apparent from the plots that $H > 0.5$ characterizes the water vapor field in the midlatitude, subtropical, and non-equatorial tropical free troposphere at levels above 850-700 hPa and that $H < 0.5$ characterizes the water vapor field in the near surface and in the equatorial tropics at all levels. The location of the maximum zonal mean scaling exponent for each case is indicated with a black cross in Figure 2.8, and

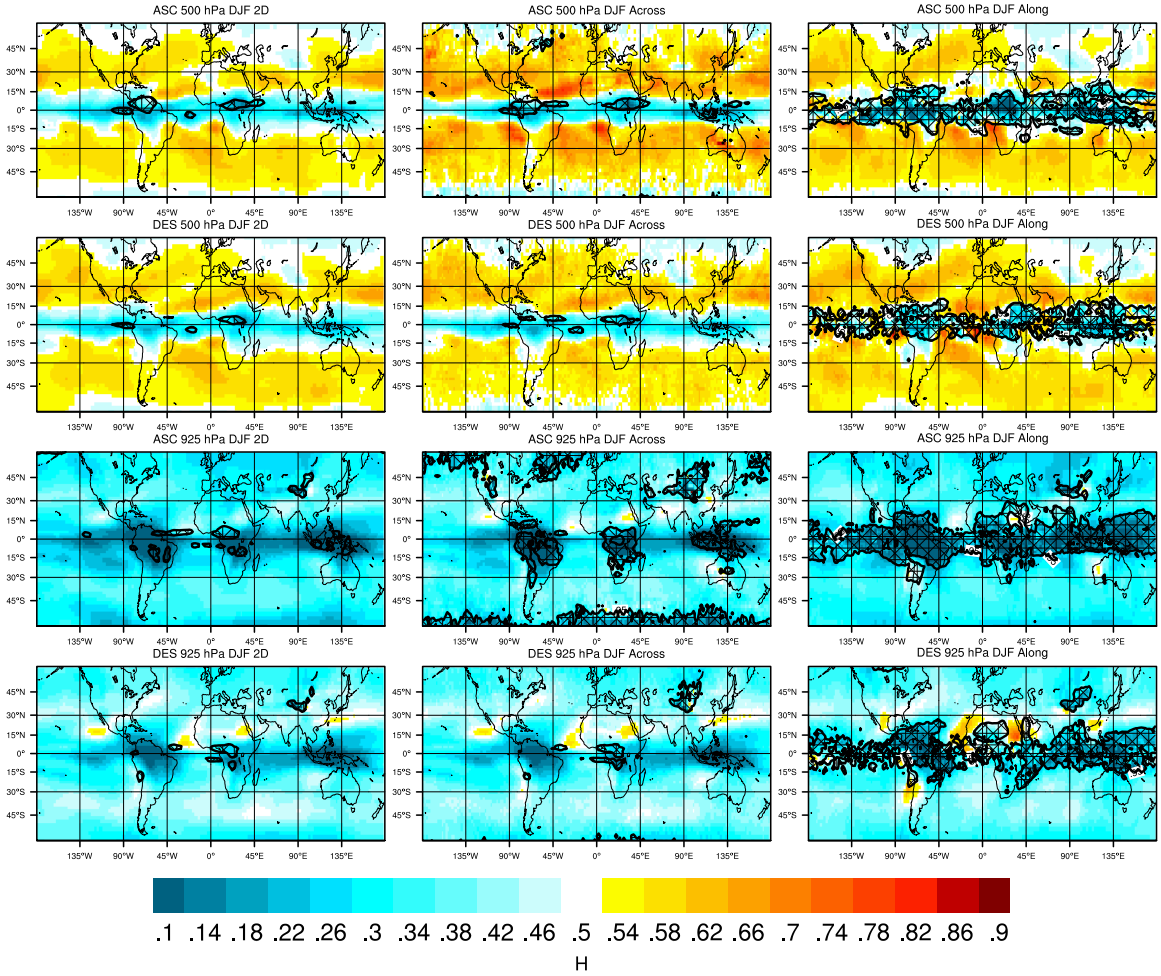

Figure 2.6: Maps of directionally-independent, across-track, and along-track scaling exponents (left, middle, and right column, respectively) for ascending (ASC) and descending (DES) passes during December, January, and February 2007 -2008 for the 500 hPa (top two rows) and 925 hPa (bottom two rows) AIRS retrieval levels. Regions for which the $R^2 > 0.95$ quality of fit criterion are not met are indicated with black hatching.

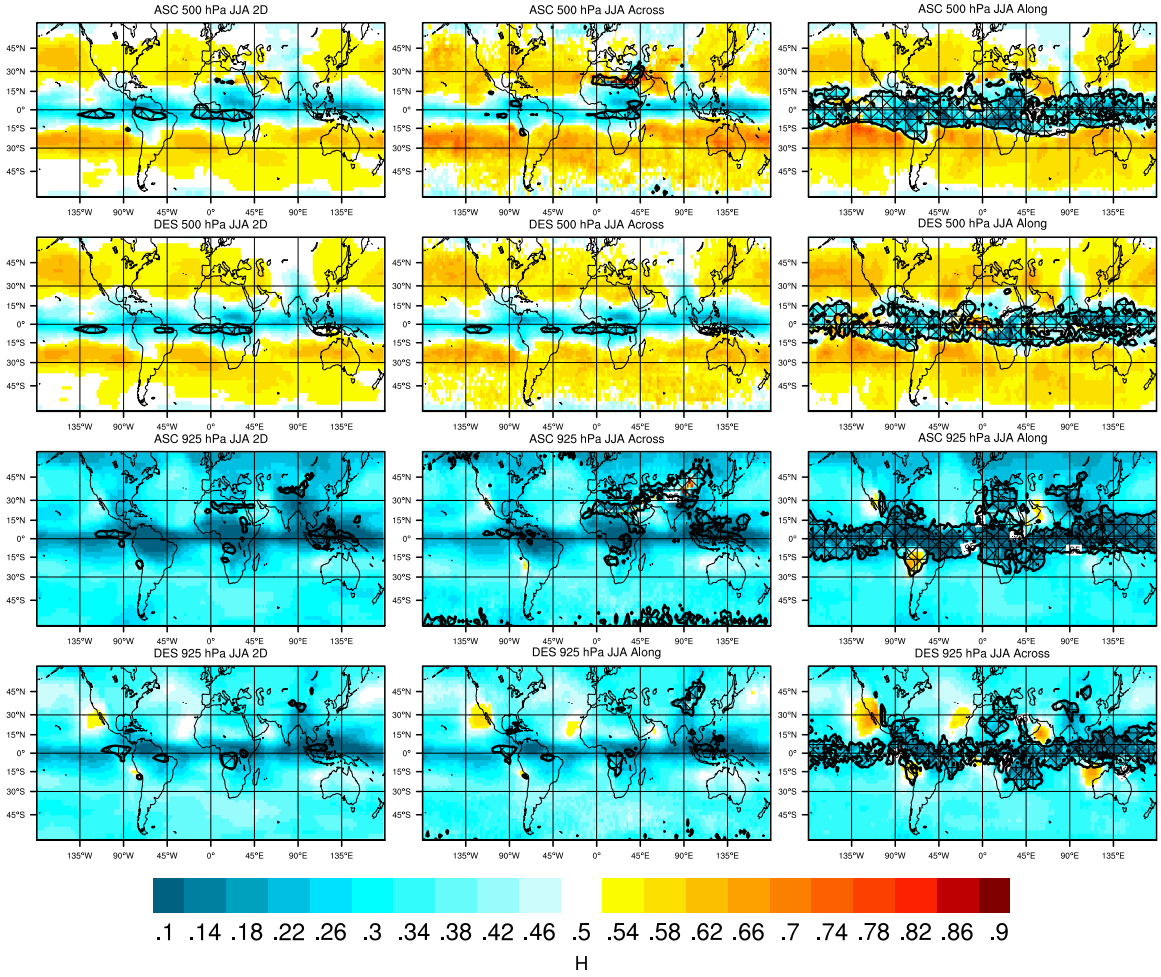

Figure 2.7: Same as Figure 2.6 but for June, July and August 2008.

typically occurs in the winter hemisphere near the margin between the tropics and subtropics at the 400 hPa or 500 hPa level. Poleward of 20° in each hemisphere the zonal mean directionally-independent and directional scaling exponents are similar, but the directional structure functions tend to be slightly larger than their directionally-independent counterparts.

There is clear evidence of diurnal variation in the near surface, which is apparent in Figure 2.8 as a downward migration of the 0.4 contour line between the ascending (daytime) and descending (nighttime) cases. The diurnal variation is approximately hemispherically symmetric for DJF, but during JJA the diurnal variation appears stronger in the northern hemisphere. We also note that the zonal mean directional structure functions exponents have a larger diurnal variation in the free troposphere than the directionally-independent structure function exponents. The causes of this difference are unknown. The amplified diurnal variation of directional scaling exponents is largest in the across-track direction, and

appears to mostly be related to increases in ascending pass (daytime) exponents leading to a larger apparent anisotropy for ascending pass exponents. Whatever the cause of the daytime anisotropy, by comparison the descending pass zonal means are indicative of considerably more isotropic conditions. Inspection of the 0.5 contour lines in Figure 2.8 shows that they do not undergo the same downward shift observed for the 0.4 contour lines. This suggests that, despite the observed diurnal variations in exponents, the relative apportionment of $H < 0.5$ and $H > 0.5$ fractional area coverage does not undergo a significant variation.

The diurnal cycle evident in the maritime zonal mean scaling exponents on the 1000 hPa and 925 hPa levels appears as a shift from values near 1/3 during the daytime to values closer to 0.4 at night (this is particularly evident in the probability density estimates shown in Figure 2.10, which will be discussed in more detail later), which is similar to the variation of scaling exponents across the top of the planetary boundary layer. Pressel et al. (2010) show that water vapor variance spectra observed at the 396 m level of a tall tower display a nocturnal increase in scaling exponents reminiscent of that evident in the AIRS zonal means. Similarly, Kahn et al. (2011) show water vapor variance spectra scaling exponents of 0.32 for VOCALs-REx flight segments below 700 m, with exponents increasing to 0.45 above 3000 m at scales ranging from 10 km to 100 km. Additionally, Cho et al. (2000) found a similar vertical variability at scales up to 100 km with scaling exponents varying from values near 0.25 in the boundary layer to higher free tropospheric values of 0.37 and 0.44 in the tropics and extratropics, respectively. Given these corroborating results, it is tempting to explain the AIRS observed diurnal variations as the results of diurnal variations in the planetary boundary layer. However, the vertical resolution of AIRS retrievals is dependent on the atmospheric vertical temperature gradient, which within the boundary layer undergoes significant diurnal variation and precludes a simple interpretation of the diurnal variation of boundary layer scaling exponents in terms of variations in boundary layer structure.

AIRS effective averaging kernels are a means of quantifying the retrieval vertical resolution (Maddy and Barnet, 2008). Effective averaging kernels are included in the AIRS Level 2 support product. The effective averaging kernels provide a measure of the vertical correlation in retrieved properties and hence provide a means of estimating the vertical extent over which a retrieval at a particular level exhibits sensitivity (Maddy and Barnet, 2008). The empirical averaging kernels do not necessarily sum to unity and significant departures from unity indicate dependence on the first guess used in the AIRS retrieval and loss of instrument sensitivity. Figure 2.9 shows mean averaging kernels for 2° latitude longitude boxes centered at $(31°\text{N}, 90°\text{W})$, $(0°\text{N}, 0°\text{W})$, and $(30°\text{N}, 50°\text{W})$, which we use to represent the qualitative characteristics of subtropical land, tropical ocean, and subtropical ocean averaging kernels respectively. The mean averaging kernels represent the arithmetic mean of averaging kernels for the 925 hPa, 700 hPa, and 500 hPa AIRS layers for all water vapor retrievals within the 2° latitude-longitude box during the DJF and JJA periods. In order to characterize the diurnal variation of AIRS vertical resolution and sensitivity, separate mean averaging kernels are reported for ascending and descending passes.

The mean averaging kernels in Figure 2.9 are intended to provide qualitative insight into the vertical resolution of the AIRS retrievals; more quantitative analysis would be useful

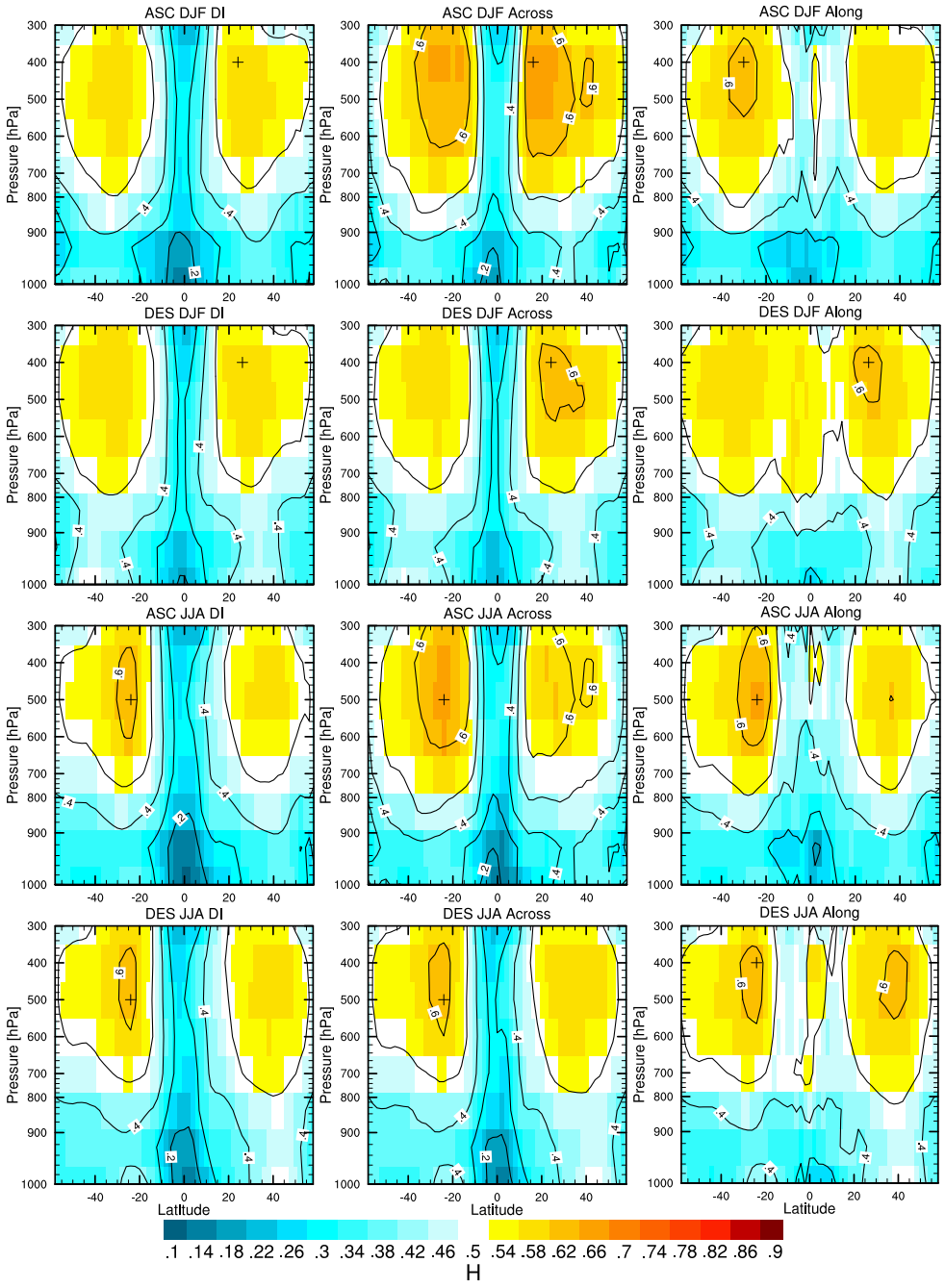

Figure 2.8: Zonal mean cross section of directionally-independent (left column), along-track (center column), and across-track (right column) scaling exponents for DJF 2007/2008 and JJA 2008 for all AIRS retrieval levels between 1000 hPa and 300 hPa. Scaling exponents determined from least squares fits with $R^2 < 0.95$ are not included in the computation of the zonal mean.

but is not required to support the primary effects summarized here. There are two primary features to note in Figure 2.9. First, there is a greater difference between ascending and descending pass mean averaging kernels at 925 hPa than at the other two levels. The shift to smaller values of the averaging kernel at night indicates a decrease in AIRS sensitivity from day to night. The change in sensitivity is likely related to diurnal variations in the lower tropospheric temperature profile. The nocturnal decrease in sensitivity appears to be more significant over land than over sea. Given that diurnal variations in the depth of the maritime boundary layer are typically rather small, we speculate that the observed diurnal variation in scaling exponents is a result of changes in the sensitivity of AIRS to variations in the near surface water vapor field. Second, it is apparent that the mean averaging kernels for the 700 hPa layer, which remain greater than zero below 925 hPa, suggest that for all cases water vapor retrievals are sensitive to water vapor fluctuations in the near surface. This suggests that the slow increase in mean scaling exponents from the near surface to the free troposphere that is evident in Figure 2.9 is likely related to the finite vertical resolution of AIRS and that AIRS profiles lack the vertical resolution necessary to resolve any abrupt transition that may occur at the top of the boundary layer. The 500 hPa averaging kernels appear to be predominantly independent of water vapor variations below 850 hPa, suggesting that 500 hPa retrievals are representative of the free troposphere.

2.5.3 Probability Density Estimates and Universality

The averaging kernels shown in Figure 2.9 suggest that the relatively smooth vertical variation in scaling exponents evident in the zonal mean cross-sections between the near surface (1000 hPa and 925 hPa) and the free troposphere (500 hPa, 400 hPa, and 300 hPa) may be the result of an inability of the AIRS retrievals to resolve abrupt transitions at the top of boundary layer. We therefore separate the remainder of the analysis into two distinct scaling regimes that the averaging kernels suggest are largely independent and are representative of the free troposphere and near surface. We take exponents computed on the 500 hPa and 925 hPa levels to be representative of the free troposphere and near surface, respectively. Given that the averaging kernels shown in Figure 2.9 suggest that the 925 hPa level exhibits mean diurnal thermodynamic variability, which is likely the source of changes in the instrument sensitivity, we will henceforth refer to the 925 hPa level as being representative of the boundary layer regime.

Probability density estimates of directionally independent maritime extratropical (poleward of 20°N and 20°S) scaling exponents from domains with nearly isotropic scaling and satisfying the $R^2 > 0.95$ quality of fit criterion are shown in Figure 2.10 for the 925 hPa and 500 hPa levels. Similar to the zonal means shown previously, the PDFs are computed from only maritime exponents. In order to limit the analysis to domains with nearly isotropic scaling, we require that the difference between along- and across-track scaling exponents be no more than 10% of the directionally-independent scaling exponent. Sensitivity tests suggest that both the distribution shape and statistics are relatively insensitive to the value of the anisotropy threshold over a range from 5% to 50%. Constraining the current analysis

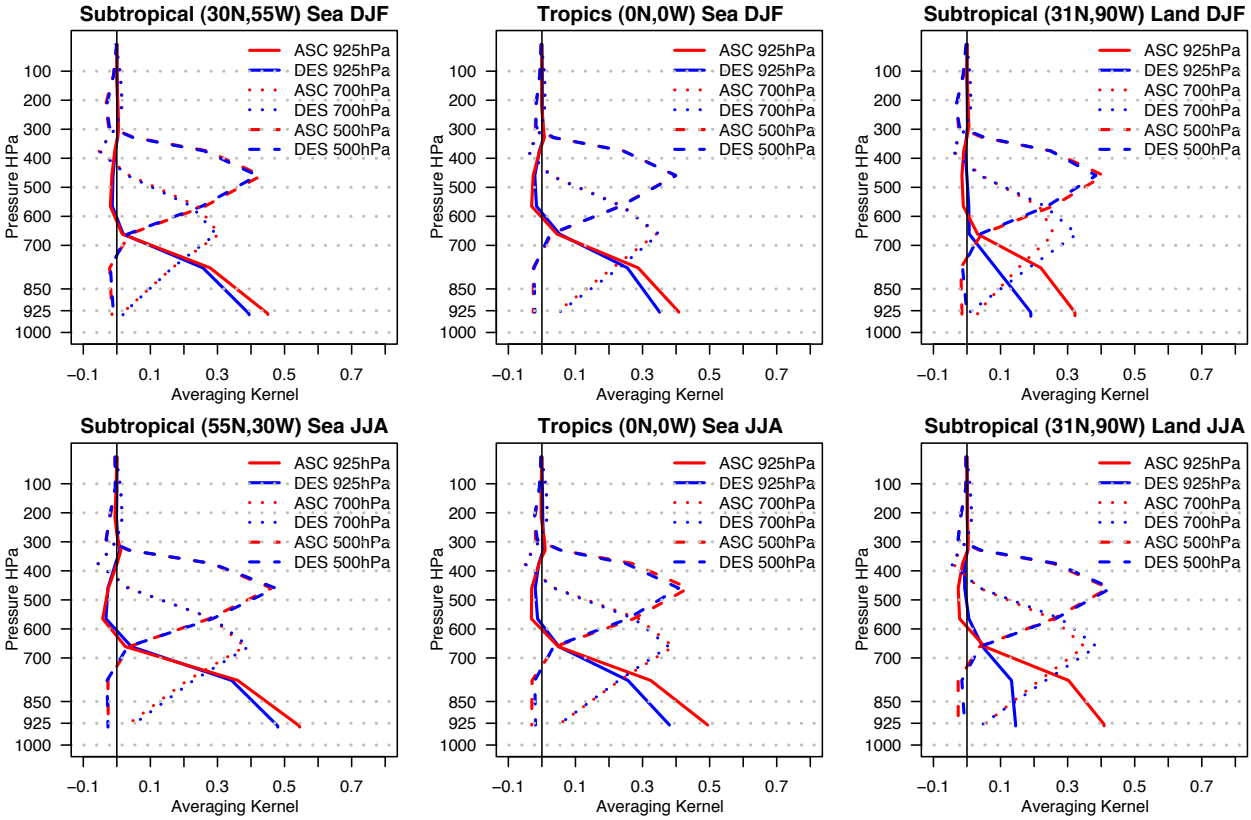

Figure 2.9: AIRS mean averaging kernels for the AIRS trapezoidal layers with effective pressure level closest to 925 hPa, 700 hPa and 500 hPa respectively for subtropical ocean (left column), tropical ocean (center column), and subtropical land (right column). Mean averaging kernels are the arithmetic mean for all vertical profiles within a 2^o latitude-longitude box centered on the latitude-longitude points given in the plot titles.

to nearly isotropic maritime extratropical scaling exponents serves two purposes: first, to remove the effects of topographic heterogeneities from the analysis and, second, to limit the effects of anisotropic scaling on the interpretation of directionally-independent exponents. Table 2.1 summarizes statistics of the exponent distributions shown in Figure 2.10 and also gives the percentage of maritime extratropical structure function exponents exhibiting nearly isotropic scaling. The table indicates that, with the exception of the DJF 925 hPa ascending case, the majority of extratropical structure function domains exhibit directionally-independent structure function scaling exponents. Therefore, density estimates shown in Figure 2.10 summarize the frequency distribution of structure function exponents for which there is strong evidence of scaling behavior (based on the R^2 criterion) and strong evidence of directionally-independent scaling exponents (based on the anisotropy threshold), conditions which characterize a large portion of the atmosphere.

		925 hPa				500 hPa			
		H	σ	95% CI	% scaling	H	σ	95% CI	% scaling
DJF	ASC	0.335	0.047	(0.333, 0.337)	44.6	0.556	0.047	(0.555, 0.558)	71.1
	DES	0.396	0.064	(0.394, 0.397)	80.2	0.561	0.065	(0.558, 0.562)	84.0
JJA	ASC	0.334	0.032	(0.332, 0.335)	70.0	0.548	0.067	(0.546, 0.549)	83.1
	DES	0.379	0.049	(0.378, 0.381)	75.8	0.549	0.042	(0.548, 0.551)	91.2

Table 2.1: The mean $\bar{H}$, standard deviation σ, and boot-strapped 95% confidence intervals for land masked extratropical (between 20°S – 58°S and between 20°N – 58°N) scaling exponents for which the absolute difference between along-track and across-track scaling exponents is less than 10% of the of the directionally independent structure function exponent value. Also given is the percentage of land masked structure function domains of directionally-independent, along-track, and across-track log-log structure function fits for which $R^2 > 0.95$, and for which the difference between along-track and across-track structure function exponents is less than 10% of the directionally-independent structure function exponent exponent value.

The density estimates for the 925 hPa level, which are representative of the boundary layer regime, are shown in the left panel of Figure 2.10. The displacements between solid and dashed lines of the same color are indicative of the diurnal variation in scaling exponents. Results of the averaging kernels analysis suggest that AIRS is most sensitive to boundary layer water vapor during ascending passes, and hence we will limit our discussion of the boundary layer scaling exponent frequency distributions to ascending (daytime) passes. The density estimates of daytime boundary layer regime estimates are unimodal with a peak occurring very near 1/3 (β= −5/3) for both DJF and JJA. The 95% bootstrapped confidence interval reported in Table 2.1 for DJF and JJA mean scaling exponents ($\bar{H}$) are $0.333 \leq \bar{H} \leq 0.337$ and $0.332 \leq \bar{H} \leq 0.336$ respectively. The bootstrapped confidence intervals are perhaps optimistically small as the scaling exponents are computed for structure function domains that are partially overlapping and hence not entirely independent. Nevertheless, we argue that given the independence of the DJF and JJA results, there is high confidence that $\bar{H}$ is near 1/3 over a range of scales from 50 km to 500 km.

There are relatively few studies that investigate scaling of water vapor over the range of scales from 50 km to 500 km to which the $\bar{H} \approx 1/3$ result can be compared. Perhaps the best comparison is to the results of KT09, who show near surface variance spectra scaling exponents to be roughly consistent with the $\bar{H} \approx 1/3$ behavior shown here and are similarly found to be consistent with the findings of Tjemkes and Visser (1994). Other studies have shown similar statistical scaling behavior, albeit over length scales typically shorter than 100 km (e.g. Cho et al. (2000); Wood and Taylor (2001); Comstock et al. (2005); Kahn et al. (2011)). These earlier results, taken in conjunction with the new results, appear to present building evidence of nearly universal $H = 1/3$ scaling at scales from below 50 km to 500 km in the boundary layer.

Scaling exponent density estimates for the 500 hPa level, which are taken to be representative of the free tropospheric regime, are shown in the right panel of Figure 2.10. The free tropospheric regime density estimates peak at 0.5. Table 2.1 shows that based on the bootstrapped 95% confidence interval, $\bar{H}$ likely lies in the range $0.546 \leq \bar{H} \leq 0.562$ for all cases, including both ascending and descending overpasses in DJF and JJA. Like the boundary layer regime, there is remarkably little seasonal variation in the observed exponents, which lends confidence in the precision of the result.

As in the boundary layer regime, there are relatively few results to which the free tropospheric regime results can be compared. These results confirm the general results of KT09, who report variance scaling exponents as large as 0.5-0.6 in some areas of the subtropical free troposphere. Moreover, the results reported here are found to support the results of Lovejoy et al. (2010), who estimated $H = 0.51$ for the free tropospheric humidity field. The free tropospheric regime results are found not to agree with the free tropospheric results of Nastrom et al. (1986) or Tjemkes and Visser (1994), who report scaling exponents that are more consistent with $H \approx 1/3$ behavior.

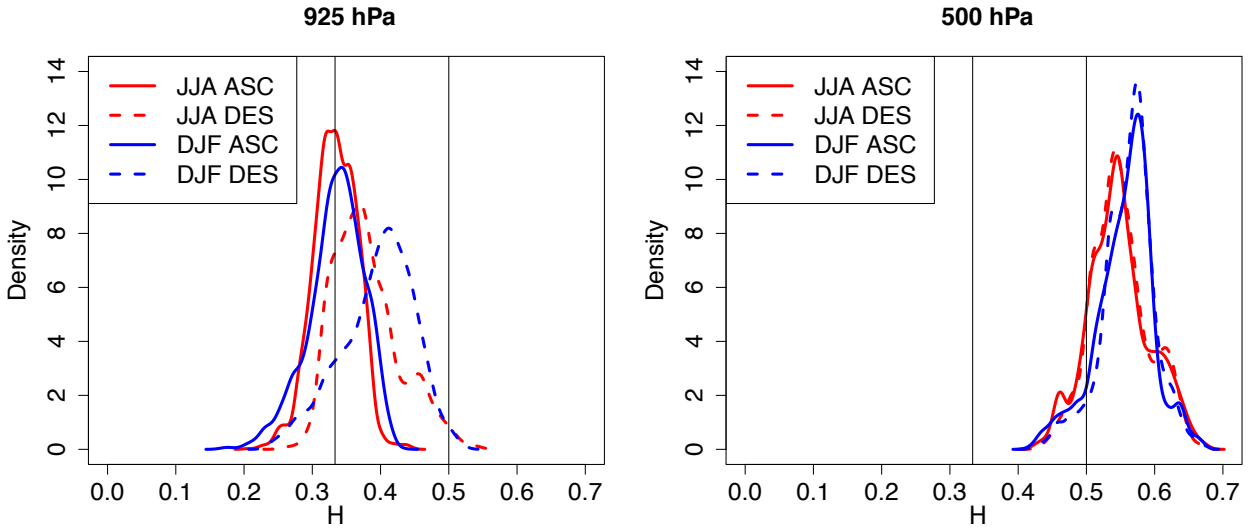

Figure 2.10: Estimated PDFs of along-track scaling exponents excluding the tropics (20°N to 20°S) for JJA and DJF ascending and descending passes. Scaling exponents for domains with land fraction > 10% are not included in the density estimate. The vertical lines represent reference values of 1/3 and 1/2.

2.6 Discussion

As is evident in Figure 2.1, the behavior of fields characterized by $H > 0.5$ and those characterized by $H < 0.5$ are tangibly different. Therefore, it is prudent to ask if there are qualitative features of the observed field that can provide a mechanistic explanation the vertical and horizontal distributions of exponents observed by this study. Structure functions are computed from spatial increments of the instantaneous water vapor field, hence the three month means shown in Figures 2.2 and 2.3 are not particularly useful for interpreting structure function behavior. Therefore, Figure 2.11 depict maps of water vapor mixing ratio from a single day's ascending passes for the 500 hPa and 925 hPa levels. These maps are taken to be representative of the instantaneous water vapor field. The quantity plotted in Figure 2.11 is the logarithm of the normalized water vapor mass mixing ratio, where the mixing ratio has been normalized by its global maximum value for each level. This normalization allows the plots to share a common colorbar and makes extratropical spatial gradients more visible. The two days shown in Figure 2.11 were not selected for any particular purpose other than to offer an example of the instantaneous water vapor field for both winter and summer seasons.

The left two panels of Figure 2.11 show the 500 hPa water vapor field. Perhaps the most striking features of the 500 hPa field are the filamentary structures that extend from the deep tropics into the midlatitudes. The filamentary structures are emblematic of large scale

two-dimensional chaotic mixing (e.g. Pierrehumbert and Yang (1993); Yang and Pierrehumbert (1994)). Yang and Pierrehumbert (1994) show that chaotic mixing processes in the free troposphere rapidly generate a wide spectrum of moisture filaments, and that within the midlatitudes these filaments lead to a fractal (i.e. $H > 0$) moisture field. They show that moisture filaments are initially generated by extrusion of moist air from the tropics through a partially permeable tropical mixing barrier. Within the tropics they show that the impediment to rapid exchange of moist tropical air with drier extra tropical air presented by the mixing barrier lead to a more homogeneous tropical water vapor field that does not exhibit fractal behavior (i.e. $H = 0$). Our results are largely consistent with both of these results, as we have shown clear $H > 0$ behavior throughout the extratropics that is clear evidence of fractal behavior. Additionally, we have shown a marked decrease in directionally-independent and across track scaling exponents in the tropics in conjunction with a systematic breakdown of along track structure function scaling.

We propose that the spectrum of filaments generated by chaotic mixing is responsible for the $H > 0.5$ free tropospheric behavior observed in this study. Chaotic mixing has been identified as important in determining the scaling of stratospheric scalar spectra (e.g. Haynes and Vanneste (2004)). Additionally, filamentary structures similar to those apparent in the water vapor field have been described in stratospheric scalar fields (e.g. Waugh (1996)) and numerous studies have shown these fields exhibit $H \approx 1/2$ scaling behavior at scales from 50 km to 500 km (e.g. Tuck and Hovde (1999),Tuck et al. (1999),Sparling and Bacmeister (2001)). In particular, Tuck and Hovde (1999) estimate H for stratospheric ozone field and found its mean, $\bar{H} = 0.56$, which is strikingly similar to the values for $\bar{H}$ reported for the water vapor field given in Table 2.1.

Considering the boundary layer regime, for which relevant instantaneous water vapor fields are shown in the right most panels of Figure 2.11, it is evident that while the boundary layer water vapor field is not completely devoid of filamentary type structures, they are considerably less distinct. This is likely a result of the fact that the existence of large scale gradients in the boundary layer water vapor field, similar to the gradients observed in the free troposphere, would be indicative of significant disequilibrium between the atmosphere and surface sources of water vapor. Hence, the large horizontal water vapor gradients associated with filamentary type structure are damped by fluxes of water vapor into the atmosphere from the surface. This allows local variations in the boundary layer to play a more dominant role in establishing the spatial variability of water vapor than is done by the large scale flow. While we do not propose a mechanism by which the boundary layer achieves the $\bar{H} \approx 1/3$ scaling of water vapor structure functions, it is apparent that the results of Wood and Field (2011) underscore the complicated interrelationship between boundary layer clouds and the water vapor field.

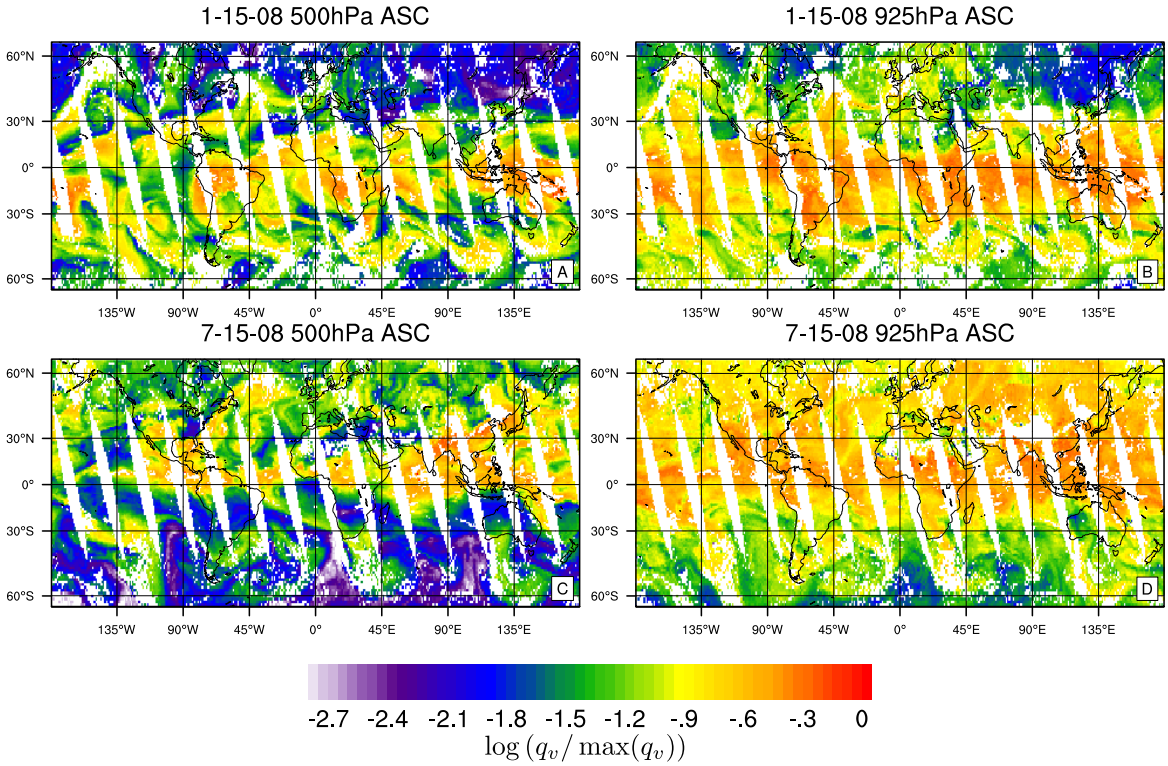

Figure 2.11: Plots of $\log(q_v/\max q_v)$ where q_v is the water vapor mass mixing ratio for a single day's ascending passes for 500 hPa and 925 hPa. This normalization allows the maps at 500 hPa and 925 hPa to be plotted with a single colorbar and emphasizes the filimentary structure of the extratropical water vapor field.

2.7 Summary and Final Remarks

In this chapter we have described a method for computing first order structure function scaling exponents from physical retrievals of water vapor mass mixing ratio from AIRS. Three separate first order structure functions are computed as part of the analysis, namely the directionally independent, across satellite track, and along satellite track structure functions. The three separate structure functions allow investigation of the directional dependence of the observed scaling. A threshold on the coefficient of determination of $R^2 > 0.95$ for the least squares fit to log lag versus distance log structure function is used to identify structure functions that exhibit power law scaling behavior.

The method is used to compute maps of structure function scaling exponents and zonal mean cross sections of maritime structure function scaling exponents for constant pressure surfaces ranging from 1000 hPa to 300 hPa between 58°S and 58°N. It is shown that directionally-independent and across-track structure functions exhibit nearly ubiquitous scaling while along-track structure functions tend not to exhibit scaling in equatorial regions. The maps and zonal means (Figures 2.6-2.7 and Figure 2.8 respectively) both suggest the presence of an equatorial minimum in scaling exponents at all levels. Outside of equatorial regions, both the maps and zonal means suggest the scaling exponents exhibit significant vertical variability, ranging from 0.3 in the near surface to values greater than 0.5 in the middle troposphere. Investigation of AIRS averaging kernels lead to the identification of two scaling regimes, one which characterizes boundary layer variability and a second which characterizes free tropospheric variability. The peaks in the probability density estimates of daytime boundary layer regime scaling exponents occur near 0.33 and transition to slightly larger values at night. The peaks in the probability density estimates of free tropospheric scaling exponents occur near 0.55 in both DJF and JJA cases and show significantly less diurnal variation than their boundary layer counterparts.

Therefore the extremely narrow confidence intervals, the agreement between DJF and JJA density estimates, and the agreement with prior results, all provide evidence that $\bar{H} \approx 1/3$ provide a relatively universal characterization of boundary layer structure function scaling poleward of 20° in each hemisphere at scales from below 50 km to at least 500 km. This result has several significant implications. First, the scale-invariance implied by the nearly isotropic scaling of structure functions indicates that AIRS observed scale dependent spatial variability may be extrapolated to smaller scales. A similar conclusion has been drawn by KT09. Second, there is strong empirical support for GCM parameterizations that seek to represent sub-grid scale variability based on the downscaling of grid scale variability (e.g. Cusack et al. (1999)), given that the model grid scales provide an accurate estimate of grid scale variability. Third, recent work by Wood and Field (2011), shows that the distribution of cloud horizontal sizes, power law scaling with an approximately -5/3 exponent across scales ranging from 0.1 km to 1500 km. They propose a bounded cascade model that assumes the water vapor field exhibits scale-invariance characterized by $H = 1/3$, and the results reported here offer significant support for this modeling assumption.

Additionally, there is significant confidence that free tropospheric water vapor field ex-

hibits behavior with $H > 0.5$. We argue that this could be explained by the generation of filimentary structures in the water vapor field that are the result of chaotic mixing processes as described by (Yang and Pierrehumbert, 1994)

The structure functions analysis reported herein has been limited to the first order structure function, but extension to other orders of structure functions may provide a fuller characterization of the scale dependence of water vapor variability. Also, structure functions are estimates of the moments of scale dependent increment probability density functions (PDFs), analysis of the climatology of these PDFs directly may prove fruitful in understanding the underlying stochastic process that generate the observed scale dependence, and provides another means of inter comparing observations and simulation. The success of this methodology suggests that its application to other AIRS retrieved fields may provide further insight into the the scale invariance of atmospheric fields.

Chapter 3

Spatial Structure Function Analysis of Water Vapor Time Series from a Very Tall Tower

3.1 Introduction

Recently the nearly global climatology of the statistical scale invariance of the water vapor mass mixing ratio has been investigated using physical retrievals from the Atmospheric Infrared Sounder (AIRS) by Kahn and Teixeira (2009) and in Chapter 2. They show that water vapor variance spectra (Kahn and Teixeira, 2009) and water vapor first order structure functions (Chapter 2 of this dissertation) exhibit scaling that is not consistent with the $-5/3$ scaling of water vapor power spectra that has been observed in the upper free troposphere (Nastrom et al., 1986; Tjemkes and Visser, 1994). However, within the boundary layer, both Kahn and Teixeira (2009) and Chapter 2 of this dissertation show scaling consistent with the $-5/3$ power spectra scaling that has been observed by aircraft and buoy measurements in the boundary layer (e.g. Cho et al. (1999a), Cho et al. (2000), Wood and Taylor (2001), Comstock et al. (2005), and Kahn et al. (2011)). A primary motivation for the investigation of the statistical scale invariance of the water vapor field is to provide an empirical basis for the parameterization of sub-gridscale variability in GCMs (e.g. Cusack et al. (1999)). While satellite observations can play a key role in constraining the scale dependence of water vapor variability at GCM gridscales across a wide range of meteorological and climatological conditions, they do not offer sufficient horizontal resolution to interrogate the statistical properties of water vapor variability at the scales below the GCM gridscales that are of immediate interest to the problem of parameterization.

A second disadvantage of remotely sensed satellite observations is the relatively coarse vertical resolution of passively retrieved quantities, such as physical retrievals of the vertical profile of water vapor from AIRS, that obscures potentially significant vertical gradients in atmospheric quantities. In Section 2.5.2 of this thesis, it is hypothesized that the relatively

smooth vertical gradient in AIRS water vapor structure function scaling exponents between the boundary layer and free troposphere is explained by the relatively broad averaging kernels for AIRS water vapor retrieval shown in Figure 2.9.

In situ observations offer an alternative to low vertical resolution satellite observations, however they are typically limited in areal coverage and temporal extent. This is particularly true for in situ observations of tropospheric water vapor which are limited to the relatively sparse global radiosonde network (e.g. Soden and Lanzante (1996)) and aircraft transects (e.g. Marenco et al. (1998)). One relatively underutilized observational platform which provides long term high temporal resolution in situ observations of water vapor, both in and above the planetary boundary layer, are observations from very tall towers (e.g. Berger et al. (2001)).

One caveat of using tall tower observations in studying spatial statistical scale invariance is that tall towers do not directly observe spatial variability. Utilization of time series of point measurements to explore the spatial variability of water vapor field requires use of Taylor's frozen turbulence hypothesis (e.g. Pope (2000)) in order to approximate a spatial domain from the directly measured temporal domain. Numerous studies have used Taylor's hypothesis to investigate the scale dependence of atmospheric variability from aircraft transects (Nastrom and Gage, 1985; Gage and Nastrom, 1986; Lovejoy et al., 2009; Lindborg et al., 2010) and buoy measurements (Comstock et al., 2005). The goal of the research described in this chapter is to use in situ observations from a very tall tower to investigate statistical scale invariance in the daytime convective boundary layer and the nocturnal residual layer.

In this chapter, a methodology is developed which allows the investigation of the spatial statistical scale invariance of the water vapor field by analysis of tall tower time series. The developed methodology is applied to water vapor observations from the 396 m level of the WLEF tower. The WLEF tower is a 447 m tall broadcast tower located in northern Wisconsin. It is shown that the observed data set allows investigation of the spatial variability of water vapor in and above the planetary boundary layer.

This chapter is structured as follows: In the second section, the WLEF data set, sampling methodology and an observational strategy which allows observed time series to be composited into boundary layer and above boundary layer cases is described. In the third section, a methodology utilizing structure function analysis and detrended fluctuation analysis to assess statistical scale invariance is described. In the fourth section, the results of an application of the methodology are presented. In the fifth section, the results from the analysis of the WLEF dataset will be compared to the results of analysis of the AIRS observed water vapor field that have been shown in Section 2.5 and in Chapter 2.

3.2 The WLEF Tower and Dataset

The 447 m WLEF television broadcast tower is located near Park Falls, Wisconsin (45.95°N, 90.27°W) at a tower base elevation of 472 m above sea level (Berger et al., 2001). The tower and surrounding environment are shown in Figure 3.1. The geographical location of the

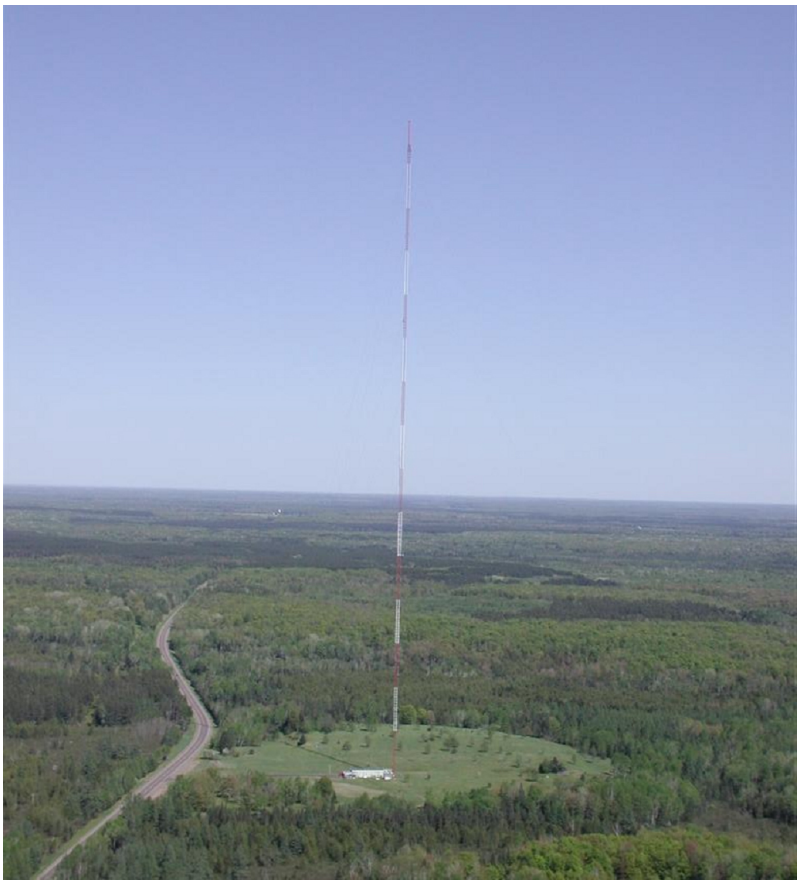

Figure 3.1: The 447 m WLEF television broadcast tower located near Park Falls, WI. (Image Credit: The North American Carbon Program)

tower is shown in Figure 3.2. The surrounding forest ecosystem is characterized by a largely heterogeneous mixture of mature deciduous forests in the uplands, lowland wetlands that are populated by mixtures of deciduous and coniferous trees, and more recently logged areas that are largely composed of younger aspen trees (Davis et al., 2003). The peak forest canopy height is approximately 25 m, and the tower is surrounded by a clearing with a radius of approximately 200 m. A detailed description of the forest ecology surrounding the WLEF site is given in Mackay et al. (2002). The topographical relief is characterized by rolling hills, with lowland to upland elevation differences of approximately 20 m over spatial scales of approximately 200 m (Davis et al., 2003).

The WLEF tower observational platform has been designed to synthesize measurements taken at multiple tower heights to provide observed time series of vertical profiles of mean CO_2 mixing ratio, CO_2 fluxes, sensible heat flux, and latent heat flux. The observed fluxes are computed from the observed variables by eddy covariance techniques (Berger et al., 2001). Computation of the aforementioned fluxes using eddy covariance techniques necessitates high

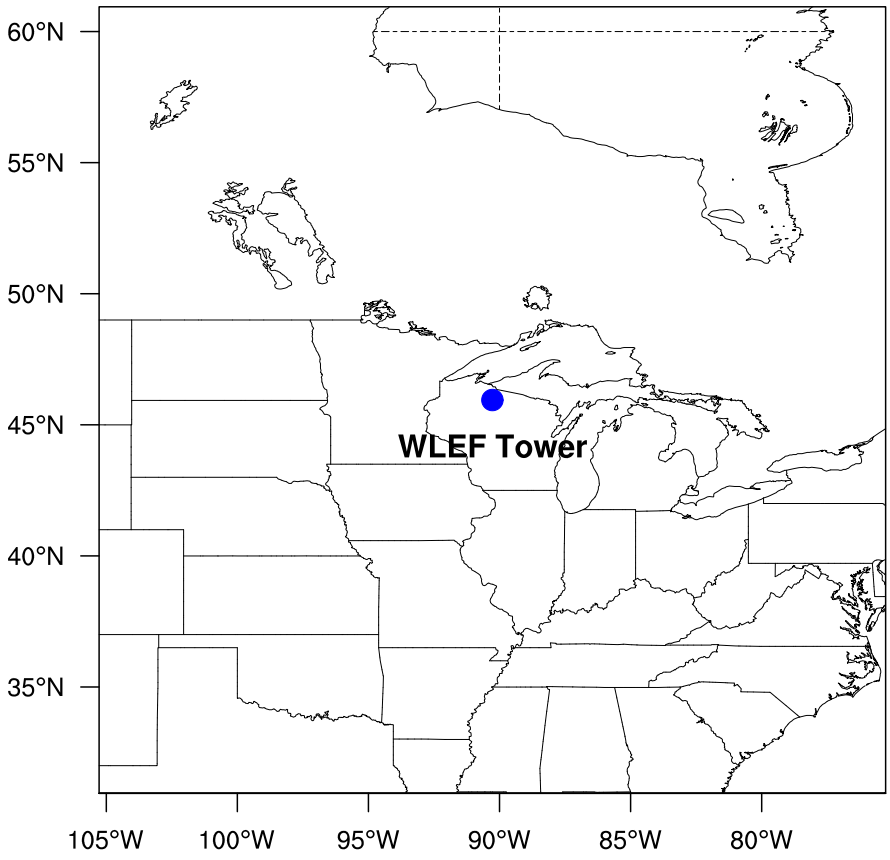

Figure 3.2: Location of the WLEF television broadcast tower.

frequency observations of sonic virtual temperature, specific humidity, CO_2 mixing ratio, and three dimensional wind velocity. The use of these raw observed variables and computed fluxes at the 30 m, 122 m, and 396 m levels serve as the primary empirical basis for this study.

The micro-meteorological instrumentation located at each of the three tower levels considered in this study includes sonic anemometers, which measure three dimensional wind velocity and sonic virtual temperature with 10 Hz frequency, as well as Li-Cor high frequency infrared gas analyzers which provide 10 Hz measurements of water vapor and CO_2 mixing ratios (Berger et al., 2001). The Li-Cor high frequency infrared gas analyzers are located at the tower base, and sample air through a 0.009 m inner diameter tube which connects the gas analyzer to the observational level. Air is drawn continuously through the tube to ground level (Berger et al., 2001). Transport of sampled air through the tube leads to dissipation of small scale gradients, although the bias incurred through this mechanism should not have appreciable affects at the scales considered in this study. A detailed de-

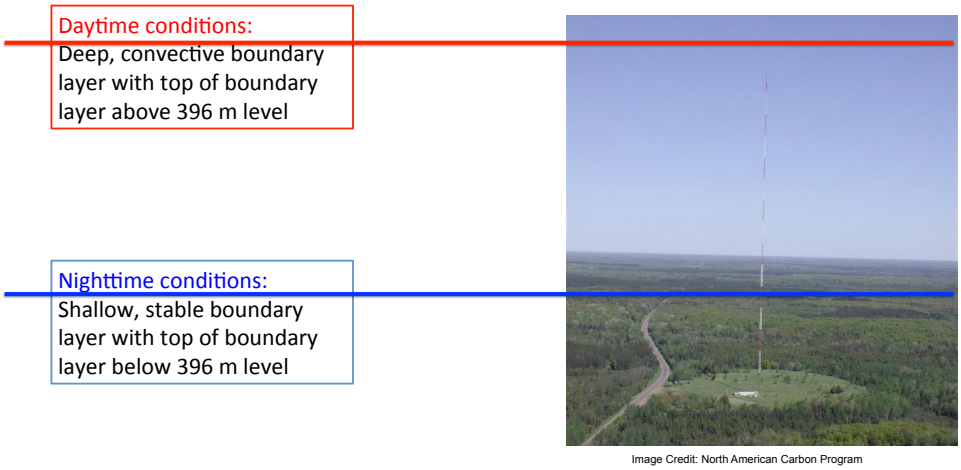

Figure 3.3: A schematic indicating the hypothesized diurnal variation in the position of the top of the boundary layer. This diurnal variation would allow sampling within the convective boundary layer during the daytime and in the lower free troposphere above the stable boundary layer during the nighttime.

scription of the flux computation methodology is give in Berger et al. (2001) and Zhao et al. (1997).

The primary focus of this study is the spatial scale dependence of water vapor variability in the convective mixed layer and nocturnal residual layer. The study relies on diurnal variations in the structure of the planetary boundary layer to make observations of water vapor mixing ratio observed at the 396 m level of the WLEF tower useful for sampling within both the convective mixed layer and the nocturnal residual layer. Figure 3.3 depicts a schematic of the summer time diurnal variation in boundary layer structure. The schematic illustrates the evolution from a stable night time boundary layer during which the 396 m level is largely decoupled from the surface to a deep daytime convective boundary layer during which the 396 m level is enveloped by the vigorous three dimensional turbulent motions of the buoyancy driven convective boundary layer. Therefore, we use observations from the 396 m to probe the water vapor field and observations on other levels to characterize the state of the boundary layer. In a later section we will discuss the mean diurnal cycle of fluxes of latent and sensible heat and of the vertical gradient of CO_2 as a means of identifying when the 396 m tower level is within the convective mixed layer or residual layer.

The WLEF tower offers a long term climatology of observations at 396 m above ground level. The total data set spans over a decade in length, however in this study only data during the summer seasons (June, July, and August) of 2007 through June 2011 are considered. The data are limited to this period for several reasons. First, limiting the analysis to the summer season affords the opportunity to investigate the diurnal variation of the scale dependence of water vapor statistics when the diurnal variation in the dynamics of the boundary layer is large, due to large diurnal variations in insolation. Second, the larger values of water

vapor mixing ratios during the warm season, due largely to the exponential dependence of saturation vapor pressure on temperature and the presence of a non-frozen land surface, ensure that temporal fluctuations in the water vapor field are larger than the instrument sensitivity. The decision to limit the observations to the years ranging from 2007 through 2011 has been made because this range provides a robust estimate of the scale-dependence, while expansion of the range would have incurred unnecessary computational costs and provided little additional physical or statistical insight.

3.2.1 Taylor's Frozen Turbulence Hypothesis

In order to investigate the spatial scale dependence of water vapor from an observed time series, spatial scales must be approximated from observed time scales. Taylor's frozen turbulence hypothesis is commonly used to approximate spatial correlations from temporal correlations and dates back to the work of Taylor (1935). The accuracy of the approximation is dependent on the properties of the particular flow of interest (Pope, 2000). If the approximation holds exactly, then it asserts the exact equivalence between Eulerian space and Eulerian time spectra (Lappe and Davidson, 1963). Numerous studies find support for the application of Taylor's hypothesis across a wide range of time/space scales (e.g. Gifford (1956); Gossard (1960); Lappe and Davidson (1963); Brown and Robinson (1979); L'vov et al. (1999)). Additionally, Taylor's hypothesis has been used in most studies that have investigated the scale dependence of atmospheric variability through aircraft and fixed point observations (e.g. Nastrom and Gage (1985); Gage and Nastrom (1986); Cho et al. (1999a,b, 2000); Wood and Hartmann (2006)).

The frozen turbulence hypothesis posits that a variable $q(t_i)$, observed at discrete times t_i beginning at an initial time t_0, can be assumed to have been observed at spatial points x_i where

$$x_i = x_0 + \bar{U} t_i \tag{3.1}$$

and where x_o is the spatial position at the initial time t_0, and $\bar{U}$ is the mean wind speed. If $x_0 = 0$ then

$$q(x_i) = q\left(\bar{U} t_i\right) \tag{3.2}$$

Therefore, the range of spatial scales that can be computed from a given time series are dependent on the time series temporal length and the mean wind speed $\bar{U}$ during the period of observation.

3.2.2 Planetary Boundary Layer Characterization

The analytical strategy employed in this study depends critically on the existence of data series that can be identified as being observed either totally within the nocturnal residual layer or within the convective mixed layer. Furthermore, in order to maximize the range of scales over which scale dependent variability can be assessed, it is necessary to maximize the length of the data series. In the course of this study, several algorithms were developed

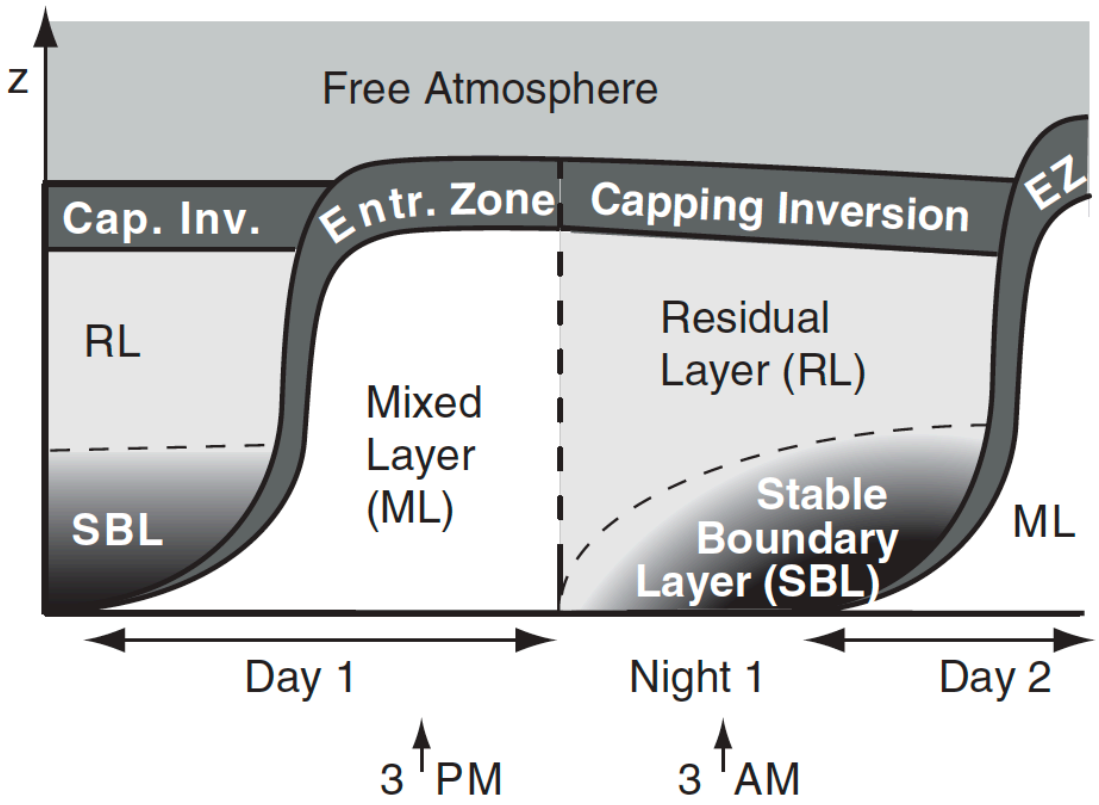

Figure 3.4: A schematic of the diurnal evolution of the planetary boundary layer. The vertical axis (labeled z) is not drawn to scale (Figure is taken without modification from Stull and Ahrens (2000)).

to automatically block segments of the WLEF time series into within and above boundary layer cases. However, it was determined that time sub-setting into nocturnal residual layer and convective boundary layer regimes with fixed starting and end points provided the most direct and easily justifiable method for blocking the data. In order to determine the starting and ending points for sub-setting the data, an objective analysis of the mean diurnal cycle of $[CO_2]$, sensible heat flux H, latent heat flux L, and friction velocity u^* at the 396 m level of the WLEF tower was carried out to identify the mean onset and termination times of the nocturnal residual layer and convective boundary layer regimes. The results of this analysis will be shown later in this section.

Prior to entering into a synopsis of the diurnal variations in the planetary boundary layer observed at the WLEF tower, it is first helpful to review the modern understanding of the diurnal evolution of continental planetary boundary layers. The discussion that is to follow is consistent with descriptions of the diurnal evolution given in Stull (1988) and Garratt (1994). In order to guide this discussion, a schematic of the diurnal evolution of the boundary layer is shown in Figure 3.4. The far left hand side of Figure 3.4 coincides with

sunrise of Day 1, and the dashed vertical line near the center of the figure coincides roughly with sunset of Day 1.

Beginning with sunrise on Day 1, solar radiation warms the land surface which in turn drives sensible heat fluxes from the land to the atmosphere. These sensible heat fluxes drive buoyant production of turbulence that leads to the rapid formation of a mixed layer that grows in depth until it reaches capping inversion (the existence and location of the capping inversions is largely related to the location of prior mixed layers and entrainment zones). At the top of the mixed layer is the entrainment zone, across which air is exchanged between the mixed layer and the overlying atmosphere. Beginning roughly around sunset, with the decrease of incoming solar radiation and the efficiency with which the land surface emits longwave radiation, the sensible heat flux between the land and atmosphere changes direction. This leads to the rapid dissipation of turbulent motions and the formation of a relatively shallow layer of stably stratified air near the ground referred to as the stable boundary layer. Immediately above the stable boundary layer lies the neutrally stratified residual layer that extends up to the capping inversion. The residual layer is largely isolated from the free troposphere and land surface by the capping inversion and the stratification of the stable boundary layer, respectively.

The dynamics of the evolution of the planetary boundary layer at the WLEF site are reported by Yi et al. (2001).

The Research Hypothesis

Prior to analysis of the mean diurnal cycle at the 396 m tower level, it is prudent to visually interpret the characteristics of the diurnal variability evident in the 10 Hz water vapor time series. Doing so allows formation of hypotheses regarding the scaling behavior based solely on visual inspection. Figure 3.5 shows a "typical" diurnal cycle of water vapor at the 396 m level. There are several features to note in the time series shown in Figure 3.5. First, there is a strikingly evident transition in behavior that occurs near sunrise. The nighttime to daytime transition is characterized by a significant increase in variability at small timescales that is consistent with a transition from nearly laminar flow in the nocturnal residual layer to highly turbulent flow within the convective planetary boundary layer. Yi et al. (2001) report a similar transition in other meteorological variables and associate the transition with a decoupling of the nighttime flow at the 396 m level of the WLEF tower during spring and summer from the land surface and nocturnal stable boundary layer. Second, it is evident that, at least for this case, both the daytime and nighttime regimes (with the exception of the water vapor mixing ratio maximum following sunrise) appear to exhibit statistical stationarity, and do not show visually apparent secular trends in the perceived mean or variance.

Insight can be gained into the scale dependence of variability based upon comparison of Figure 3.5 to the idealized synthetic time series shown in Figure 2.1. The results of this comparison are suggested by the annotations in Figure 3.5 that indicate the hypothesized $H > 1/2$ behavior for nighttime conditions and $H < 1/2$ behavior for daytime conditions.

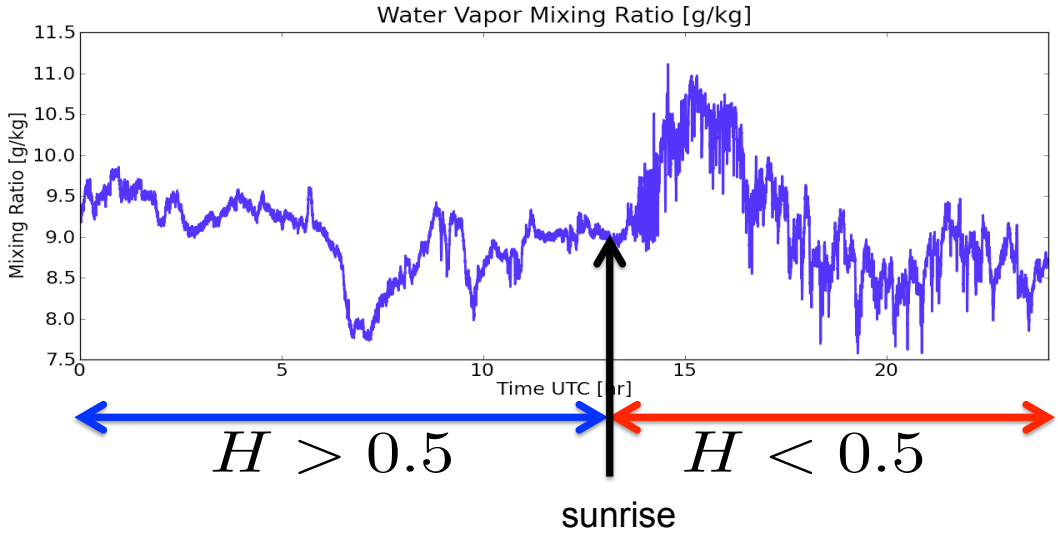

Figure 3.5: An example 10 Hz time series from the WLEF tower time series. The annotations to the time series suggest the basis for the hypothesis for $H > 0.5$ behavior at night and $H < 0.5$ behavior during the day. The basis for this hypothesis is formed by comparison to Figure 2.1.

A similar transition with similar nighttime and daytime behavior is evident in many of the daily time series. Based on these observations, several hypotheses are proposed for which confirmation is sought:

1. Two regimes are present in the WLEF time series. One is representative of the convective boundary layer and a second is representative of the residual layer.

2. The statistical scale invariance of water vapor in the convective boundary layer regime can be characterized by $H < 0.5$ behavior across a wide range of scales.

3. The statistical scale invariance of water vapor in the residual layer can be characterized by $H > 0.5$ behavior across a wide range of scales.

4. The scale invariant behavior of the daytime convective boundary layer regime observed by WLEF largely agrees with the boundary layer regime observed by AIRS.

5. The scale invariant behavior of the nighttime residual layer as observed by WLEF largely agrees with the free tropospheric regime observed by AIRS.

Having established these hypotheses, it is apparent that the last four are critically dependent on the first. The discussion now turns to an analysis of the mean diurnal cycle at the 396 m level of the WLEF tower as a means of supporting the hypothesis that two distinct regimes are present in the WLEF time series.

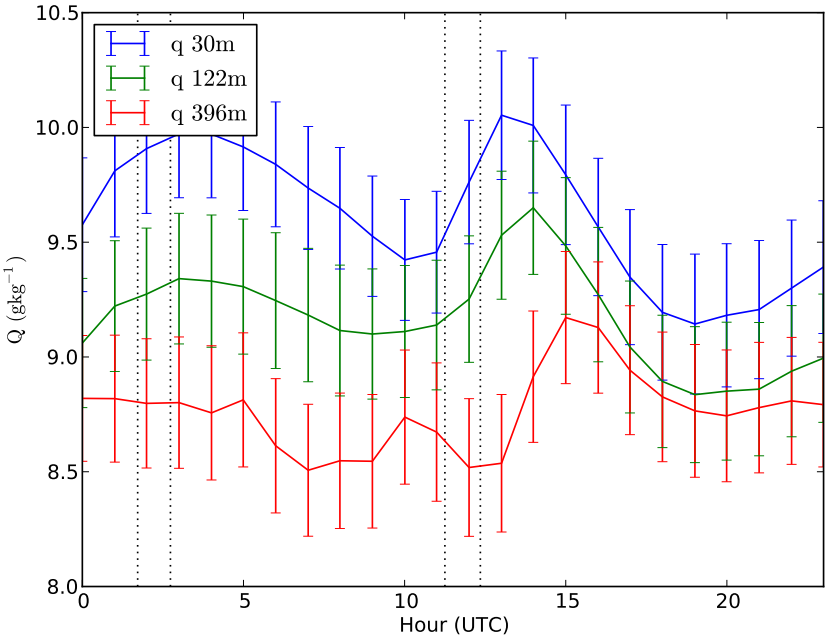

Figure 3.6: The mean diurnal cycle of water vapor mixing ratio measured at the 30 m, 122 m, and 396 m levels of the WLEF tower for the period the June, July, and August months between June 2007 and June 2011. The mean diurnal cycle is computed from hourly means of the time series observed at 10Hz. The vertical error bars are the standard error estimates for the means.

The Mean Diurnal Cycle of Water Vapor

Figure 3.6 shows the mean diurnal cycle of water vapor mixing ratio q as observed at the 396 m, 122 m, and 30 m levels of the WLEF tower. The vertical error bars indicate the standard error of the mean. The vertical dotted lines indicate the range of sunrise ($\approx$ 2h UTC) and sunset times ($\approx$ 12h UTC). The diurnal cycle of q at 396 m is characterized by a relatively small diurnal variation, with a difference between maximum and minimum values of the mean diurnal cycle of less than 0.5 g/kg. The relatively weak diurnal cycle revealed in Figure 3.6 suggests that the weak diurnal variation evident in Figure 3.5 is in fact a fairly robust property of the diurnal cycle of q. The lack of a substantial mean diurnal cycle in water vapor mixing ratio is not surprising given that, in the absence of evaporation or condensation, the mixing ratio is a conserved variable and that, unlike humidity measures such as relative humidity, the mixing ratio does not depend on temperature.

There is some evidence of a minimum in q near sunrise and a relatively broad maximum that occurs throughout daylight hours. In comparison to the other observational levels, the 396 m level tends to be drier than the 30 m and 122 m, levels at night. At 30 m and 122 m,

there is a more pronounced maximum in q closely following sunrise than at 396 m and the maximum occurs later with increasing height. The delay in the early morning maximum that occurs with increasing height is the first empirical evidence of a time dependent evolution of the boundary layer, such that at night the top of the stable boundary layer lies below the 396 m level and during the day the 396 m level lies within the convective boundary layer.

The Mean Diurnal Cycle of Vertical CO_2 Differences

The mean diurnal cycle of CO_2 concentration, here after $[CO_2]$, is shown in Figure 3.7. There is an appreciably larger diurnal cycle of $[CO_2]$ at all levels than is evident for q. The maximum value of $[CO_2]$ occurs just prior to sunrise at 30 m and just after sunrise at the 122m and 396 m levels, with a similar delay in the occurrence of the daily maximum value with height as was seen for q. The minimum value of $[CO_2]$ in the mean diurnal cycle occurs a few hours prior to sunset. The magnitude of the mean diurnal cycle decreases with height. The large diurnal cycle is primarily a result of substantial time dependent surface sources and sinks of $[CO_2]$ associated with photosynthesis (a $[CO_2]$ sink) and aerobic microbial respiration (a $[CO_2]$ source). While the substantial sources and sinks of $[CO_2]$ that lead to the observed diurnal evolution are interesting in their own right, they also provide a means of interpreting the diurnal evolution of the boundary layer and in particular of estimating the position of the top of the planetary boundary layer (Yi et al., 2001).

Figure 3.8 shows the mean diurnal cycle of the difference in CO_2 concentration between the 30 m and 396 m levels. The vertical error bars are the standard errors of the means. The the difference $\Delta[CO_2]$ is given by

$$\Delta[CO_2] = \left[CO_2^{30\mathrm{m}}\right] - \left[CO_2^{396\ \mathrm{m}}\right] \tag{3.3}$$

such that positive values are indicative of larger $[CO_2]$ concentrations at 30m. Understanding the connection between the position of the top of the planetary boundary layer relative to the 396 m tower level and the observed vertical differences in $[CO_2]$ concentration requires understanding the role of the biological processes that are the prominent sources and sinks of $[CO_2]$ as well as transport processes that transport $[CO_2]$ vertically in the atmosphere (Yi et al., 2001). The dominant biological processes that control the vertical gradient of $[CO_2]$ are the consumption of $[CO_2]$ by photosynthesis, which to first order is controlled by the amount of photosynthetically active radiation, and the release of $[CO_2]$ as a byproduct of aerobic respiration by soil microbes, which is largely controlled by the soil temperature. Deep soil temperature remains relatively constant throughout the diurnal cycle, therefore the release of $[CO_2]$ from soils also remains relatively constant. Conversely, due to the substantial diurnal variation in photosynthetically active radiation, the uptake of $[CO_2]$ by plants undergoes a large diurnal variation. The stably stratified boundary layer serves as an impediment to the vertical transport and mixing of $[CO_2]$ at night, thereby allowing a large $[CO_2]$ concentration to build up near the ground level giving rise to large vertical gradients in $[CO_2]$ as is evident in Figure 3.7 and 3.8. During the daytime, turbulent mixing dissipates the vertical gradients in $[CO_2]$ that formed during the night. The uptake of $[CO_2]$ by plants

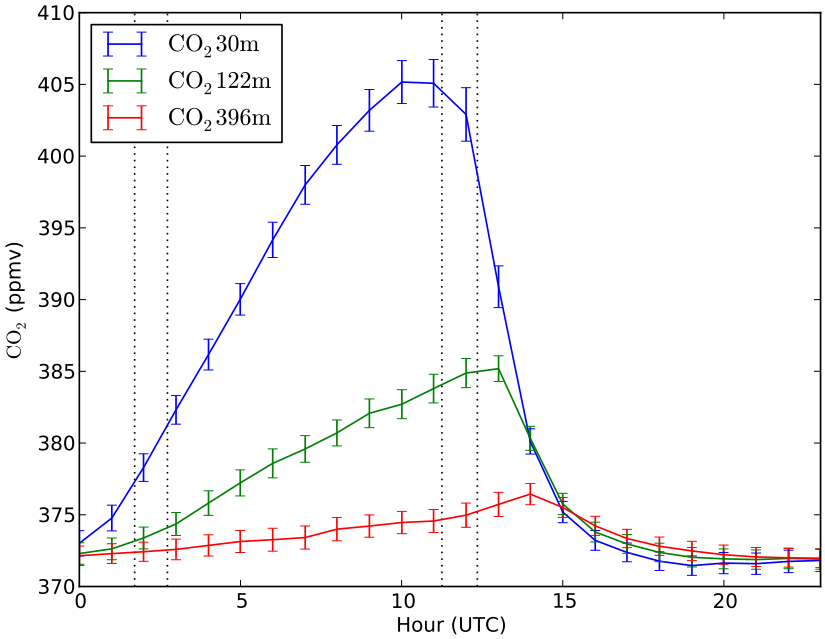

Figure 3.7: The mean diurnal cycle of $[CO_2]$ mixing ratio [ppmv] measured at the 30 m(blue), 122m (green), and 396 m (red) levels of the WLEF tower. The vertical error bars indicate the standard error estimates for the means.The vertical dotted lines indicate the range of sunrise ($\approx$ 2h UTC) and sunset times ($\approx$ 12h UTC)

is sufficiently rapid that by 15h UTC the $[CO_2]$ concentration at 396 m exceeds that at 30 m despite the vigorous mixing associated with the daytime convective boundary layer.

Based on these fluid dynamical and biological processes, Yi et al. (2001) have identified the existence of this diurnal variation in $[CO_2]$ gradients at multiple tower levels as a basis for identifying decoupling between particular tower levels and the surface. Based on the methodology shown in Yi et al. (2001), Figure 3.8 suggests that the 396 m level begins decoupling from the surface beginning just prior to sunset, when the difference in $[CO_2]$ concentration between the 30 m and 396 m levels begins to grow and then begins to recouple with the surface by roughly 15h UTC when the vertical gradient has been largely diminished.

The Mean Diurnal Cycle of u^* at 396 m

The mean diurnal cycle of the friction velocity u^* is shown in Figure 3.9 for the 396 m tower level. The friction velocity u^* is defined as

$$u^* = \left(\overline{u'w'}\right)^{\frac{1}{2}} \tag{3.4}$$

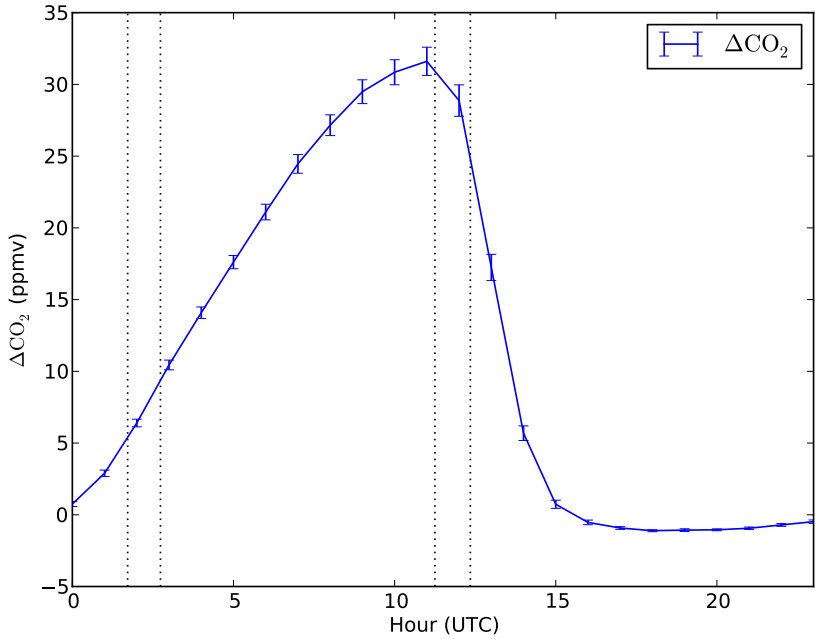

Figure 3.8: The mean diurnal cycle of difference of $[CO_2]$ mixing ratio [ppmv] between the 30 m and 396 m tower levels. Positive values indicate larger $[CO_2]$ concentrations at 30m. The vertical error bars indicate the standard error estimate of the means.The vertical dotted lines indicate the range of sunrise ($\approx$ 2h UTC) and sunset times ($\approx$ 12h UTC)

where u' and w' are the vertical and horizontal fluctuating velocity components. The friction velocity is related to the vertical flux of horizontal momentum and therefore the vertical shear stress (e.g. Holton (2004)). The mean diurnal cycle is characterized by a nearly factor of three increase in u^* between daytime and nighttime conditions that is associated with larger vertical fluxes of momentum associated with the convective mixed layer relative to the more laminar conditions observed at night. The variation in u^* over the daytime portion of the diurnal cycle is larger than the variation over the nighttime portion. This is related to the variability of the turbulence intensity in association with changes in the surface sensible heat fluxes. In comparison to the vertical gradient in CO_2 shown in Figure 3.8, the transition between the daytime and nighttime regimes for u^* begins slightly later. This is likely related to the dependence of the $[CO_2]$ gradient on observations from multiple tower levels rather than from a single level for u^*, and highlights the substantial differences in conditions that can exist between the upper and lower level of the tower. Based upon these observations, the mean diurnal cycle of u^* suggest that the daytime convective mixed layer likely envelopes the 396 m level by 15h UTC and then transitions to the more laminar nighttime residual layer by 4h UTC.

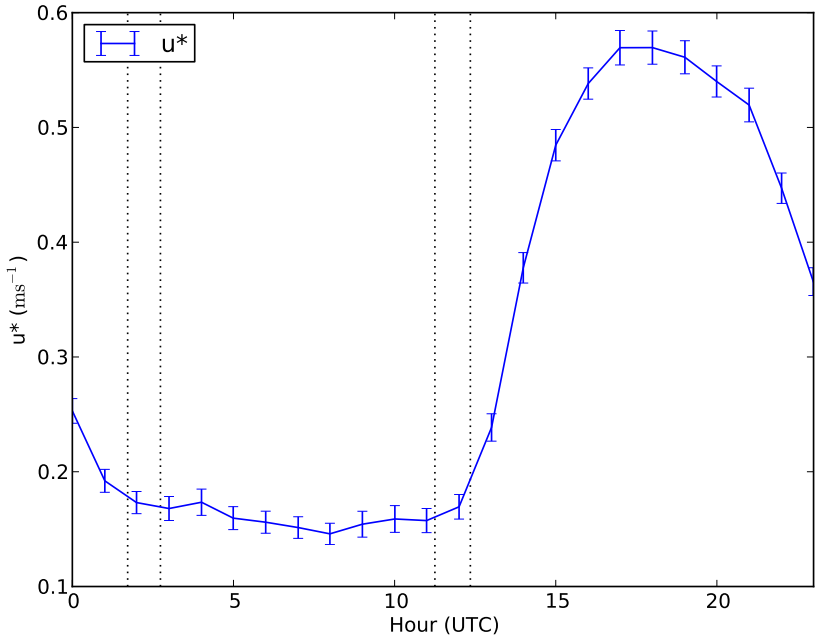

Figure 3.9: The mean diurnal cycle of the friction velocity u^* at the 396 m level of the WLEF tower. The error bars indicate the standard error estimate of the means.The vertical dotted lines indicate the range of sunrise ($\approx$ 2h UTC) and sunset times ($\approx$ 12h UTC)

The Mean Diurnal Cycle of H and L at 396 m

The mean diurnal variation of sensible H and latent L heat fluxes is shown in Figure 3.10. The functional shape of the diurnal cycle of H and L is fairly similar to that seen for u^*, and is characterized by maximum values in the day and minimum values at night. Both H and L exhibit a crossover from the nighttime to daytime regimes that occurs at roughly the same time as was observed for u^*. Perhaps more interesting is the somewhat smaller diurnal range in L and the pronounced flattening of the daytime portion of the diurnal cycle relative to H, both of which are consistent with the perceived stationarity of the 10Hz and mean water vapor series shown in Figure 3.5 and 3.6 respectively. The diurnal cycle evident in H and L shown in Figure 3.10 largely agree with the transition between the convective mixed layer and residual layer suggested by the diurnal cycles of CO_2 and u*.

Selection of Analysis Periods

As previously discussed, this analysis of the mean diurnal cycle in tower observations has been motivated by a need to determine the longest subsets of the diurnal cycle that can be identified as being entirely within either the convective mixed layer or the residual layer.

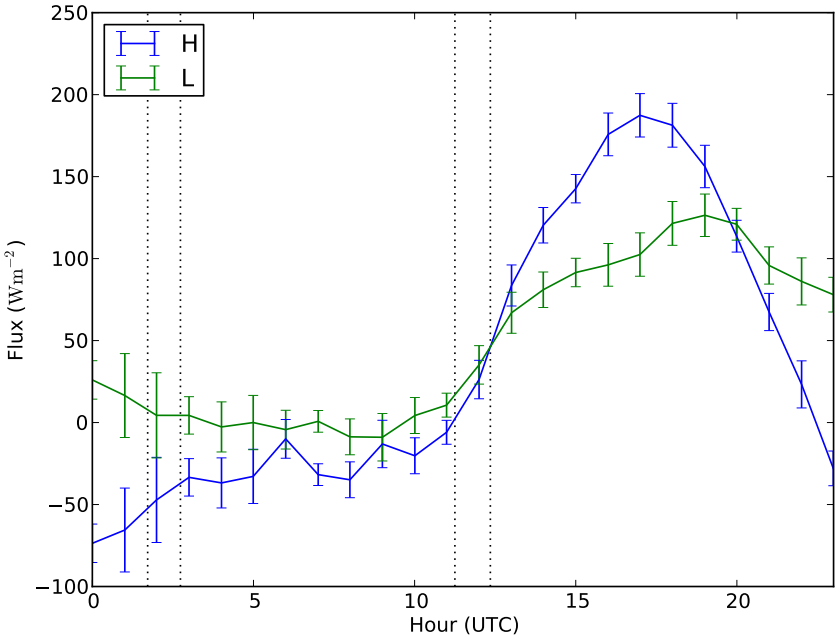

Figure 3.10: The diurnal cycle of latent (L) and sensible (H) heat flux from the 396 m level of the WLEF tower. Black dotted vertical lines indicate the range of sunset ($\approx$ 2h UTC) and sunset ($\approx$ 12h UTC) times for the JJA analysis period.

All of the observed variables indicate that a transition between residual layer and daytime convective mixed layer conditions at the 396 m level occurs near sunrise and that the opposite transition, between daytime and nighttime conditions, occurs just before sunset. In order to most unambiguously represent the two regimes that occur at the 396 m level, subsets of daily time series are selected that are approximately centered on the temporal midpoint of the two regimes. These correspond to midpoint times of 7.5h UTC and 19.5h UTC for the residual layer and convective mixed layer regimes respectively. In order to determine the sensitivity of the results to the length of the analysis, the analysis periods are varied. Table 3.1 gives the starting and ending times of the periods of analysis used in this study.

3.3 Statistical Methodology

Two methods are used in this study to investigate the statistical scale invariance of the water vapor measurements from the WLEF tower. The first method is structure function analysis and is directly comparable to the methods used in Section 2.4. Despite the fact that Figures 3.5 and 3.6 suggest that the nocturnal residual layer and daytime convective mixed layer water vapor fields are relatively statistically stationary, a second method, detrended

length (hours)	night start	night end	day start	day end
3 h	6	9	18	21
5 h	5	10	17	22
7 h	4	11	16	23
9 h	3	12	15	24

Table 3.1: Starting and ending time for analysis periods. The night and day start are the starting times in UTC of the analysis periods for the above nighttime stable boundary layer and daytime within mixed layer periods respectively. The night and day end are the ending times in UTC of the analysis periods for the above nighttime stable boundary layer and within mixed layer periods respectively.

fluctuation analysis, is used in order to remove the effects of statistical non-stationarity from the observed time series. In part, the use of detrended fluctuation analysis is motivated by the obvious non-stationarity of the convective mixed layer portion of the u^* mean time series that are shown in Figure 3.9. The mean time series of u^* is indicative of large variations in the mean turbulent intensity throughout the duration of the convective mixed layer. Both methods provide an estimate of the generalized Hurst exponent $h(q)$. In order to be consistent with the analysis of the AIRS water vapor field given in Chapter 2, the structure function and detrended fluctuation analysis methodologies will be used to estimate $h(q=1)$ based on the scaling of first order statistics. In order to be consistent with the notation in Chapter 2 we will denote $h(q=1)$ as H.

3.3.1 Structure Function Analysis Methodology

Algorithmic Description

A detailed description of structure functions and their numerical computation is given in Section 2.4 of this dissertation. The computation of structure functions from the WLEF time series permits a simpler methodology than does the analysis of AIRS observations. The simpler methodology is permitted by two fundamental differences between the AIRS and WLEF datasets. First, the WLEF time series vary only in a single dimension, hence the question of anisotropy is a moot point. Second, unlike the AIRS dataset in which the data points are distributed on a non-uniform grid, the WLEF data are distributed uniformly in time. This removes the need for binning the spatially non-uniform data in the computation of the structure function. In order to agree with the notation used in the upcoming description of detrended fluctuation analysis, the notation used in the present discussion of the structure function algorithm will diverge from that used in Section 2.4. The structure function algorithm operates on a data series x_k that is N elements in length and for which the distance in time or space between sequential x_k's is constant. The distance between sequential x_k's is denoted ΔX.

1. The value of the q^{th} order generalized structure function $S_q(s)$ at a scale s can then be computed directly by

$$S_q(s) = \frac{1}{N-n} \sum_{i=1}^{N-n} |x_i - x_{i+n}|^q \tag{3.5}$$

   where the scale s is an integer multiple n of the separation between sequential x_k's.

2. Step 1 is then repeated for various n in order to form $S_q(s)$ for a range of scales.

The scaling behavior of the q^{th} order structure function $S_q(s)$ can then be determined by visual inspection of log-log plots of $S_q(r)$, to identify portions that appear to be linear and therefore exhibit scaling (i.e. power law behavior). For a portion of the structure function exhibiting scaling, the power law behavior of $S_q(s)$ can be written mathematically as

$$S_q(s) \propto s^{h(q)} \tag{3.6}$$

where $h(q)$ is the generalized Hurst exponent. Within each portion that exhibits scaling, the scaling exponent can be determined by performing a least squares fit to determine $h(q)$ from

$$\log(S_q(s)) = h(q)\, s + const. \tag{3.7}$$

The Hurst exponent H is equal to the first order generalized Hurst exponent,

$$H = h(1). \tag{3.8}$$

In the remainder of this chapter, H will be referred to as the scaling exponent.

3.3.2 Detrended Fluctuation Analysis Methodology

Detrended fluctuation analysis was originally described by Peng et al. (1994) as a means of assessing statistical scale invariance in statistically non-stationary data series. The methodology relies on the computation of a function that relates the behavior of second order statistics to an arbitrary scale. Detrended fluctuation analysis has been applied to numerous natural systems including the spatial structure of clouds (e.g. Ivanova et al. (2000)), climate records (e.g. Koscielny-Bunde et al. (1998); Ivanova and Ausloos (1999); Talkner and Weber (2000)) and hydrology (e.g. Matsoukas et al. (2000); Li and Zhang (2007)). The detrended fluctuation analysis method was extended to relate the behavior of other orders of statistics to an arbitrary scale by Kantelhardt et al. (2002) with the development of multifractal detrended fluctuation analysis. Applications of multifractal detrended fluctuation analysis to natural systems have included hydrology (e.g. Zhang et al. (2008)), meteorology (e.g. Kavasseri and Nagarajan (2005)), and climate (e.g. Varotsos et al. (2006)). In this study, multifractal detrended fluctuation analysis is used in order to afford comparison to first order structure function scaling exponents.

Algorithmic Description

In this section a description of the multifractal detrended fluctuation analysis (MF-DFA) is given in detail. The notation and discussion of the algorithmic details follows closely to those given in Kantelhardt et al. (2002) and Leung (2010). The algorithm operates on a data series x_k that is N elements in length.

1. The algorithm begins by computing the profile $Y(i)$ of the series x_k

$$Y(i) = \sum_{k=1}^{i} \left[x_k - \langle x \rangle\right], i = 1, ..., N \tag{3.9}$$

   where $\langle x \rangle$ is the arithmetic mean of x_k. Note that $Y(i)$ is also a series of length N.

2. The profile $Y(i)$ is then divided into $N_s \equiv \text{int}(N/s)$ non-overlapping segments of length s. In order to span an entire series $Y(i)$ whose length is not an integer multiple of s the series is also divided starting at the opposite end, such that there are total of $2N_s$ segments of length s.

3. Least squares regression is used to calculate the local trend for each of the $2N_s$ segments of $Y(i)$ of length s. The least squares curve fit for the ν^{th} segment is denoted by $y_\nu(i)$.

4. For each segment ν, $\nu = 1, ..., N_s$ the variance is computed by

$$F^2(s, \nu) = \frac{1}{s} \sum_{i=1}^{s} \left\{Y\left[(\nu - 1)s + i\right] - y_\nu(i)\right\}^2 \tag{3.10}$$

   and for each segment ν, $\nu = N_s + 1, ..., 2N_s$ the variance is computed by

$$F^2(s, \nu) = \frac{1}{s} \sum_{i=1}^{s} \left\{Y\left[N - (\nu - 1)s + i\right] - y_\nu(i)\right\}^2 \tag{3.11}$$

5. Averaging over all $2N_s$ segments of length s yields the value of q^{th} order fluctuation function at scale s as

$$F_q(s) \equiv \left\{\frac{1}{2N_s} \sum_{\nu=1}^{2N_s} \left[F^2(s, \nu)\right]^{\frac{q}{2}}\right\}^{\frac{1}{q}} \tag{3.12}$$

6. Steps 1 to 5 are repeated over a range of scales s in order to form the fluctuation function $F_q(s)$.

The scaling behavior of the fluctuation function $F_q(s)$ can be determined by visual inspection of log-log plots of $F_q(s)$, to identify portions that appear to be linear and therefore exhibit scaling (i.e. power law behavior). For each scaling portion, the power law behavior of $F_q(s)$ can be written mathematically as

$$F_q(s) \propto s^{h(q)+1} \tag{3.13}$$

where $h(q)$ is the generalized Hurst exponent. Within each portion that exhibits scaling the scaling exponent can be determined by performing a least squares fit to determine $h(q)$ from

$$\log\left(F_q(s)\right) = \left(h(q)+1\right)s + const. \tag{3.14}$$

Note, however, that in the case of first order detrended fluctuation analysis the actual scaling exponent is of the fluctuation function F_q is $H+1$. Nonetheless the H will be referred to as the scaling exponent, for consistency with Chapters 2 and 4.

3.3.3 Algorithmic Implementation

The implementation of the structure function and and detrended fluctuation algorithms to analyze the WLEF time series is relatively straight forward, where the only deviations from the direct implementation of the algorithms given in Section 3.3.1 pertain to the removal of erroneous observations from the time series, cloud masking, normalization,and the use of Taylor's Frozen Turbulence Hypothesis to convert temporal scales to spatial scales.

Time series values that are flagged as erroneous are removed from the time series. The presence of cloud at the 396 m level could lead to errors in the water vapor measurements due to wetting of the sampling tube inlet that would likely lead to over estimation of the mixing ratio. The presence of cloud at the 396 m level can be identified by an increase in the number of sonic anemometer measurements flagged as erroneous due to the effects of cloud droplets in the beam path, and the erroneous values are used to mask cloudiness at the 396 m level. The structure function and detrended fluctuation analysis algorithms have been applied to the WLEF 396 m water vapor mixing ratio observations. The algorithms have been applied for the time subsets of each diurnal cycle given in Table 3.1. This yields one structure function and one detrended fluctuation function for each of the nocturnal residual layer and convective mixed layer subsets. This averaging is performed in two steps:

1. Use Taylor's frozen turbulence hypothesis to convert the time scale of structure function and detrended fluctuation function to a length scale using the mean wind speed computed for the period of analysis

    - This is performed for each residual layer and convective mixed layer structure function and detrended fluctuation functions using the mean horizontal wind speed computed for each. As a result, each residual layer and convective mixed layer structure function and detrended fluctuation function is defined over a unique set of discrete scales.

2. The spatial structure functions and detrended fluctuation functions are normalized by their value at the scale closest to 0.5 km.

3. The discrete spatial scales for all functions are then binned into logarithmically spaced bins and the mean of each bin is computed.

The final output of the algorithm is a single mean structure function and a single mean detrended fluctuation function that are functions of length scale for each of the residual layer and mixed layer periods given in Table 3.1. The normalization, described in step 2 of the averaging procedure, ensures that each structure function and detrended fluctuation function is weighted equally in the average. The normalization does not change the slope of the log-log structure function or detrended fluctuation function.

As a result of the variability of the mean horizontal wind speed, not all length scales are sampled with equal frequency. Figure 3.11 shows plots of the number of times each length scale bin is sampled during the June 2007 through June 2011 analysis period, which is labeled in the plot as N_{sf}. The drop off in N_{sf} at the smallest and largest scales occurs because these scales are only sampled on the calmest and windiest days, respectively. Despite the drop off at very large and small scales, it is clear that there is a range of length scales spanning several decades that are sampled by all structure functions.

3.4 Results

The structure function and detrended fluctuation analysis methods that were described in the previous section have been used to analyze the scale dependence of variability in observations of water vapor mixing ratio from the WLEF tower. Two sets of results are shown for both structure function analysis and detrended fluctuation analysis. In the first set of results the structure functions and detrended fluctuation functions are truncated at a scale equal to one quarter of their temporal length prior to spatial binning. In the notation used in Section 3.3.2, this is equivalent to truncation at a scale equal to $N_s/4$. The reason for this truncation is to ensure that at each scale the computed values of the structure functions and detrended fluctuation functions are a sufficiently statistically robust estimate. The second set of results does not employ truncation, and hence the functions are defined over a larger range of scales. While there is some danger in interpreting the results at larger scales which may not be robustly estimated for any given daily structure function, it is likely that much of this danger is ameliorated in the spatial binning and averaging process. In the next part of the results section, the computed structure functions and detrended fluctuation functions are shown alongside the best fitting power law for each, so that qualitative features of the structure functions and detrended fluctuation functions can be considered. Quantitative assessment of the scaling behavior of the structure functions and detrended fluctuation functions is reserved until the end of the section, where it is reported in tabular form.

3.4.1 Results with truncation at $N_s/4$

Figure 3.12 depicts the first order structure functions for the nocturnal residual layer and daytime convective mixed layer in the top and bottom panels respectively. The structure functions for all subset lengths are shown in each plot. In both the nocturnal residual layer and convective mixed layer cases the linearity at scales from 1 km to 100 km is indicative

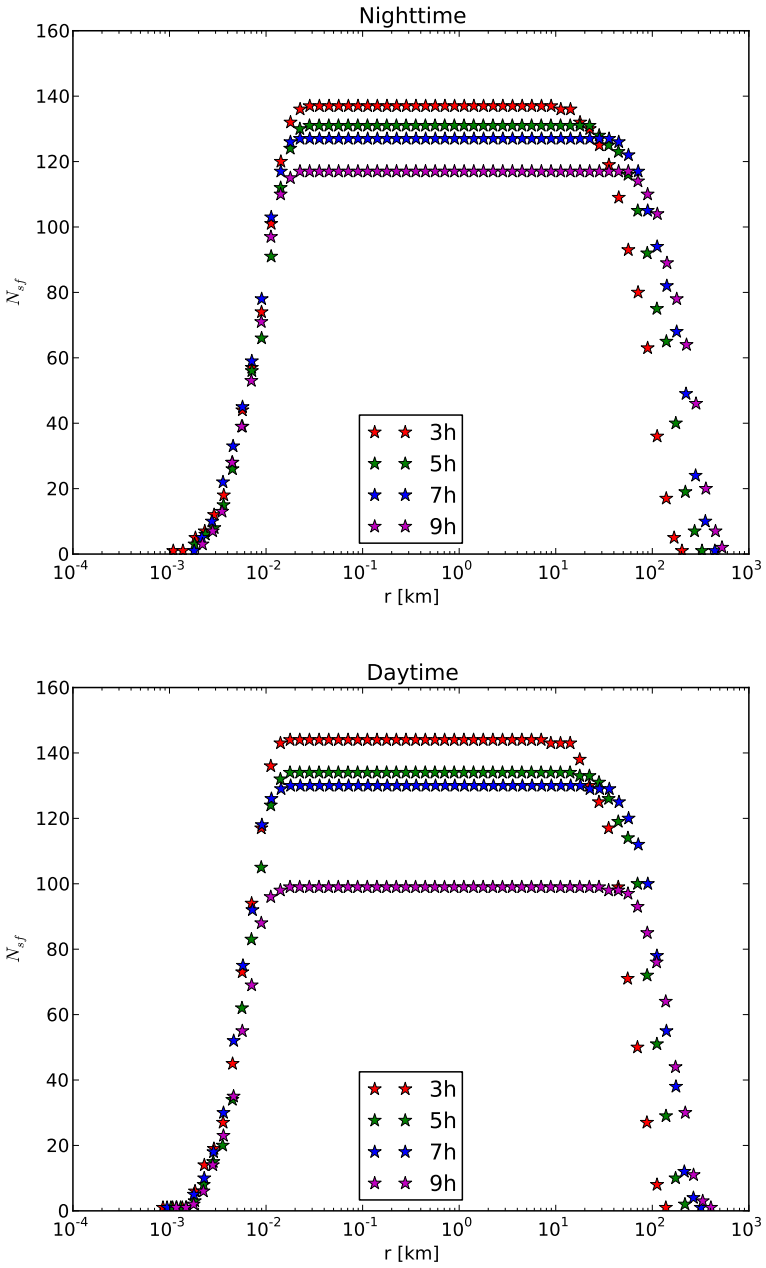

Figure 3.11: The number of daily structure functions and detrended fluctuation functions N_{sf} included in the computation of the mean.

of power law behavior. Linear least squares lines for scales between 1 km and 100 km are plotted for each of the structure functions. The coincidence of the least squares lines suggests that the structure functions exhibit similar power law behavior.

If a structure function S_1 exhibits power law dependence on r with scaling exponent H, then plots of S_1/r^H should appear as constant functions of r. Plots of S_1/r^H, where H is determined by the least squares fits shown in Figure 3.12, are shown in Figure 3.13. The near constant function behavior of S_1/r^H at scales between 1 km and 100 km confirms the power law behavior evident in Figure 3.12. At large scales, there appears to be some divergence from power law behavior, but this is likely due to under sampling at these large scales as suggest by Figure 3.11.

Figure 3.14 depicts the detrended fluctuation functions truncated at $N_s/4$. The general behavior of the detrended fluctuation functions is similar to that seen for the structure functions shown in Figure 3.12, with clear power law scale dependence between 1 km and 100 km and a flattening off at small scales. The flattening at small scales is likely related to the damping of small scales gradients associated with transport through the sampling tube. The range of the detrended fluctuations functions is larger than that of the structure functions, which is expected given Equation 3.13. The least squares power law fits that are shown in Figure 3.14 suggest that the power law behavior is largely independent of the length of the analysis interval.

Plots of F_1/r^{H+1} are shown in Figure 3.15 and should be interpreted similarly to the plots of S_1/r^H shown in Figure 3.13. The constant function of r behavior between 1 km and 100 km again confirms the power law behavior at these scales. The break from power behavior of F_1/r^H at large scales is reduced relative to S_1/r^H.

3.4.2 Results with no truncation

Figure 3.16 shows the convective mixed layer and residual layer structure functions without truncation. Results for the nocturnal residual layer are shown in the top panel of Figure 3.16 and show clear evidence of the presence of power law behavior at scales between 1 km and 100 km. At the largest scales for each subset length, there is some evidence of a flattening of the structure functions, although given the infrequency with which these scales are sampled (e.g. Figure 3.11) and the questionable robustness of structure function estimates at these scales any physical interpretation of the flattening is questionable.

Unlike the untruncated residual layer case which is largely consistent with its truncated counterpart, there are substantial differences evident between the the truncated and untruncated convective mixed layer structure functions. The most prominent difference between the truncated and untruncated convective mixed layer results is that the power law behavior is less distinct in the non-truncated case. This deviation from power law behavior is best observed by noting the larger variation in the structure functions about their best fit lines.

Figure 3.17 depicts plots of S_1/r^H as were shown in Figure 3.13 for the truncated structure functions. The plots shown in Figure 3.17 largely confirm the existence of power law behavior

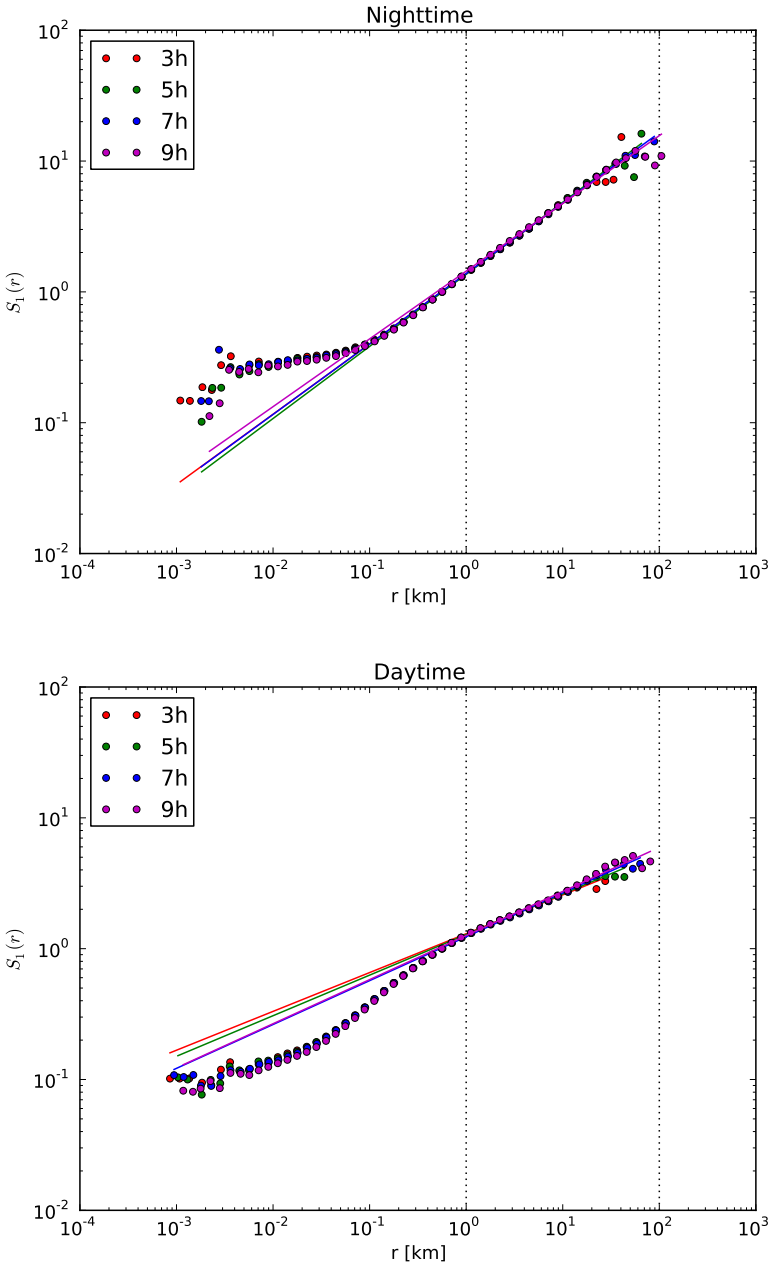

Figure 3.12: Plots of the first order structure functions $S_1(r)$ truncated at $N_s/4$ for nocturnal residual layer (top) and daytime convective mixed layer (bottom) regimes. The best fitting power laws are shown as solid lines. Vertical dotted lines indicate the least squares fitting region.

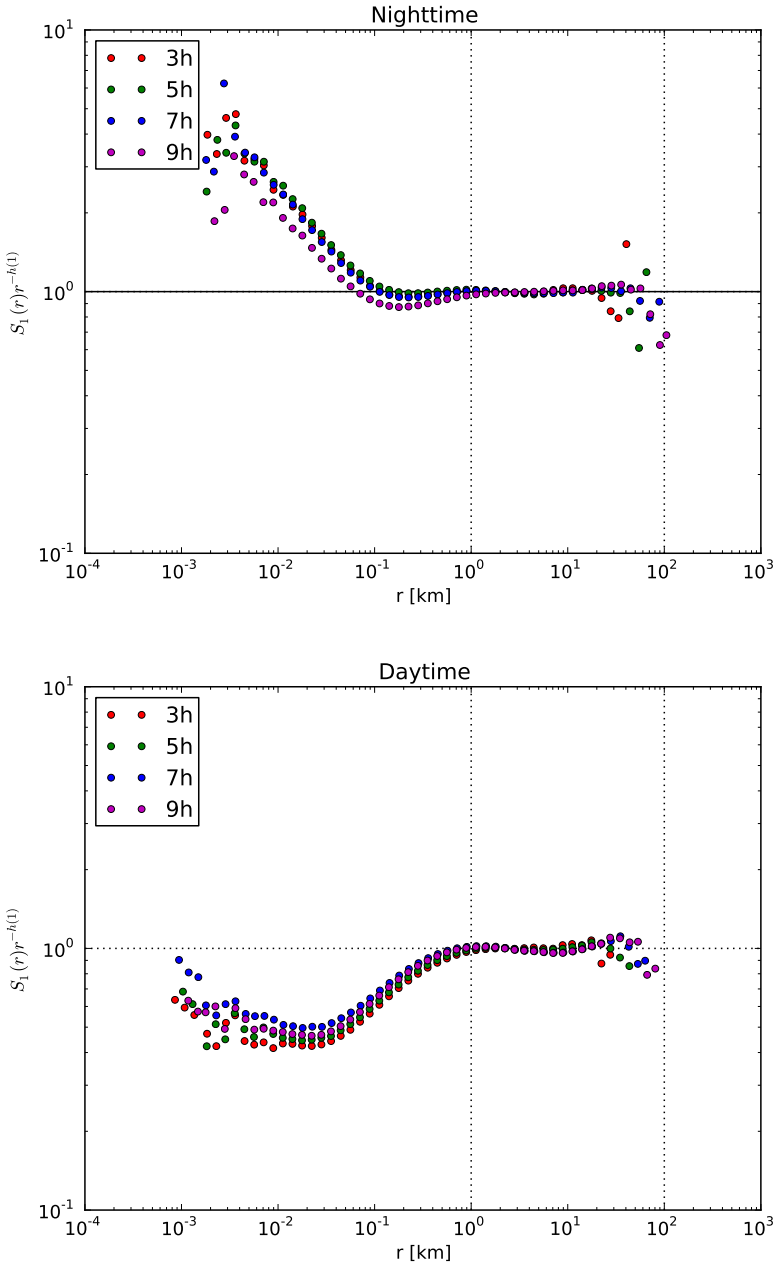

Figure 3.13: Plots of the normalized first order structure function $S_1(r)/r^H$ truncated at $N_s/4$ for nocturnal residual layer (top) and daytime convective mixed layer (bottom) regimes. Each curve has been normalized by its value at r = 10km. Vertical dotted lines indicate the least squares fitting region and the horizontal dotted line is a reference line that indicates perfect scaling.

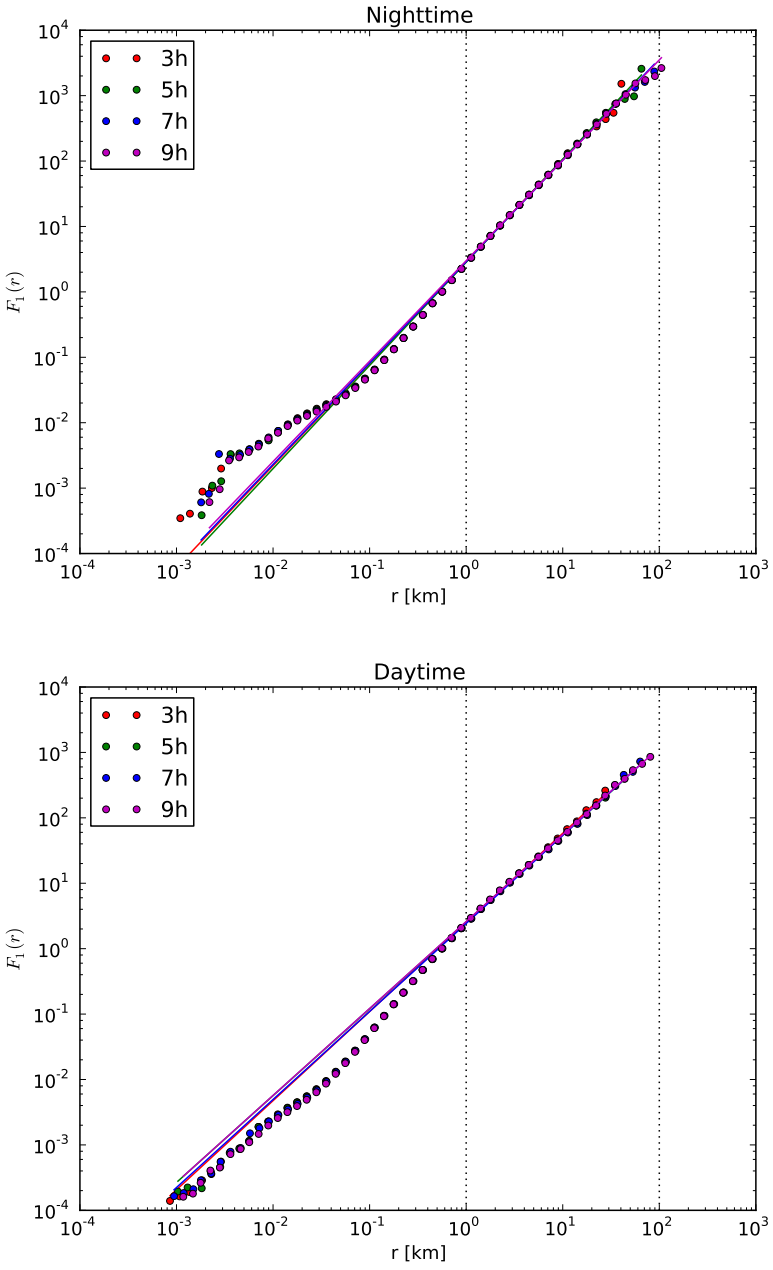

Figure 3.14: Plots of the detrended fluctuation functions $F_1(r)$ truncated at $N_s/4$ for nocturnal residual layer daytime (top) and convective mixed layer (bottom) regimes. The best fitting power laws are shown as solid lines. Dotted vertical lines indicate the least squares fitting region.

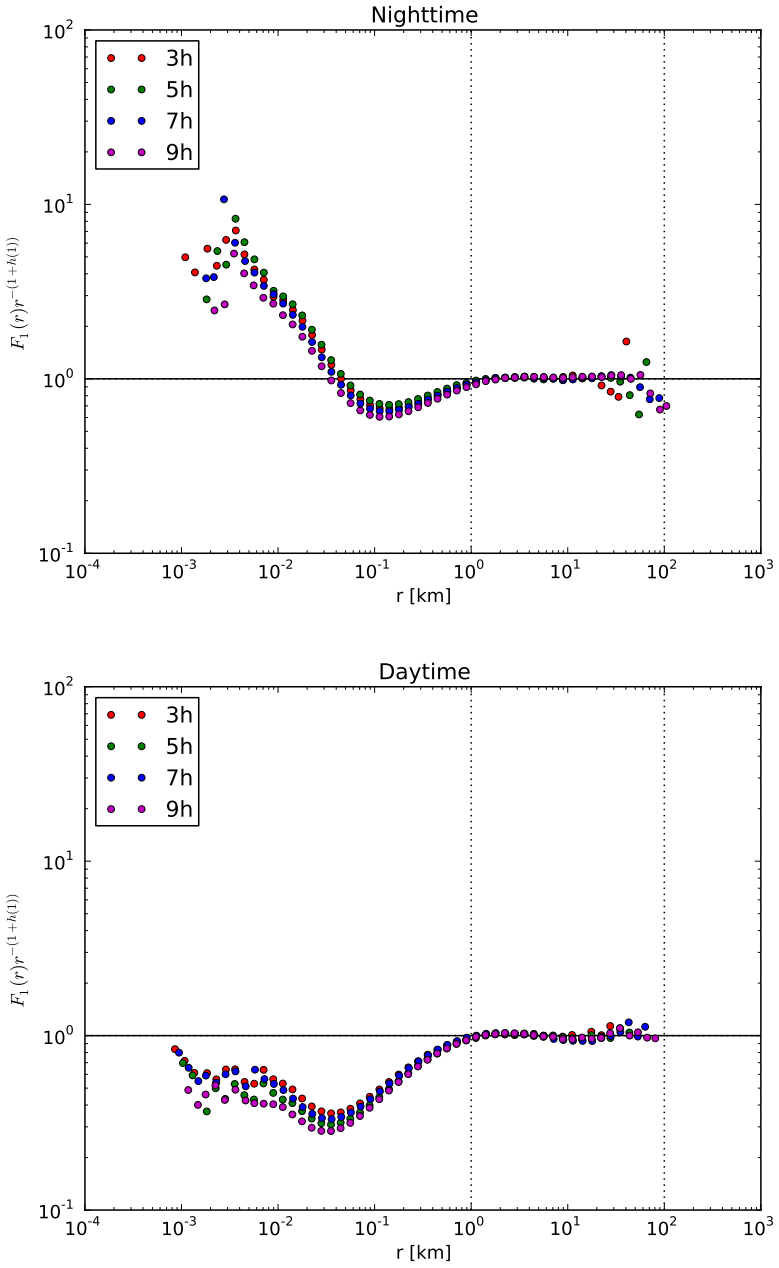

Figure 3.15: Plots of the normalized detrended fluctuation functions $F_1(r)/r^{H+1}$ truncated at $N_s/4$ for nocturnal residual layer (top) and daytime convective mixed layer (bottom) regimes. Each curve has been normalized by its value at r = 10 km. Vertical dotted lines indicate the least squares fitting region and the horizontal dotted line is a reference line that indicates perfect scaling.

for the residual layer cases between 1 km and 100 km and the apparent departure from power law behavior for the convective mixed layer cases across the same range of scales.

Figure 3.18 depicts the convective mixed layer and and residual layer detrended fluctuations without truncation. The non-truncated detrended fluctuation function results bear much similarity to the truncated results for both the nocturnal residual layer and convective mixed layer cases. This similarity was not as apparent for the truncated and non-truncated structure functions, and suggests that some portion of the departure from power law behavior evident in the non-truncated structure functions is likely related to non-stationarity that is removed by detrended fluctuation analysis. Plots of F_1/r^{H+1}, as were shown for the truncated fluctuation function in Figure 3.15, are shown in Figure 3.19 for non-truncated structure functions.

3.4.3 Computed Scaling Exponents

Tables 3.2 and 3.3 report the scaling exponent H estimated by structure function analysis and detrended fluctuation analysis for the residual layer and convective boundary layer cases. Also reported in the tables are the 95% confidence interval for the least squares slope parameter. The narrowness of the 95% confidence interval has been proposed as an indicator of the existence of power law behavior, although what what defines sufficient narrowness is ad hoc (e.g. Tuck (2010)). In order to avoid specifying an ad hoc parameter, the numerical values of the confidence interval are given in Tables 3.2 and 3.3 .

The results for the nocturnal residual layer are shown in Table 3.2. In all cases $H > 0.5$, with the range of H for all cases being $0.518 \leq H \leq 0.578$. There is some evidence that H becomes smaller as the length of the temporal subset increases, although this increase is relatively small. The detrended fluctuation analysis estimates for H are in general slightly larger than the structure function estimates, however this difference is again rather small. The 95% confidence intervals are generally more narrow for the detrended fluctuation estimates than for the structure function estimates, indicating that the detrended fluctuation estimates can be more closely fit by a power law relationship. *It is clear that these results offer strong support for the third hypothesis given in Section 3.2.2, that the statistical scale invariance of the water vapor field in the residual layer regime can be characterized by* $H > 0.5$ *across a wide range of scales.*

In the convective mixed layer the range of H for all cases is $0.297 \leq H \leq 0.403$. The 95% confidence intervals indicate that the structure functions and detrended fluctuation functions are well fit by a power law in all cases. There is a larger difference in H between truncated and non-truncated structure functions than for truncated and non-truncated detrended fluctuation functions. This suggests that non-stationarity may be affecting the structure functions in the convective mixed layer, and that greater confidence should be placed in the detrended fluctuation estimate of H than in the structure function. This non-stationarity of the convective mixed layer is not surprising given the larger daytime non-stationarity in other daytime boundary layer properties. In both truncated and non-truncated cases the detrended fluctuation estimates of H are remarkably close to $H = 1/3$, with the non-truncated case lying

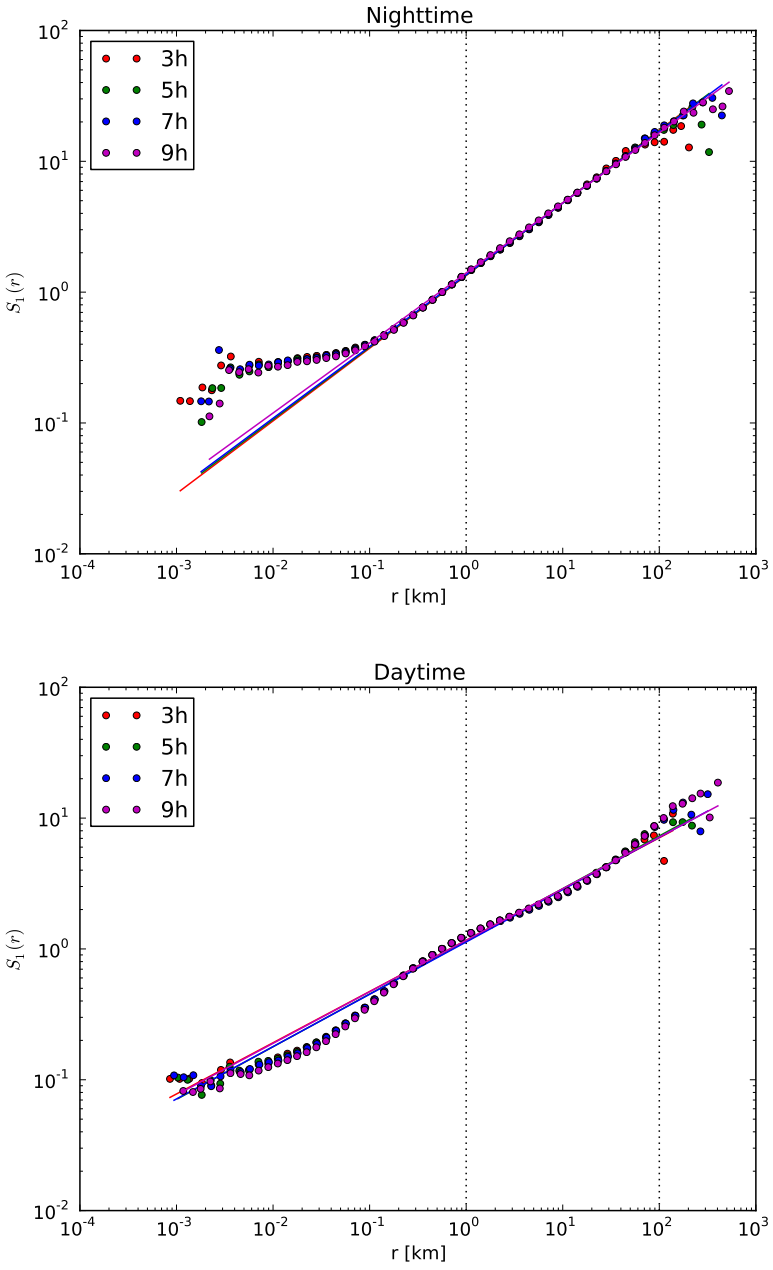

Figure 3.16: Plots of the first order structure functions $S_1(r)$ for nocturnal residual layer (top) and daytime convective mixed layer (bottom) regimes. The best fitting power laws are shown as solid lines. Vertical dotted lines indicate the least squares fitting region.

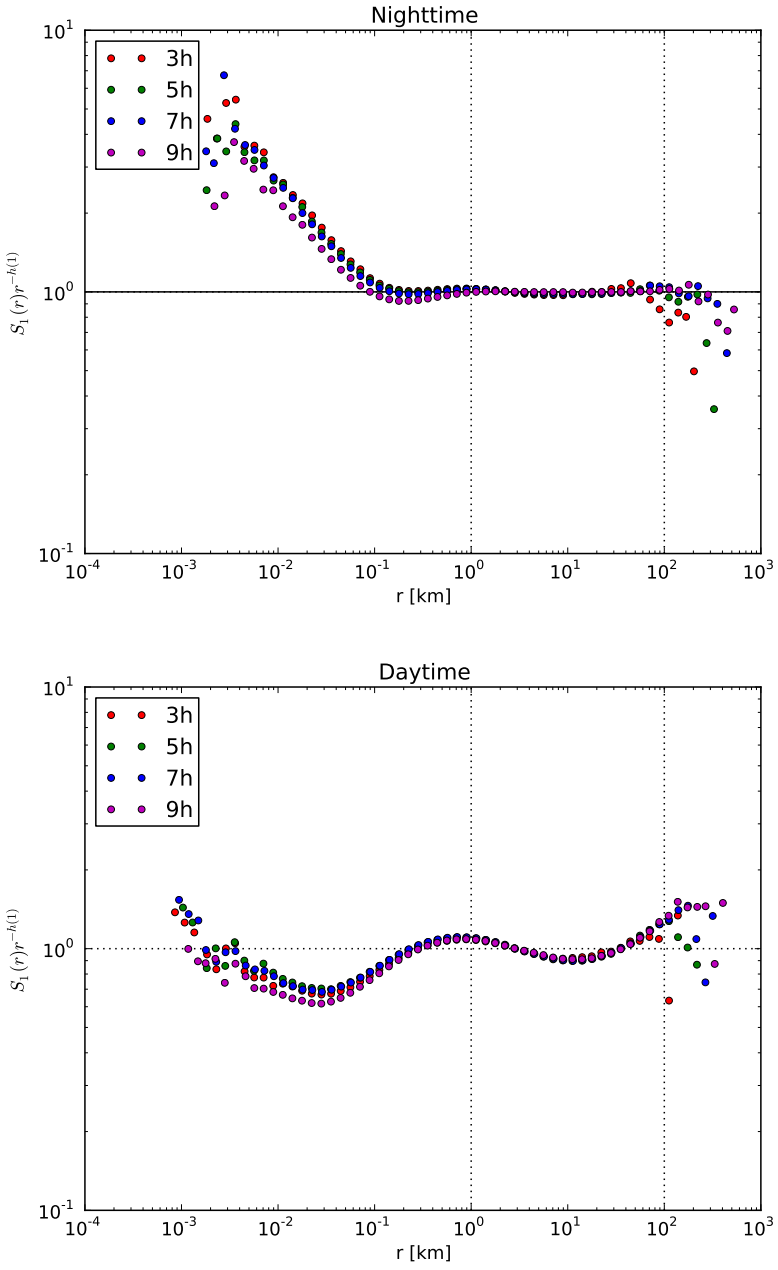

Figure 3.17: Plots of the normalized first order structure function $S_1(r)/r^H$ for nocturnal residual layer (top) and daytime convective mixed layer (bottom) regimes. Each curve has been normalized by its value at r = 10 km. Vertical dotted lines indicate the least squares fitting region and the horizontal dotted line is a reference line that indicates perfect scaling.

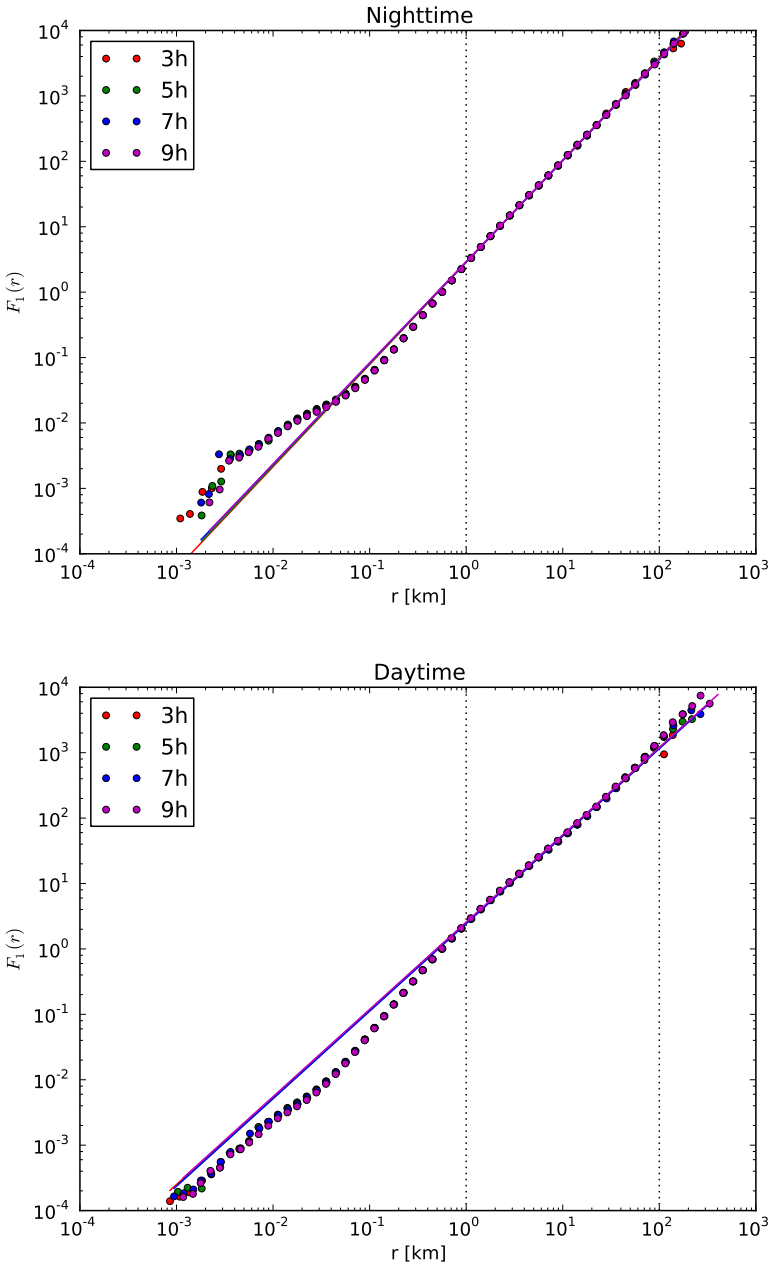

Figure 3.18: Plots of the detrended fluctuation functions $F_1(r)$ for nocturnal residual layer daytime (top) and convective mixed layer (bottom) regimes. The best fitting power laws are shown as solid lines. Dotted vertical lines indicate the least squares fitting region.

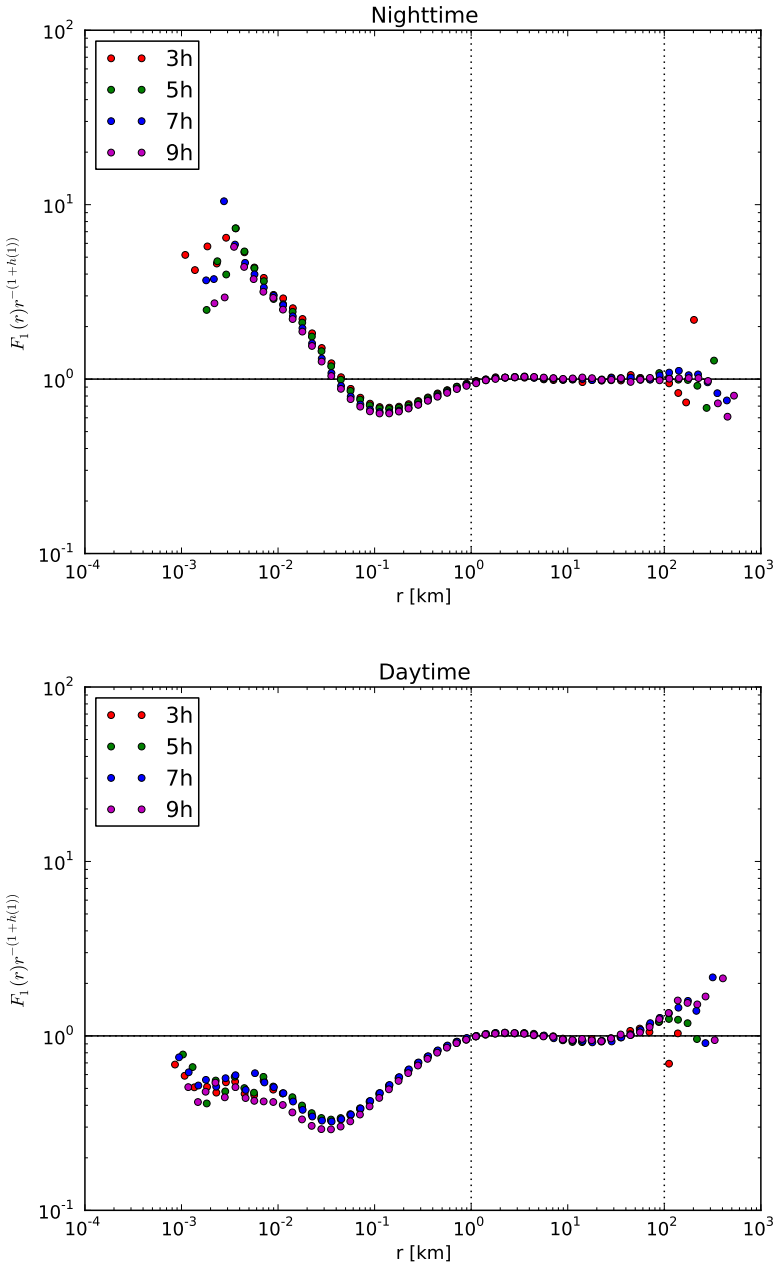

Figure 3.19: Plots of the normalized detrended fluctuation functions $F_1(r)/r^{H+1}$ for nocturnal residual layer (top) and daytime convective mixed layer (bottom) regimes. Each curve has been normalized by its value at $r = 10$ km. Vertical dotted lines indicate the least squares fitting region and the horizontal dotted line is a reference line that indicates perfect scaling.

length (hours)	Night SF $N/4$	Night SF N	Night DFA $N/4$	Night DFA N
3 h	0.537 ± 0.0138	0.556 ± 0.012	0.560 ± 0.012	0.563 ± 0.008
5 h	0.552 ± 0.008	0.552 ± 0.008	0.578 ± 0.009	0.558 ± 0.006
7 h	0.538 ± 0.011	0.548 ± 0.007	0.550 ± 0.0154	0.546 ± 0.007
9 h	0.518 ± 0.021	0.535 ± 0.001	0.535 ± 0.0217	0.548 ± 0.009

Table 3.2: Scaling exponents H and 95% confidence intervals for the residual layer.

length (hours)	Day SF $N/4$	Day SF N	Day DFA $N/4$	Day DFA N
3 h	0.297 ± 0.029	0.392 ± 0.025	0.362 ± 0.013	0.334 ± 0.018
5 h	0.310 ± 0.015	0.403 ± 0.033	0.328 ± 0.018	0.341 ± 0.023
7 h	0.335 ± 0.022	0.400 ± 0.031	0.348 ± 0.025	0.337 ± 0.024
9 h	0.337 ± 0.027	0.394 ± 0.029	0.329 ± 0.022	0.334 ± 0.018

Table 3.3: Scaling exponents H and 95% confidence intervals for the convective mixed layer.

closest to that value. *It is clear that these results offer strong support for the second hypothesis given in Section 3.2.2, that the statistical scale invariance of the water vapor field in the convective mixed layer can be characterized by* $H < 0.5$ *across a wide range of scales.*

Prior to comparing the results of the analysis of the WLEF time series to the results for the analysis of the AIRS water vapor field given in Chapter 2, it is important to distinguish between the range of scales over which the two analyses were performed. The range of scales considered in the WLEF analysis, described in this chapter, extends from 1 km to 100 km. The range of scales considered in the AIRS analysis, describe in Chapter 2, extends from 50 km to 500 km. Therefore, the scaling exponents H computed between the two studies are not a direct comparison, however agreement in the scaling exponents between the two studies is a strong argument that a single scaling exponent characterizes the scale invaraince of atmospheric water vapor structure functions and spectra over the full range of scales from 1 km to 500 km.

In Table 3.4 the results from the AIRS analysis are reproduced alongside the non-truncated detrended fluctuation analysis results for the nine hour subset length. The results for the WLEF analysis shown in Table 3.4 have been limited to non-truncated detrended fluctuation analysis results for the nine hour subset length, because this case allows the largest range of scales to be investigated and by use of detrended fluctuation analysis is less affected by potential non-stationarity. The agreement between the estimates of H from the AIRS and WLEF analysis is extraordinary, especially given the substantial differences in the observational techniques used in obtaining the two data sets.

Perhaps the most surprising aspect of the results shown in Table 3.4 is the agreement between the AIRS free tropospheric and WLEF residual layer estimates of H. This is particularly the case given that the AIRS free tropospheric estimate is computed from AIRS retrievals at the 500 hPa level, which is without question representative of the free tropo-

Regime	AIRS JJA ASC	AIRS DJF ASC	WLEF
FT (RL)	0.548 ± 0.002	0.556 ± 0.002	0.548 ± 0.009
BL (ML)	0.334 ± 0.002	0.335 ± 0.002	0.334 ± 0.018

Table 3.4: Comparison of AIRS Descending pass estimates of H with WLEF estimates of H. For the AIRS analysis H is determined over scales ranging from 50 km to 500 km. For the WLEF analysis H is determined over scales ranging from 1km to 100 km. Only the AIRS results for the ascending cases are reported here, however the full set of AIRS results in given in Table 2.1

sphere, while the WLEF residual layer case is representative of observations made at a height that without question (and in fact by definition) undergoes substantial variations on a diurnal time scale. Hence, the dynamical processes operating between the two cases would be expected to be substantially different yet they are nonetheless characterized by very similar scaling exponents. Without further observations of the residual layer and free troposphere it is difficult to surmise why there should be such agreement. Perhaps the strongest similarity between the free troposphere and residual layer is that in both cases the flow field is largely two dimensional. The two dimensionality of the flow makes it tempting to suggest that chaotic advection, as discussed in Chapter 2, is responsible for the filamentation of the water vapor field in both the residual layer and free troposphere, although there is no way to determine the validity of this hypothesis from this study. Recently, height resolved estimates of scaling exponents have been reported by Fischer et al. (2012) based on airborne lidar observations that are consistent with the boundary layer and free tropospheric scaling exponents seen in the AIRS study. Observations from this platform may prove particularly useful in providing a deeper understanding of the striking similarity between residual layer and free tropospheric scaling exponents.

There is also striking agreement agreement between the AIRS boundary layer and WLEF convective mixed layer scaling exponents. This result provides strong evidence of $H \approx 1/3$ scaling between 1 km and 500 km, and is in general agreement with the findings of Cho et al. (1999a),Wood and Taylor (2001), Comstock et al. (2005), Kahn et al. (2011), and Fischer et al. (2012). What sets the results reported here apart from these prior studies, is the size of the data set that has been analyzed, the efforts that have been to made reduce errors in the analysis methodology, and the estimated error bars on the quantitative estimates of H. Together these three properties allow strong statements to be made regarding the universality of $H \approx 1/3$ as characterizing the spatial scale dependence of first order statistical variability in the boundary layer at scale up to 500km.

3.5 Summary and Conclusions

This work has shown that the first order structure function and detrended fluctuation function of the water vapor field exhibit approximate power law behavior at scales between 1 km and 100 km within the convective mixed layer and nocturnal residual layer. Detrended fluctuation functions are shown to more closely follow a power law relationship than structure functions, although only slightly. It is shown that the Hurst exponent H, determined using least squares, for the residual layer is estimated to be $H = 0.548 \pm 0.009$ and is estimated for the convective mixed layer to be $H = 0.334 \pm 0.018$. The estimate of H for the residual layer is shown to be in very close agreement with the estimates of H for the free troposphere from the AIRS analysis. Similarly, the estimate of H for the convective mixed layer is shown to be in very close agreement with the estimate of H for the maritime boundary layer from AIRS. The difficulty of interpreting the similarity between the AIRS free tropospheric and WLEF residual layer result is discussed and two plausible interpretations are conjectured. Finally, the near equality of H for the AIRS boundary layer regime with H for the WLEF convective mixed layer, when interpreted in the context of previous results offers strong support for the universality of $H \approx 1/3$ in the convectively mixed boundary layer.

The results underscore the need for more thorough exploration of the vertically resolved scale dependence of the lower troposphere and in particular of the nocturnal residual layer. Vertically resolved observations of the free troposphere and residual layer are becoming more practical as has been shown by Fischer et al. (2012) using airborne lidar. Numerical studies may also prove fruitful, although simulations with domains of sufficient extent to support water vapor fluctuations with horizontal scales of 500 km but with sufficient resolution to resolve the complicated dynamics of the stable boundary layer are unlikely to be realized in the near future.

Chapter 4

Structure Function Analysis of Water Vapor in High Resolution Global Climate Model Simulations

Up to this point, the subject matter of this dissertation has focused on the scale dependence of variability in the observed water vapor field, either observed remotely by AIRS (Chapter 2) or in situ by the micrometeorological instrumentation on the WLEF tower (Chapter 3). More specifically, this dissertation has focused on the statistical scale invariance of the observed water vapor variability. However, this work as a whole is primarily motivated by the application of scale dependent statistics and scale invariant statistics to the assessment of and development of climate models. It is in order to return to this foundation that the discussion now turns to the scale dependence of water vapor statistics in climate simulations. As discussed in Chapter 1, one potential application of this research is the estimation of subgridscale moments of the water vapor field as a basis for cloud parameterization (e.g. Cusack et al. (1999)). This modeling paradigm necessarily requires that the grid scale water vapor field exhibits accurate scale dependent variability. In this chapter the scale dependence of water vapor variability in numerical simulations from a GCM will be investigated, and the results will be compared to the analysis of the AIRS water vapor field given in Chapter 2.

4.1 Introduction

The power law behavior of structure functions of the AIRS observed water vapor field is shown in Chapter 2 and the power law behavior of structure functions and detrended fluctuation functions of the water vapor field observed from the WLEF tower are shown in Chapter 3. In both cases the results provide evidence that the scaling exponents H tend to cluster around two values. The first, $H \approx 0.55$, suggests the importance of long range correlations in the free tropospheric and boundary layer residual layer fields. The second value, $H \approx 0.33$, suggests antipersistence of water vapor spatial increments within the convectively mixed

boundary layer. It is therefore only natural to ask if numerical models of the atmosphere produce water vapor fields that exhibit power law behavior and moreover, if the power law scaling exponents cluster around the aforementioned observed values.

In this chapter, a straightforward methodology is described that allows computation of structure functions from global climate model output. The methodology is applied to compute structure functions from global water vapor fields produced by numerical integration of the Community Atmospheric Model Version 4 (CAM4) run in aqua-planet mode. This work seeks to address the following science questions:

1. Do numerical simulations of the atmospheric water vapor field have structure functions that exhibit power law behavior?

2. If the numerical simulations exhibit water vapor structure functions with power law behavior, are the computed exponents a function of the simulation's grid resolution?

3. If the numerical simulations exhibit water vapor structure functions with power law behavior, do the computed exponents agree with those from observations?

4. What are the implications of the observed and simulated structure functions for the problem of parameterization of sub-gridscale process in numerical models?

The lay-out of this chapter is as follows: In the second section, the choice of aqua-planet simulations as the modeling experiment is discussed and the model setup is described. Additionally, the structure function methodology is described. In the third section, the results of the analysis are reported and discussed in the context of the prior empirical results. In the fourth section, extensions of the results to the assessment of the fidelity of the numerically simulated water vapor field to observed reality are discussed as well as the implications for the parameterization of sub-gridscale processes in GCMs.

4.2 Methodology

4.2.1 The Use of Aqua-Planet Simulations

Scientific models are by definition a simplification of physical reality (e.g. Held (2005)). Often the level of simplification is determined out of a combination of necessity (i.e. when underlying physical processes are poorly understood), expediency (i.e. when full representation is too expensive), or simplicity (i.e. when the level of simplification affords more direct or coherent intuition about physical reality). In this study, results from numerical aqua-planet experiments are used to investigate the water vapor field because of the simplicity in interpretation they afford.

Recently, aqua-planet simulations have come into wide use in interpreting properties of numerical simulations of the climate system (e.g. Neale and Hoskins (2000a,b),Williamson (2008), Mapes et al. (2008),O'Gorman and Schneider (2009), and Li et al. (2011)). In a

sense, an aqua-planet simulation is a simplified model of the fully coupled atmosphere-ocean general circulation models (AOGCM) that are designed to represent the climate system as realistically as possible and are used routinely in climate prediction. The simplifications to a state of the art AOGCM that yield an aqua-planet simulation, as is used in this study, involve modification to the atmospheric lower boundary conditions and radiative forcing. The lower boundary condition is simplified by specifying that the whole of the Earth's surface is covered by a single ocean with a fixed temperature distribution that varies only in the meridional direction and is symmetric about the equator (Neale and Hoskins, 2000a). Additionally, the shortwave radiative forcing is specified such that there is a realistic diurnal cycle but no seasonal cycle (Neale and Hoskins, 2000a). Since our focus is on the scale dependence of the modeled processes rather than the boundary conditions, we have used the aqua-planet simulations for all the simulations discussed in this chapter.

The aqua-planet simplifications are designed to produce simulations with axial symmetry (symmetry for purely zonal translations) of statistical moments computed in the limit of long time, as well as symmetry about the equator. Additionally, the aqua-planet simplifications allow the convergence of the simulation with respect to spatial resolution to be studied (e.g. Li et al. (2011); Williamson (2008)) independent of the sensitivity of the simulations to increasingly resolved topography. The effects of changes in the resolution of topography have been shown to impact the atmospheric flow across a wide range of scales (e.g. Ghan et al. (2002)).

In particular, the use of an aqua-planet simulation experiment in this study has two primary advantages. First, the axial symmetry of the aqua-planet simulation is used to simplify the computation of structure functions computed from zonally oriented increments. Second, the lack of topography simplifies the interpretation of the sensitivity of the computed structure functions to computational grid resolution.

4.2.2 Aqua-planet Simulation Details

The aqua planet simulations are performed using the Community Atmospheric Model Version 4 (CAM4) (Neale et al., 2010) as part of the Department of Energy funded project on robust regional climate modeling. In particular, the simulations use the Eulerian dynamical core implemented in CAM4 that is based on a spectral transform method in the horizontal and finite-difference approximations for time advancement and vertical derivatives. A complete description of the CAM4 Eulerian dynamical core is given in Neale et al. (2010).

Simulations at two resolutions are used in this study, with spectral truncations of T85 and T340 that correspond to 2.8° and 0.35° latitude-longitude grids, respectively. The lower boundary condition is provided by the fixed sea-surface temperature that is specified according to the 'control experiment' configuration given in Neale and Hoskins (2000a). The same CAM4 physics routines (Neale et al., 2010) are used at both resolutions in accordance with the equivalent resolution methodology (Williamson, 2008).

Figure 4.1 shows color filled contour plots of the logarithm of the instantaneous specific humidity field at approximately 500 hPa from the CAM4 aqua planet simulations. Figure

4.1 is comparable to Figure 2.11 that shows the AIRS observed instantaneous water vapor mass mixing at 500 hPa. Qualitatively, the structures in the 500 hPa aqua planet specific humidity field and the AIRS observed field are quite similar, particularly for the T340 aqua-planet simulation. The differences between the T340 and T85 water vapor fields will be discussed in greater detail in the context of the structure function results in Section 4.3.

4.2.3 Structure Function Methodology

The computation of structure functions from the CAM4 aqua-planet simulation data is relatively straightforward if the structure functions are only computed from increments in the zonal direction. For any given latitude, the zonal computational grid spacing is uniform. Therefore, letting the scale s be an integer multiple (i.e. $s = n\Delta X$) of the grid spacing ΔX allows the k^{th} order structure function at a particular height, latitude, and scale s to be computed directly by

$$S_k(s) = \frac{1}{N-n} \sum_{i=1}^{N-n} |x_i - x_{i+n}|^q \tag{4.1}$$

where N is the number of zonal grid points in the computational grid. This algorithm makes use of the zonal symmetry of the aqua-planet configuration such that for each latitude and height a single structure function can be computed from all N grid points in the zonal direction.

The computational grid is globally uniform and Cartesian in latitude and longitude. However, due to the sphericity of the earth the horizontal computational grid is not uniform in physical space. The zonal grid spacing varies as a function of latitude from its maximum value at the equator to its minimum value near the poles. The zonal grid spacing defines the set of numerical values taken by the scale s. Therefore, for a given range of scales, a structure function $S_k(s)$ computed at a latitude closer to the equator will be defined at the same or fewer number of scales than a structure function at a latitude located further from the equator. In order to afford comparison to the structure function analysis of the AIRS observed water vapor field, the structure functions are computed for $s < 500$km. Figure 4.2 shows the meridional dependence of the zonal grid spacing ΔX and the meridional dependence of the number of $s < 500$km for the T85 and T340 simulations.

Unlike the AIRS structure function methodology that computes a single structure function from spatial increments accumulated over a three month analysis period, the methodology employed in this analysis computes the first order structure function for each instantaneous water vapor field from zonal increments at each latitude and height. For each instantaneous water vapor field, least squares regression is used to determine the power law scaling exponent for scales below 500 km for each latitude and height. The computed scaling exponents are stored and used to compute the mean power law scaling exponent for each latitude and height. The analysis is performed for two model years of instantaneous water vapor fields that are output at six hour intervals. The two year period of analysis commences after the model has been fully spun-up.

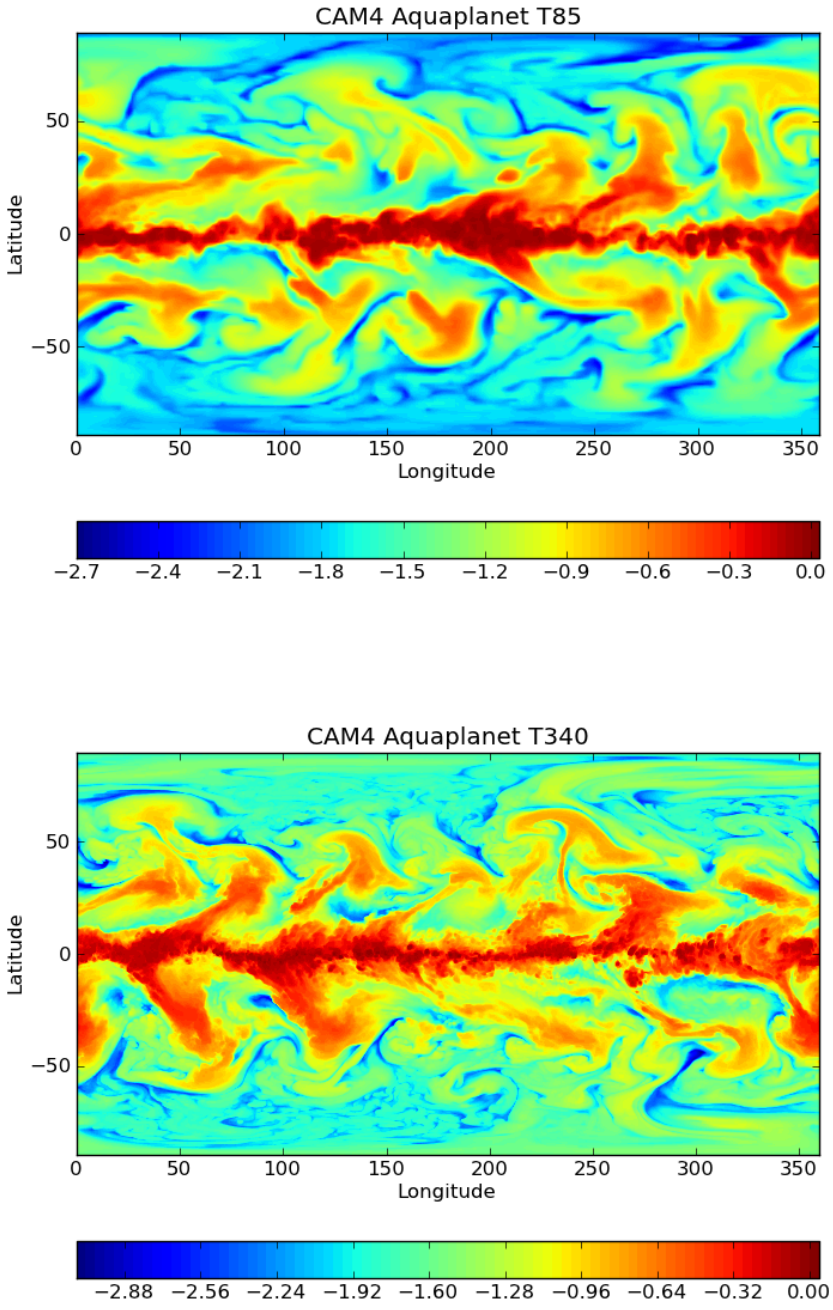

Figure 4.1: Plots of log(q) of the water vapor mixing ratio at 500 hPa from CAM4 aqua planet simulations at T85 (top) and T340 (bottom) resolutions.

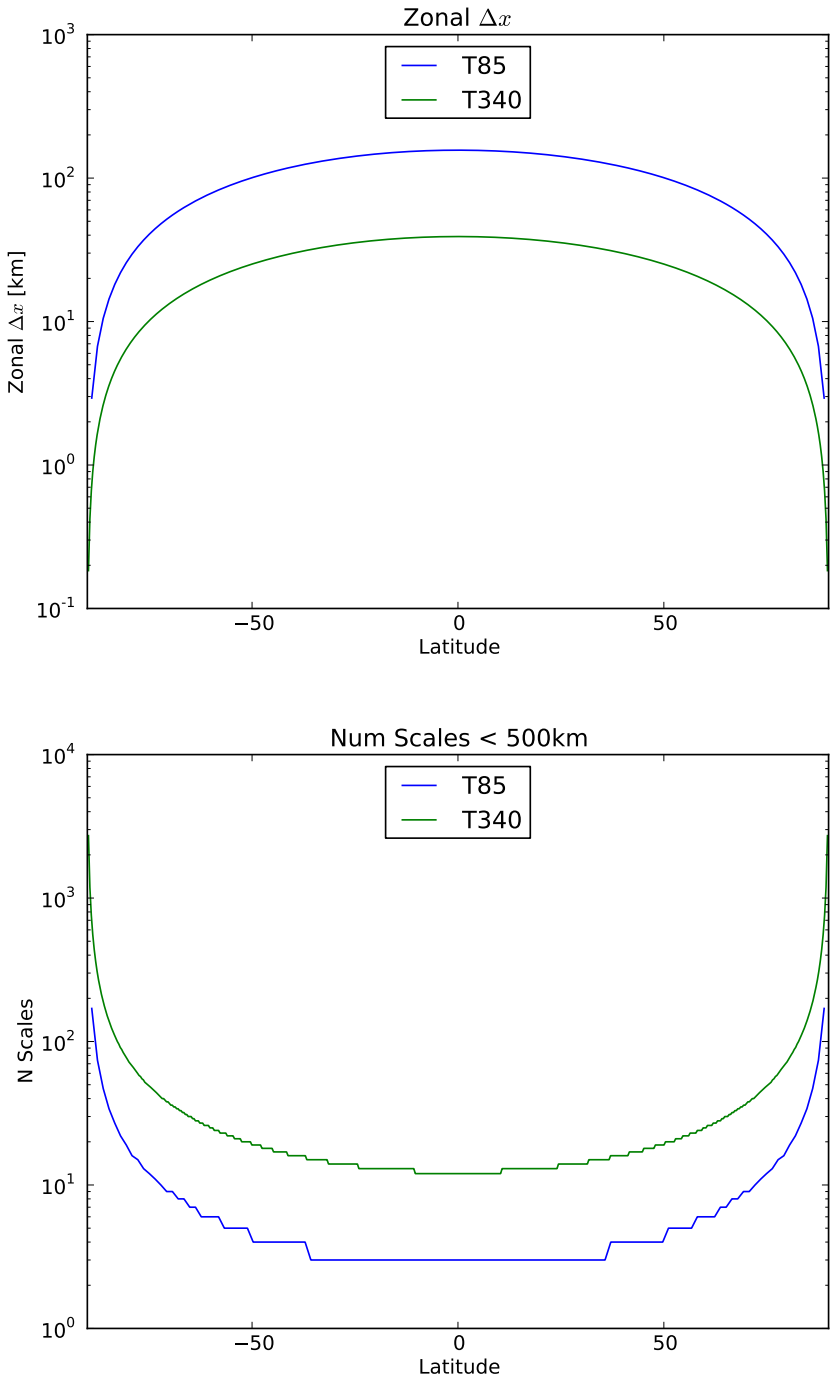

Figure 4.2: The top panel shows the meridional dependence of the zonal grid spacing ΔX for the T85 and T340 simulations. The lower panel shows the meridional dependence of the number of scales s less than 500 km.

4.3 Results and Discussion

The structure function methodology described in Section 4.2.3 has been applied to analyze the water vapor fields from the T85 and T340 aqua-planet experiments. The zonal cross section of first order structure function scaling exponent H for scales less than 500 km is shown in Figure 4.3 for the T85 and T340 simulations respectively. At both resolutions the distribution of H is nearly symmetric about the equator, as would be expected given the lack of a seasonal cycle and the prescribed sea surface temperature distribution. Departures from equatorial symmetry are likely the result of the finite duration (2 years) of the simulation, rather than properties of aqua-planet long term mean climate. For both T85 and T340 resolutions, maximum values of H occur in the subtropical lower (< 850 hPa) troposphere as well as in the subtropical middle free troposphere (≈ 600 hPa). For each height, the minimum value of H occurs in proximity to the equator. The primary difference between the results at T340 and T85 is that for the higher resolution case the range of scaling exponents is increased. Nonetheless, the qualitative similarity between the T85 and T340 scaling exponent field is surprising given the relatively small number of scales at which the T85 structure function is defined below 500 km (see Figure 4.2).

4.3.1 Comparison to AIRS Across Track Structure Function Scaling Exponents H

The most direct comparison between the aqua-planet results reported here and the AIRS first order structure function results reported in Chapter 2 between the aqua-planet scaling exponents and AIRS across track scaling exponents. The AIRS across track scaling exponents are computed from spatial increments of the water vapor field that are approximately zonally oriented. The zonal mean AIRS along track first order structure function scaling exponents are shown in the center column of Figure 2.8. Prior to entering into a comparison of the AIRS and aqua-planet water vapor structure function scaling exponents, it is important to be specific about fundamental differences between the AIRS and aqua-planet water vapor fields. The fundamental differences are:

1. The AIRS water vapor field is dry biased, due to the inability of AIRS to observe full water vapor profiles in scenes with greater than 70% cloud fraction and the positive correlation between cloud amount and water vapor concentration (e.g. Lanzante and Gahrs (2000)). On the other hand, the aqua-planet water vapor field has no such bias as water vapor concentrations are reported even in the presence of 100% cloud fraction.

2. The AIRS zonal mean structure functions are for the DJF and JJA seasons which are the extremes of the seasonal cycle, when equatorial asymmetry is maximized. The aqua-planet simulations do not contain seasonal variations and are symmetric about the equator.

3. The location of land masses has large effects on the location of free tropospheric water vapor source regions as is evident in Figures 2.2 and 2.3. The absence of land in the aqua-planet precludes the localization of water vapor sources to land areas.

4. Numerical simulations are subject to numerical dissipation and imperfect sub-gridscale parameterizations that have been shown to adversely affect the scale invariance of kinetic energy spectra (Skamarock, 2004) as well as water vapor and temperature variance spectra (Kahn et al., 2011). The structure functions computed from observations are not subject to this degradation.

Despite these important differences, the qualitative similarities between the latitude-height distribution of AIRS zonal mean free tropospheric scaling exponents (above 850 hPa) and the aqua-planet free tropospheric scaling exponents is striking. First, the general shape of the equatorial minimum in H is nearly identical between the numerical experiment and the observations, as is the general shape of the subtropical maximum. There is some evidence that the subtropical free tropospheric scaling exponent maximum occurs at a slightly higher altitude and closer to the equator in the observations, although the extent to which this is an artifact of the differences in seasonal cycle between the observations and the simulations or of the structure function computation methodology is difficult to ascertain. Nonetheless, these differences are rather small. Quantitatively, there is considerable numerical agreement between the AIRS scaling exponents and the aqua-planet scaling exponents with free tropospheric scaling exponent typically greater than 0.5 outside of the deep tropics. The T340 simulation agrees better with the observations than does the T85 simulation. The most appreciable qualitative and quantitative difference between the observations and simulations is the asymmetry about the equator associated with the seasonal cycle in the observed scaling exponents. The simulations do not exhibit a similar asymmetry.

Unlike the free troposphere, where there is considerable agreement between the observations and simulations, there are significant differences differences below 850 hPa. First, it is important to remember that the aqua-planet structure function scaling exponents shown in Figure 4.3 are computed from structure functions based on instantaneous water vapor field that are part of the six hourly model output, and are then time averaged. Time averaging in this fashion implicitly assumes that there is no diurnal cycle. This assumption has been tested by repeating the analysis independently (not shown) for each of the four daily output times. This analysis confirmed the lack of a diurnal cycle in the modeled results. This result is not surprising given the meager diurnal variation in maritime boundary layers and the relatively simplistic treatment of boundary layer dynamics in GCMs. This lack of a diurnal cycle in the model results is a significant difference between the aqua-planet and AIRS results. The aqua-planet lower troposphere results seem to be in better agreement with the nighttime (descending) results from AIRS. Nonetheless, the lower tropospheric scaling exponents outside of the tropics from the aqua-planet simulations are distinctly greater than those for any of the observed cases from AIRS. The larger boundary layer scaling exponents in simulations in comparison to the AIRS scaling exponents is consistent with the results of

Skamarock (2004) and Kahn et al. (2011) who show that spectra from atmospheric models are steeper than those computed from comparable observations.

4.4 Extension and Conclusions

In the free troposphere and extratropics there is considerable agreement between the simulated and observed scaling exponents. Few studies have compared observed to simulated spectra for water vapor fields, and fewer still have compared observed to simulated scaling exponents. Kahn et al. (2011) show that water vapor variance spectra scaling exponents are steeper in free running climate models and reanalyses than in satellite observed water vapor fields. They attribute this spectral steepening to an underrepresentation of variability at small length scales in numerical simulations. Several studies (e.g. Koshyk and Hamilton (2001), Skamarock (2004), and Takahashi et al. (2006)) have found that kinetic energy spectra in mesoscale numerical weather prediction models and global climate models generally underrepresent kinetic energy at small scales in comparison to observations. Skamarock (2004) identifies the point where the slope of the simulated spectra agrees with the observed spectra as the effective resolution of the simulation. The agreement between observed and simulated scaling exponents found in this study suggests that water vapor transport and mixing in the free troposphere as resolved by high resolution numerical models are not subject to the spectral steepening effects observed by Kahn et al. (2011) and Skamarock (2004). The difference between the results of Kahn et al. (2011) and the results reported here, highlight the differences between the structure function and variance spectra methodology used in the respective studies, as both rely on water vapor retrievals from AIRS.

Interestingly, Kahn et al. (2011) also report that variance spectra computed from the the super-parameterized version of the Community Atmospheric Model (SP-CAM), which attempts to represent GCM sub-gridscale cloud processes through an embedded high resolution two dimensional cloud resolving model (CRM), are generally too flat across the range of scales captured by the CRM (the GCM sub-gridscales). In their study, the CRM resolves scales between 2 km and 200 km. While, as previously mentioned, there are significant differences between the structure function and variance spectra analysis, it seems likely that the results presented here largely confirm the conclusions of Kahn et al. (2011) that the super parameterization does not provide the necessary scale dependent relationship of variability in the water vapor field.

In the boundary layer (< 850hPa) there is considerable disagreement between the observations and simulations. The differences are characterized by steepening of simulated structure functions relative to the observations, a result that largely confirms the findings of Kahn et al. (2011). As they suggested, it is not immediately clear if the source of this steepening is the result of dissipative numerics at the smallest resolved scales (Koshyk and Hamilton, 2001; Takahashi et al., 2006) or inadequate parameterizations of sub-gridscale processes (Boville, 1991).

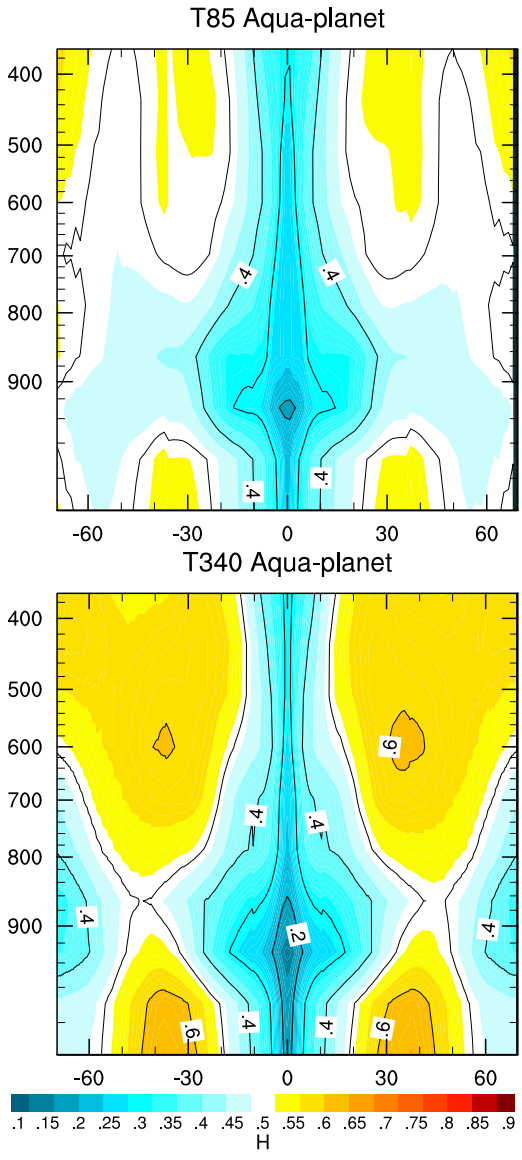

Figure 4.3: First order structure function scaling exponents H for the T85 (top panel) and T340 (lower panel) experiments. The structure functions are computed using only increments in the zonal direction. The scaling exponents are determined using least squares regression.

The agreement between extratropical free troposphere scaling exponents in the observations and simulations may provide insight into the ability of numerical models of the atmosphere to represent the physical processes responsible for transport and mixing of water vapor. As has been discussed in Chapter 2, the predominant source of water vapor in the free troposphere is cross isentropic transport of water vapor associated with tropical convection (e.g. Schneider et al. (2006)). However, there is evidence of a relatively strong impediment to mixing between the tropical and extratropical free troposphere (e.g. Pierrehumbert and Yang (1993)), and this mixing generally occurs in relatively large coherent structures (e.g. Zhu and Newell (1994, 1998), Ralph et al. (2004), and Ralph et al. (2011)). Largely two dimensional chaotic mixing processes, which are characterized by positive Lyapunov exponents (suggesting the tendency of material elements to be strained into filaments) (e.g. Pierrehumbert (1991), Pierrehumbert and Yang (1993) and Cohen and Schultz (2005)), rapidly generate a broad spectrum of filament sizes (Yang and Pierrehumbert, 1994). Note that this model of rapid straining of coherent extrusions of moist tropical air into the extratropics provides a plausible explanation for the filamentary structures observable in Figures 2.11 and 4.1. The agreement between the observations and simulations in the free troposphere may suggest that numerical models adequately resolve this mixing processes, even at length scales well below 500 km. While it is difficult to offer a clear explanation for why scales below 500 km in the free troposphere are so well represented in the numerical simulations, it is likely related to the rapidity with which relatively simple smoothly varying large scale two dimensional velocity fields can generate a wide spectrum of filamentary structures (e.g. Pierrehumbert (1991); Sukhatme and Pierrehumbert (2002)).

In this chapter it has been shown that zonal structure functions of water vapor fields from a T340 resolution aqua-planet simulation exhibit scaling exponents that are consistent with scaling exponents of across-track structure functions from AIRS. However, this not the case in the boundary layer, where zonal structure functions from the aqua-planet simulation are shown to be larger than those from AIRS. The results from the T340 simulation provides better agreement with the results from the AIRS analysis than do the results of the T85 simulation. It is proposed that the similarity between observations and simulations in the free troposphere is a consequence of the importance of large scale mixing processes in determining the spatial distribution of water vapor in the free troposphere. It is proposed that differences within the boundary layer are resultant from deficiencies in the representation of boundary layer processes in the GCM.

Chapter 5

Concluding Remarks

It is the goal of this concluding chapter to provide a synthesis of the results of the preceding chapters so that a final set of conclusions may be drawn and recommendations may be made for further scientific work. The structure of this chapter reflects these purposes: First, the major findings of each chapter are summarized. Second, the results from each chapter are synthesized into a few overarching conclusions. Third, potential impacts of the conclusions are discussed. Fourth, recommendations for further scientific work are proposed.

5.1 Restatement of Primary Research Results

5.1.1 Chapter 1: Introduction

In the introductory chapter, the question of the scale dependence of the water vapor field is raised in the context of the parameterization of clouds in numerical models of the atmosphere. Many cloud parameterizations, particularly those used in global climate models, have a statistical formulation that makes modeling assumptions about the sub-gridscale distribution of water vapor. The sub-gridscale distributions are often parameterized by their statistical moments, making observations of statistical moments crucial in the formulation and verification of statistical cloud parameterizations.

However, the observed distributions and statistical moments carry with them an implicit length scale associated with the spatial resolution at which observations were made. This length scale may not correspond to a length scale appropriate for the parameterization of sub-gridscale cloud variability, hence the scale dependence of observed moments of the water vapor field is directly relevant to the problem of developing and verifying sub-gridscale cloud parameterizations. Furthermore, a complete knowledge of the scale dependence of statistical moments would provide a robust foundation for extrapolating coarse resolution observations to higher resolutions.

Statistical scale invariance, which has been observed for many atmospheric properties and, indeed in many natural systems in general, is recognized as a particularly useful means

of characterizing the spatial scale dependence of variability in the observed water vapor field.

5.1.2 Chapter 2: AIRS Water Vapor Structure Function Analysis

Remote sensing observations offer the benefit of nearly global spatial coverage on relatively short time scales, but their utility in gaining insight into small-scale processes that are relevant to sub-gridscale parameterization is often hindered by their relatively coarse spatial resolution. In Chapter 2, scale dependence of the statistical moments of spatial increments of the water vapor field as observed by physical retrievals from the Atmospheric Infrared Sounder (AIRS) is reported for scales between 50 km and 500 km. This analysis is based on the computation of the first order structure function of physical retrievals of water vapor mass mixing ratio from AIRS. In order to assess the directional dependence (anisotropy) of structure functions of the water vapor field, three sets of structure functions are computed using either all of the increments regardless of their orientation, or only those increments oriented in the satellite across track direction, or only those increments oriented in the satellite along track direction.

The computed structure functions are shown to exhibit nearly ubiquitous power law behavior throughout the analysis domain (60°S to 60°N and 1000 hPa to 300 hPa), with the exception of along track structure functions in the deep tropics. The power law behavior of structure functions suggests the presence of three regimes, one that characterizes the deep tropics at all heights with $H < 0.5$, a second that characterizes the extratropical free troposphere with $H > 0.5$, and a third that characterizes the extratropical boundary layer with $H < 0.5$. The $H < 0.5$ and $H > 0.5$ scaling behavior constitute fundamentally different statistical behaviors. In the boundary layer and tropics $H < 0.5$ indicates anti-persistence of spatial increments, while in the extratropical free troposphere $H > 0.5$ indicates the existence of long range correlations. In the maritime boundary layer the first order structure function power law scaling exponents are found to cluster around $H \approx 1/3$. In the free troposphere (500 hPa) the scaling exponents are found to cluster around $H \approx 0.55$.

The work described in this Chapter has been accepted for publication in the Journal of Climate (Pressel and Collins, 2012).

5.1.3 Chapter 3: WLEF Water Vapor Structure Function Analysis and Detrended Fluctuation Analysis

In situ observations provide higher resolution data than do remotely sensed observations. However, in situ observations do not provide the large spatial coverage typically provided by remote sensing. In Chapter 3, water vapor time series observed at the 396m level of the WLEF tower located near Park Falls, Wisconsin are used to explore the spatial variability of water vapor in the convective mixed layer and nocturnal residual layer during the summer

season. Taylor's frozen turbulence hypothesis is used to transform the observed time scales to length scales.

Two methods are used to compute H. The first method, structure function analysis, is comparable to the method used to determine H in Chapters 2 and 4. Due to the potential for significant statistical non-stationarity associated with diurnal variations in the continental planetary boundary layer, a second method, detrended fluctuation analysis, is used to compute H with the effects of non-stationarity removed.

The results of this analysis indicate that the convective mixed layer and the nocturnal residual layer are characterized by $H \approx 1/3$ and $H \approx 0.54$, respectively, over a range of scales from 1km to at least 100 km. The range of scales is limited by the length of the diurnal cycle. The scaling exponents compare well to those obtained from the analysis of the AIRS water vapor field.

Preliminary results from this Chapter have been presented in a conference paper (Pressel et al., 2010).

5.1.4 Chapter 4: Aqua-planet Water Vapor Structure Function Analysis

In Chapter 4, a structure function methodology is used to compute H from zonally oriented spatial increments of aqua-planet simulated water vapor fields. Two simulations are used in the analysis, one with a horizontal resolution of T85 and a second with T340, with a minimum in H occurring at all heights in the tropics, and maximums in H occurring in the subtropical middle troposphere and boundary layer. The T85 and T340 simulations yield latitude-height cross-sections of H that are qualitatively similar to each other. The scaling exponents computed from the aqua-planet simulations can be compared to the AIRS across track scaling exponents. This comparison shows that within the tropics and free troposphere a striking similarity exists between the latitude-height scaling exponent cross-sections from observations and simulation. However, in the boundary layer (< 850 hPa) there are significant differences between the observed and simulated results. The differing levels of agreement between the free troposphere and boundary layer are likely related to the GCM's ability to represent the important transport and mixing processes in these two regimes.

It is argued that the scale dependent variability of the water vapor field in the free troposphere is governed by chaotic mixing that depends on large scale two dimensional atmospheric motions. These motions are likely to be well resolved by the GCM, this accurate simulation therefore leads to good agreement between the scale dependence of water vapor in the GCM and observations. In the boundary layer, the scale dependent variability of the water vapor field is likely to be dependent on boundary layer processes that are small scale and not well represented in the GCM. This leads to an under representation of variability at small scales, as is suggested by the steeper structure functions relative to the observations and is consistent with the findings of Kahn et al. (2011).

5.2 Synthesis of Results

In this section the results of Chapters 2, 3, and 4 will be synthesized into an overarching set of conclusions from which the general scientific impacts of the work can be described and on which a set of recommendations can be based.

The results presented herein have shown empirical evidence from remote sensing and in situ observations that statistical scale invariance is a nearly ubiquitous property of the tropospheric water vapor field at scales below 500 km. The statistical scale invariance can be characterized by structure function scaling exponents H, with $H > 1/2$ in the free troposphere and $H \approx 1/3$ in the boundary layer. Aqua-planet simulations are used to show that numerical models can produce free tropospheric water vapor fields whose structure function scaling exponents agree to a high degree with the scaling exponents of structure functions computed from observed fields. This is likely related to the controlling influence of the well resolved large scale 2D velocity field on the water vapor variability. Aqua-planet simulations are shown to be unable to reproduce observed water vapor structure function scaling in the boundary layer. This is likely related to the controlling influence of boundary layer processes, which are not well represented in GCMs, on water vapor variability.

5.3 Recommendations

In this section recommendations for future research efforts are described based on the synthesis of results given in Section 5.2. This discussion is subdivided into observational, theoretical, and modeling recommendations.

5.3.1 Observational Recommendations

Chapter 2 of this dissertation relies on observations from the Atmospheric Infrared Sounder (AIRS), to provide nearly global observations of the vertically resolved water vapor field, which allowed the characterization of variability at scales as small as 50 km. The success of the methodology described in Chapter 2 underscores the obvious utility of future satellite missions, that could provide high vertical resolution measurements of atmospheric properties. One primary limitation of the AIRS water vapor retrievals are their relatively wide and varying empirical averaging kernels (shown in Figure 2.9). The width of these averaging kernels makes the interpretation of vertical gradients in the computed scaling exponents somewhat ambiguous. Despite this ambiguity, the vertical variation in scaling exponents is quite consistent with the height resolved water vapor structure function scaling exponents from very high vertical resolution water vapor profiles from an aircraft based lidar (Fischer et al., 2012).

Chapter 3 of this dissertation relied on observations from the WLEF tower to investigate the scale dependence of water vapor variability from in situ measurements. The scales investigated from the WLEF dataset ranges from 1 km to 100 km. The lower bound on

the scales of assessment is in part specified because of the damping of small scale gradients resulting from the transport of sampled air from the 396 m tower level to the measurement apparatus at the base of the tower. An obvious means of circumventing this effect, and to potentially investigate scale dependence at smaller scales, would be to move the measurement apparatus to the observational level. A second obvious extension of this work would be to apply the methodology to data sets from other very tall towers in order to determine if the results are specific to midlatitude continental boundary layers and residual layers. However, at this time there are few instrumented very tall towers that provide the appropriate datasets to exactly replicate the analysis presented herein.

The methodology developed for computing structure functions from AIRS observations is sufficiently general that it can be applied to observations of other properties observed by AIRS. Application of the methodology to other trace gas species such as O_3, CO_2, CH_4 and CO could provide fundamental insight into the transport and mixing of quantities that have sources, sinks, and atmospheric lifetimes that differ significantly from those of water vapor.

5.3.2 Theoretical Recommendations

At present, to the author's knowledge, there is no theoretical explanation for the observed $H \approx 1/3$ scaling of water vapor structure functions that has been observed at scales between 1km and 500 km in the boundary layer as reported in Chapters 2 and 3 of this dissertation. This is despite the fact that there is growing empirical evidence that $H \approx 1/3$ behavior is a nearly universal property of the boundary layer at mesoscales. Further theoretical work that attempts to understand the physical reasons for the observed $H \approx 1/3$ universality may provide fundamental insight into the dynamics of the planetary boundary layer at scales much larger than the boundary layer height.

It was shown in Chapter 3 that there is striking agreement between the residual layer values of H estimated from in situ observations and free tropospheric values of H estimated from the remote sensing observations from AIRS. As was mentioned in Chapter 3, perhaps the most obvious unifying aspect of the free troposphere and residual layer dynamics is the two dimensionality of the velocity field. Numerical studies, similar to those performed by Pierrehumbert and Yang (1993), of the residual layer may provide insight into the two dimensional mixing processes that lead to the similar structure function behavior between the residual layer and free troposphere.

5.3.3 Modeling Recommendations

The near universality of $H \approx 1/3$ behavior in the boundary layer provides strong support for designing parameterizations that are designed to incorporate this scale dependence into their formulation. Cusack et al. (1999) have shown that parameterizations that assume a scale dependence of variance consistent with $H \approx 1/3$ behavior have led to improvements in an operational model. One caveat of a parameterization that tries to directly make use of this observed scale dependent behavior is that it requires that the variability at grid scale

be represented correctly in the numerical model. The results of Chapter 4 suggest that the variability at small scales may be underrepresented in numerical models, and suggests that parameterizations for sub-gridscale variability should be designed to take this into account for this under prediction of gridscale variability.

Bibliography

Aumann, H., et al., 2003: AIRS/AMSU/HSB on the Aqua mission: Design, science objectives, data products, and processing systems. *IEEE Transactions on Geoscience and Remote Sensing*, **41 (2)**, 253–264.

Batchelor, G. K., 1959: Small-scale variation of convected quantities like temperature in turbulent fluid. Part 1. General discussion and the case of small conductivity. *Journal of Fluid Mechanics*, **5 (01)**, 113–133.

Bechtold, P., J. Cuijpers, P. Mascart, and P. Trouilhet, 1995: Modeling of trade wind cumuli with a low-order turbulence model: Toward a unified description of Cu and Sc clouds in meteorological models. *Journal of the Atmospheric Sciences*, **52 (4)**, 455–463.

Bechtold, P., C. Fravalo, and J. Pinty, 1992: A model of marine boundary-layer cloudiness for mesoscale applications. *Journal of the Atmospheric Sciences*, **49 (18)**, 1723–1744.

Berger, B., K. Davis, C. Yi, P. Bakwin, and C. Zhao, 2001: Long-term carbon dioxide fluxes from a very tall tower in a northern forest: Flux measurement methodology. *Journal of Atmospheric and Oceanic Technology*, **18 (4)**, 529–542.

Bony, S. and J. Dufresne, 2005: Marine boundary layer clouds at the heart of cloud feedback uncertainties in climate models. *Geophysical Research Letters*, **32 (20)**, doi: 10.1029/2005GL023851.

Bony, S., J. Dufresne, H. Le Treut, J. Morcrette, and C. Senior, 2004: On dynamic and thermodynamic components of cloud changes. *Climate Dynamics*, **22 (2)**, 71–86.

Bony, S. and K. Emanuel, 2001: A parameterization of the cloudiness associated with cumulus convection; evaluation using TOGA COARE data. *Journal of the Atmospheric Sciences*, **58 (21)**, 3158–3183.

Bony, S., et al., 2006: How well do we understand and evaluate climate change feedback processes? *Journal of Climate*, **19 (15)**, 3445–3482.

Bougeault, P., 1981: Modeling the trade-wind cumulus boundary layer. Part I: Testing the ensemble cloud relations against numerical data. *Journal of the Atmospheric Sciences*, **38 (2)**, 2414–2428.

Boville, B., 1991: Sensitivity of simulated climate to model resolution. *Journal of Climate*, **4 (5)**, 469–486.

Brown, P. and G. Robinson, 1979: The variance spectrum of tropospheric winds over eastern europe. *Journal of the Atmospheric Sciences*, **36 (2)**, 270–286.

Cess, R., et al., 1996: Cloud feedback in atmospheric general circulation models: An update. *Journal of Geophysical Research*, **101 (D8)**, 12 791–12 794.

Cho, J., R. Newell, and J. Barrick, 1999a: Horizontal wavenumber spectra of winds, temperature, and trace gases during the Pacific Exploratory Missions: 1. Climatology. *Journal of Geophysical Research*, **104 (D5)**, 5697–5716.

Cho, J., R. Newell, and J. Barrick, 1999b: Horizontal wavenumber spectra of winds, temperature, and trace gases during the Pacific Exploratory Missions: 2. Gravity waves, quasi-two-dimensional turbulence, and vortical modes. *Journal of Geophysical Research*, **104 (D13)**, 16 297–16 308.

Cho, J., R. Newell, and G. Sachse, 2000: Anomalous scaling of mesoscale tropospheric humidity fluctuations. *Geophysical Research Letters*, **27 (3)**, 377–380.

Cohen, R. A. and D. M. Schultz, 2005: Contraction rate and its relationship to frontogenesis, the Lyapunov exponent, fluid trapping, and airstream boundaries. *Monthly Weather Review*, **133 (5)**, 1353–1369.

Collins, W., et al., 2006: The community climate system model: CCSM3. *Journal of Climate*, **19 (11)**, 2122–2143.

Comstock, K., C. Bretherton, and S. Yuter, 2005: Mesoscale variability and drizzle in southeast Pacific stratocumulus. *Journal of the Atmospheric Sciences*, **62 (10)**, 3792–3807.

Corrsin, S., 1951: On the spectrum of isotropic temperature fluctuations in an isotropic turbulence. *Journal of Applied Physics*, **22 (4)**, 469–473.

Cusack, S., J. Edwards, and R. Kershaw, 1999: Estimating the subgrid variance of saturation, and its parametrization for use in a GCM cloud scheme. *Quarterly Journal of the Royal Meteorological Society*, **125 (560)**, 3057–3076.

Davis, A., A. Marshak, W. Wiscombe, and R. Cahalan, 1994: Multifractal characterizations of nonstationarity and intermittency in geophysical fields: Observed, retrieved, or simulated. *Journal of Geophysical Research*, **99 (D4)**, 8055–8072.

Davis, A., A. Marshak, W. Wiscombe, and R. Cahalan, 1996: Scale invariance of liquid water distributions in marine stratocumulus. Part I: Spectral properties and stationarity issues. *Journal of the Atmospheric Sciences.*, **53 (11)**, 1538–1558.

Davis, K., P. Bakwin, C. Yi, B. Berger, C. Zhao, R. Teclaw, and J. Isebrands, 2003: The annual cycles of co2 and h2o exchange over a northern mixed forest as observed from a very tall tower. *Global Change Biology*, **9 (9)**, 1278–1293.

Divakarla, M., C. Barnet, M. Goldberg, L. McMillin, E. Maddy, W. Wolf, L. Zhou, and X. Liu, 2006: Validation of Atmospheric Infrared Sounder temperature and water vapor retrievals with matched radiosonde measurements and forecasts. *Journal of Geophysical Research*, **111 (D9)**, doi:10.1029/2005JD006116.

Dufresne, J. and S. Bony, 2008: An assessment of the primary sources of spread of global warming estimates from coupled atmosphere-ocean models. *Journal of Climate*, **21 (19)**, 5135–5144.

Feder, J., 1988: *Fractals*. Plenum Press.

Fischer, L., C. Kiemle, and G. C. Craig, 2012: Height-resolved variability of midlatitude tropospheric water vapor measured by an airborne lidar. *Geophysical Research Letters*, **39**, doi:10.1029/2011GL050621.

Fowler, L., D. Randall, and S. Rutledge, 1996: Liquid and ice cloud microphysics in the CSU general circulation model. Part I: Model description and simulated microphysical processes. *Journal of Climate*, **9 (3)**, 489–529.

Frehlich, R. G. and R. D. Sharman, 2010: Equivalence of velocity statistics at constant pressure or constant altitude. *Geophysical Research Letters*, **37**, doi:10.1029/2010GL042912.

Gage, K. S. and G. D. Nastrom, 1986: Theoretical interpretation of atmospheric wavenumber spectra of wind and temperature observed by commercial aircraft during gasp. *Journal of the Atmospheric Sciences*, **43 (7)**, 729–740.

Garratt, J., 1994: *The atmospheric boundary layer*. Cambridge University Press.

Gettelman, A., et al., 2004: Validation of Aqua satellite data in the upper troposphere and lower stratosphere with in situ aircraft instruments. *Geophysical Research Letters.*, **31 (22)**, doi:10.1029/2004GL020730.

Ghan, S., X. Bian, A. Hunt, and A. Coleman, 2002: The thermodynamic influence of subgrid orography in a global climate model. *Climate Dynamics*, **20 (1)**, 31–44.

Gifford, F., 1956: The relation between space and time correlations in the atmosphere. *Journal of Meteorology*, **13 (3)**, 289–294.

Gossard, E., 1960: Power spectra of temperature, humidity and refractive index from aircraft and tethered balloon measurements. *IRE Transactions on Antennas and Propagation*, **8 (2)**, 186 –201.

Hagan, D., et al., 2004: Validating AIRS upper atmosphere water vapor retrievals using aircraft and balloon in situ measurements. *Geophysical Research Letters*, **31 (21)**, L21 103, doi:10.1029/2004GL020302.

Hall, A. and S. Manabe, 1999: The role of water vapor feedback in unperturbed climate variability and global warming. *Journal of Climate*, **12 (8, Part 1)**, 2327–2346.

Harrison, E., P. Minnis, B. Barkstrom, V. Ramanathan, R. Cess, and G. Gibson, 1990: Seasonal variation of cloud radiative forcing derived from the Earth Radiation Budget Experiment. *Journal of Geophysical Research*, **95 (18)**, 18 687–18 703.

Haynes, P. and J. Vanneste, 2004: Stratospheric tracer spectra. *Journal of the Atmospheric Sciences*, **61 (2)**, 161–178.

Held, I., 2005: The gap between simulation and understanding in climate modeling. *Bulletin Of The American Meteorological Society*, **86 (11)**, doi:10.1175/BAMS-86-11-1609.

Held, I. and B. Soden, 2000: Water vapor feedback and global warming. *Annual Review of Energy and the Environment*, **25**, 441–475.

Holton, J., 2004: *An introduction to dynamic meteorology*. Academic Press.

Hurst, H., 1956: Methods of using long-term storage in reservoirs. *ICE Proceedings*, Vol. 5, 519–543.

Illingworth, A. and S. Bony, 2009: *Clouds in the perturbed climate*, chap. Observational strategies at Meso- and Large Scales to Reduce Critical Uncertainties in Future Cloud Changes. The MIT Press.

Ivanova, K. and M. Ausloos, 1999: Application of the detrended fluctuation analysis (DFA) method for describing cloud breaking. *Physica A: Statistical Mechanics and its Applications*, **274 (1)**, 349–354.

Ivanova, K., M. Ausloos, E. Clothiaux, and T. Ackerman, 2000: Break-up of stratus cloud structure predicted from non-brownian motion liquid water and brightness temperature fluctuations. *Europhysics Letters*, **52**, 40–46.

Kahn, B. and J. Teixeira, 2009: A global climatology of temperature and water vapor variance scaling from the Atmospheric Infrared Sounder. *Journal of Climate*, **22 (20)**, 5558–5576.

Kahn, B., et al., 2011: Temperature and water vapor variance scaling in global models: Comparisons to satellite and aircraft data. *J. Atmos. Sci.*, **68 (9)**, 2156–2168.

Kantelhardt, J., S. Zschiegner, E. Koscielny-Bunde, S. Havlin, A. Bunde, and H. Stanley, 2002: Multifractal detrended fluctuation analysis of nonstationary time series. *Physica A: Statistical Mechanics and its Applications*, **316 (1)**, 87–114.

Kavasseri, R. and R. Nagarajan, 2005: A multifractal description of wind speed records. *Chaos, Solitons & Fractals*, **24 (1)**, 165–173.

Koscielny-Bunde, E., A. Bunde, S. Havlin, H. E. Roman, Y. Goldreich, and H.-J. Schellnhuber, 1998: Indication of a universal persistence law governing atmospheric variability. *Physical Review Letters*, **81**, 729–732.

Koshyk, J. N. and K. Hamilton, 2001: The horizontal kinetic energy spectrum and spectral budget simulated by a high-resolution troposphere-stratosphere mesosphere GCM. *Journal of the Atmospheric Sciences*, **58 (4)**, 329–348.

Lanzante, J. and G. Gahrs, 2000: The clear-sky bias of TOVS upper-tropospheric humidity. *Journal of Climate*, **13 (22)**, 4034–4041.

Lappe, U. and B. Davidson, 1963: On the range of validity of Taylor's hypothesis and the Kolmogoroff spectral law. *Journal of the Atmospheric Sciences*, **20 (6)**, 569–576.

Le Trent, H. and Z. Li, 1991: Sensitivity of an atmospheric general circulation model to prescribed SST changes: Feedback effects associated with the simulation of cloud optical properties. *Climate Dynamics*, **5 (3)**, 175–187.

Leung, Y., 2010: *Knowledge discovery in spatial data*. Springer Verlag.

Lewellen, W. and S. Yoh, 1993: Binormal model of ensemble partial cloudiness. *Journal of the Atmospheric Sciences*, **50 (9)**, 1228–1237.

Li, F., W. D. Collins, M. F. Wehner, D. L. Williamson, J. G. Olson, and C. Algieri, 2011: Impact of horizontal resolution on simulation of precipitation extremes in an aqua-planet version of Community Atmospheric Model (CAM3). *Tellus Series A-Dynamic Meteorology And Oceanography*, **63 (5)**, 884–892, doi:10.1111/j.1600-0870.2011.00544.x.

Li, Z. and Y. Zhang, 2007: Quantifying fractal dynamics of groundwater systems with detrended fluctuation analysis. *Journal of Hydrology*, **336 (1)**, 139–146.

Lin, B., B. Wielicki, L. Chambers, Y. Hu, and K. Xu, 2002: The iris hypothesis: a negative or positive cloud feedback? *Journal of Climate*, **15 (1)**, 3–7.

Lindborg, E., 1999: Can the atmospheric kinetic energy spectrum be explained by two-dimensional turbulence? *Journal of Fluid Mechanics*, **388**, 259–288.

Lindborg, E., K. Tung, G. Nastrom, J. Cho, and K. Gage, 2010: Comment on Reinterpreting aircraft measurement in anisotropic scaling turbulence by Lovejoy et al.(2009). *Atmospheric Chemistry and Physics*, **10 (3)**, 1401–1402.

Lohmann, U., N. McFarlane, L. Levkov, K. Abdella, and F. Albers, 1999: Comparing different cloud schemes of a single column model by using mesoscale forcing and nudging technique. *Journal of Climate*, **12 (2)**, 438–461.

Lovejoy, S., 1982: Area-perimeter relation for rain and cloud areas. *Science*, **216 (4542)**, 185–187.

Lovejoy, S., A. Tuck, and D. Schertzer, 2010: Horizontal cascade structure of atmospheric fields determined from aircraft data. *Journal of Geophysical Research*, **115**, doi: 10.1029/2009JD013353.

Lovejoy, S., A. Tuck, D. Schertzer, and S. Hovde, 2009: Reinterpreting aircraft measurements in anisotropic scaling turbulence. *Atmospheric Chemistry and Physics*, **9**, 5007–5025.

L'vov, V. S., A. Pomyalov, and I. Procaccia, 1999: Temporal surrogates of spatial turbulent statistics: The taylor hypothesis revisited. *Physical Review E*, **60**, 4175–4184, doi: 10.1103/PhysRevE.60.4175.

Mackay, D., D. Ahl, B. Ewers, S. Gower, S. Burrows, S. Samanta, and K. Davis, 2002: Effects of aggregated classifications of forest composition on estimates of evapotranspiration in a northern wisconsin forest. *Global Change Biology*, **8 (12)**, 1253–1265.

Maddy, E. and C. Barnet, 2008: Vertical resolution estimates in version 5 of AIRS operational retrievals. *Geoscience and Remote Sensing, IEEE Transactions on*, **46 (8)**, 2375–2384.

Mapes, B., S. Tulich, T. Nasuno, and M. Satoh, 2008: Predictability Aspects of Global Aqua-planet Simulations with Explicit Convection. *Journal of The Meteorological Society of Japan*, **86A**, 175–185.

Marenco, A., et al., 1998: Measurement of ozone and water vapor by Airbus in-service aircraft: The MOZAIC airborne program, An overview. *Journal of Geophysical Research.*, **103 (D19)**, 25 631–25 642.

Marshak, A., A. Davis, W. Wiscombe, and R. Cahalan, 1997: Scale invariance in liquid water distributions in marine stratocumulus. Part II: Multifractal properties and intermittency issues. *Journal of the Atmospheric Sciences*, **54 (11)**, 1423–1444.

Matsoukas, C., S. Islam, and I. Rodriguez-Iturbe, 2000: Detrended fluctuation analysis of rainfall and streamflow time series. *Journal of Geophysical Research*, **105 (D23)**, 29 165–29 172.

Medeiros, B., B. Stevens, I. Held, M. Zhao, D. Williamson, J. Olson, and C. Bretherton, 2008: Aquaplanets, climate sensitivity, and low clouds. *Journal of Climate*, **21 (19)**, 4974–4991.

Mellor, G., 1977: The Gaussian Cloud Model Relations. *Journal of the Atmospheric Sciences*, **34 (2)**, 356–358.

Moller, F., 1963: On the influence of changes in the CO2 concentration in air on the radiation balance of the Earth's surface and on the climate. *Journal of Geophysical Research*, **68 (13)**, 3877–3886.

Nastrom, G. and K. Gage, 1985: A climatology of atmospheric wavenumber spectra of wind and temperature observed by commercial aircraft. *Journal of the Atmospheric Sciences*, **42 (9)**, 950–960.

Nastrom, G., W. Jasperson, and K. Gage, 1986: Horizontal spectra of atmospheric tracers measured during the Global Atmospheric Sampling Program. *Journal of Geophysical Research*, **91 (D12)**, 13 201–13 213.

Neale, R. and B. Hoskins, 2000a: A standard test for agcms including their physical parametrizations: I: The proposal. *Atmospheric Science Letters*, **1 (2)**, 101–107.

Neale, R. and B. Hoskins, 2000b: A standard test for AGCMs including their physical parametrizations. II: Results for the met office model. *Atmospheric Science Letters*, **1 (2)**, 108–114.

Neale, R., et al., 2010: Description of the NCAR Community Atmosphere Model (CAM 4.0). *NCAR Technical Note, National Center of Atmospheric Research*.

O'Gorman, P. and T. Schneider, 2009: Scaling of precipitation extremes over a wide range of climates simulated with an idealized GCM. *Journal of Climate*, **22 (21)**, 5676–5685.

Olsen, E., E. Fishbein, T. Hearty, S. Lee, F. Irion, B. Kahn, and E. Manning, 2007: AIRS version 5 release level 2 standard product quickstart.

Ose, T., 1993: An examination of the effects of explicit cloud water in the UCLA GCM. *Journal of the Meteorological Society of Japan*, **71 (1)**, 93–109.

Peng, C.-K., S. V. Buldyrev, S. Havlin, M. Simons, H. E. Stanley, and A. L. Goldberger, 1994: Mosaic organization of DNA nucleotides. *Physical Review E*, **49**, 1685–1689.

Pierrehumbert, R., 1994: Tracer microstructure in the large-eddy dominated regime. *Chaos, Solitons & Fractals*, **4 (6)**, 1091–1110.

Pierrehumbert, R., H. Brogniez, and R. Roca, 2007: On the relative humidity of the atmosphere. *The Global Circulation of the Atmosphere*, Princeton University Press, 143–185.

Pierrehumbert, R. and H. Yang, 1993: Global chaotic mixing on isentropic surfaces. *Journal of Atmospheric Science*, **50 (15)**, 2462–2480.

Pierrehumbert, R. T., 1991: Chaotic mixing of tracer and vorticity by modulated travelling Rossby waves. *Geophysical and Astrophysical Fluid Dynamics*, **58**, 285–319.

Pierrehumbert, R. T., 1996: Anomalous scaling of high cloud variability in the tropical Pacific. *Geophys. Res. Lett.*, **23 (10)**, 1095–1098.

Pierrehumbet, R., 1995: Thermostats, radiator fins, and the local runaway greenhouse. *Journal of The Atmospheric Sciences*, **52 (10)**, 1784–1806.

Pope, S., 2000: *Turbulent flows*. Cambridge University Press.

Pressel, K. G., W. Collins, and A. Desai, 2010: Variance scaling in water vapor measurements from a tall tower. *Extended Abstracts, 13th Conf. on Cloud Physics*, URL http : //ams.confex.com/ams/13CldPhy13AtRad/techprogram/paper$_1$71839.htm.

Pressel, K. G. and W. D. Collins, 2012: First order structure function analysis of statistical scale invariance in the airs observed water vapor field. *Journal of Climate*.

Pu, Z. and L. Zhang, 2010: Validation of Atmospheric Infrared Sounder temperature and moisture profiles over tropical oceans and their impact on numerical simulations of tropical cyclones. *Journal of Geophysical Research*, **115 (D24)**, D24 114.

Ralph, F. M., P. J. Neiman, G. N. Kiladis, K. Weickmann, and D. W. Reynolds, 2011: A multi-scale observational case study of a pacific atmospheric river exhibiting tropical-extratropical connections and a mesoscale frontal wave. *Monthly Weather Review*, **139 (4)**, 1169–1189.

Ralph, F. M., P. J. Neiman, and G. A. Wick, 2004: Satellite and CALJET aircraft observations of atmospheric rivers over the eastern north pacific ocean during the winter of 1997/98. *Monthly Weather Review*, **132 (7)**, 1721–1745.

Ramanathan, V., R. Cess, E. Harrison, P. Minnis, B. Barkstrom, E. Ahmad, and D. Hartmann, 1989: Cloud-radiative forcing and climate: Results from the Earth Radiation Budget Experiment. *Science*, **243 (4887)**, 57–63.

Schneider, S., 1972: Cloudiness as a global climatic feedback mechanism- The effects on the radiation balance and surface temperature of variations in cloudiness. *Journal of the Atmospheric Sciences*, **29 (8)**, 1413–1422.

Schneider, T., P. O'Gorman, and X. Levine, 2009: Water vapor and the dynamics of climate changes. *Arxiv preprint arXiv:0908.4410*.

Schneider, T., K. Smith, P. O'Gorman, and C. Walker, 2006: A climatology of tropospheric zonal-mean water vapor fields and fluxes in isentropic coordinates. *J. Climate*, **19 (22)**, 5918–5933.

Sherwood, S., R. Roca, T. Weckwerth, and N. Andronova, 2010: Tropospheric water vapor, convection, and climate. *Reviews of Geophysics*, **48**, doi:10.1029/2009RG000301.

Skamarock, W. C., 2004: Evaluating mesoscale nwp models using kinetic energy spectra. *Monthly Weather Review*, **132 (12)**, 3019–3032.

Smith, R., 1990: A scheme for predicting layer clouds and their water content in a general circulation model. *Quarterly Journal of the Royal Meteorological Society*, **116 (492)**, 435–460.

Soden, B. and I. Held, 2006: An assessment of climate feedbacks in coupled ocean-atmosphere models. *Journal of Climate*, **19 (14)**, 3354–3360.

Soden, B. and J. Lanzante, 1996: An assessment of satellite and radiosonde climatologies of upper-tropospheric water vapor. *Journal of Climate*, **9 (6)**, 1235–1250.

Solomon, S., et al., 2007: *Intergovernmental Panel on Climate Change. The Fourth Assessment Report of the Intergovernmental Panel on Climate Change.* Cambridge UK: Cambridge University Press.

Sommeria, G. and J. Deardorff, 1977: Subgrid-scale condensation in models of nonprecipitating clouds. *Journal of the Atmospheric Sciences*, **34 (2)**, 344–355.

Sparling, L. and J. Bacmeister, 2001: Scale dependence of tracer microstructure: Pdfs, intermittency and the dissipation scale. *Geophysical Research Letters.*, **28 (14)**, 2823–2826.

Stephens, G., 2005: Cloud feedbacks in the climate system: A critical review. *Journal of Climate*, **18 (2)**, 237–273.

Stolle, J., S. Lovejoy, and D. Schertzer, 2009: The stochastic multiplicative cascade structure of deterministic numerical models of the atmosphere. *Nonlinear Processes in Geophysics*, **16 (5)**, 607–621.

Stull, R., 1988: *An introduction to boundary layer meteorology.* Springer.

Stull, R. and C. Ahrens, 2000: *Meteorology for scientists and engineers.* Brooks/Cole.

Sukhatme, J. and R. T. Pierrehumbert, 2002: Decay of passive scalars under the action of single scale smooth velocity fields in bounded two-dimensional domains: From non-self-similar probability distribution functions to self-similar eigenmodes. *Physical Review E*, **66**, doi:10.1103/PhysRevE.66.056302.

Susskind, J., C. Barnet, and J. Blaisdell, 2003: Retrieval of atmospheric and surface parameters from AIRS/AMSU/HSB data in the presence of clouds. *Geoscience and Remote Sensing, IEEE Transactions on*, **41 (2)**, 390–409.

Takahashi, Y. O., K. Hamilton, and W. Ohfuchi, 2006: Explicit global simulation of the mesoscale spectrum of atmospheric motions. *Geophysical Research Letters*, **33 (12)**, doi: 10.1029/2006GL026429.

Talkner, P. and R. Weber, 2000: Power spectrum and detrended fluctuation analysis: Application to daily temperatures. *Physical Review E*, **62 (1)**, 150–160.

Taylor, G. I., 1935: Statistical theory of turbulence. *Proceedings of the Royal Society of London. Series A, Mathematical and Physical Sciences*, **151 (873)**, 421–444.

Tjemkes, S. and M. Visser, 1994: Horizontal variability of temperature, specific humidity, and cloud liquid water as derived from spaceborne observations. *Journal of Geophysical Research*, **99 (D11)**, 23 089–23 105.

Tobin, D., et al., 2006: Atmospheric Radiation Measurement site atmospheric state best estimates for Atmospheric Infrared Sounder temperature and water vapor retrieval validation. *Journal of Geophysical Research*, **111 (D9)**, doi:10.1029/2005JD006103.

Tompkins, A., 2002: A prognostic parameterization for the subgrid-scale variability of water vapor and clouds in large-scale models and its use to diagnose cloud cover. *Journal of the Atmospheric Sciences*, **59 (12)**, 1917–1942.

Tompkins, A., 2003: Impact of temperature and humidity variability on cloud cover assessed using aircraft data. *Quarterly Journal of the Royal Meteorological Society*, **129 (592)**, 2151–2170.

Tuck, A., 2010: From molecules to meteorology via turbulent scale invariance. *Quarterly Journal of the Royal Meteorological Society*, **136 (650)**, 1125–1144.

Tuck, A. and S. Hovde, 1999: Fractal behavior of ozone, wind and temperature in the lower stratosphere. *Geophysical Research Letters.*, **26 (9)**, 1271–1274.

Tuck, A., S. Hovde, and M. Proffitt, 1999: Persistence in ozone scaling under the hurst exponent as an indicator of the relative rates of chemistry and fluid mechanical mixing in the stratosphere. *The Journal of Physical Chemistry A*, **103 (49)**, 10 445–10 450.

Varotsos, C. A., J. M. Ondov, A. P. Cracknell, M. N. Efstathiou, and M. N. Assimakopoulos, 2006: Long-range persistence in global aerosol index dynamics. *International Journal of Remote Sensing*, **27 (16)**, 3593–3603, doi:10.1080/01431160600617236.

Wallace, J. and P. Hobbs, 2006: *Atmospheric science: an introductory survey*. Academic Press.

Waugh, D., 1996: Seasonal variation of isentropic transport out of the tropical stratosphere. *Journal of Geophysical Research*, **101 (D2)**, 4007–4023.

Webb, M., et al., 2006: On the contribution of local feedback mechanisms to the range of climate sensitivity in two GCM ensembles. *Climate Dynamics*, **27 (1)**, 17–38.

Wetherald, R. and S. Manabe, 1988: Cloud feedback processes in a general circulation model. *Journal of the Atmospheric Sciences*, **45 (8)**, 1397–1415.

Williams, K. and M. Webb, 2009: A quantitative performance assessment of cloud regimes in climate models. *Climate Dynamics*, **33 (1)**, 141–157.

Williams, P., 2005: Modelling climate change: the role of unresolved processes. *Philosophical Transactions of the Royal Philosophical Society A*, **363 (1837)**, 2931–2946.

Williamson, D., 2008: Convergence of aqua-planet simulations with increasing resolution in the community atmospheric model, version 3. *Tellus A*, **60 (5)**, 848–862.

Wood, A. and G. Chan, 1994: Simulation of stationary Gaussian processes in [0, 1] d. *Journal of Computational and Graphical Statistics*, **3 (4)**, 409–432.

Wood, R. and P. R. Field, 2011: The distribution of cloud horizontal sizes. *Journal of Climate*, **24 (18)**, 4800–4816.

Wood, R. and D. L. Hartmann, 2006: Spatial variability of liquid water path in marine low cloud: The importance of mesoscale cellular convection. *Journal of Climate*, **19 (9)**, 1748–1764.

Wood, R. and J. P. Taylor, 2001: Liquid water path variability in unbroken marine stratocumulus cloud. *Quarterly Journal of the Royal Meteorological Society*, **127 (578)**, 2635–2662.

Yang, H. and R. Pierrehumbert, 1994: Production of dry air by isentropic mixing. *Journal of the Atmospheric Sciences*, **51 (23)**, 3437–3437.

Yi, C., K. Davis, B. Berger, and P. Bakwin, 2001: Long-term observations of the dynamics of the continental planetary boundary layer. *Journal of the Atmospheric Sciences*, **58 (10)**, 1288–1299.

Zhang, Q., C. Xu, Y. Chen, and Z. Yu, 2008: Multifractal detrended fluctuation analysis of streamflow series of the yangtze river basin, china. *Hydrological Processes*, **22 (26)**, 4997–5003.

Zhao, C., P. Bakwin, and P. Tans, 1997: A design for unattended monitoring of carbon dioxide on a very tall tower. *Journal of Atmospheric and Oceanic Technology*, **14 (5)**, 1139–1145.

Zhu, Y. and R. E. Newell, 1994: Atmospheric rivers and bombs. *Geophysical Research Letters*, **21 (18)**, doi:10.1029/94GL01710.

Zhu, Y. and R. E. Newell, 1998: A proposed algorithm for moisture fluxes from atmospheric rivers. *Monthly Weather Review*, **126 (3)**, 725–735.